Fast Forward and Inverse Wave Propagation for Tomographic Imaging of Defects in Solids

by

Qinan Chang

A Dissertation Presented in Partial Fulfillment
of the Requirements for the Degree
Doctor of Philosophy

Approved December 2018 by the
Graduate Supervisory Committee:

Yongming Liu, Chair
Marc Mignolet
Aditi Chattopadhyay
Hao Yan
Yi Ren

ARIZONA STATE UNIVERSITY

May 2019

ABSTRACT

Aging-related damage and failure in structures, such as fatigue cracking, corrosion, and delamination, are critical for structural integrity. Most engineering structures have embedded defects such as voids, cracks, inclusions from manufacturing. The properties and locations of embedded defects are generally unknown and hard to detect in complex engineering structures. Therefore, early detection of damage is beneficial for prognosis and risk management of aging infrastructure system.

Non-destructive testing (NDT) and structural health monitoring (SHM) are widely used for this purpose. Different types of NDT techniques have been proposed for the damage detection, such as optical image, ultrasound wave, thermography, eddy current, and microwave. The focus in this study is on the wave-based detection method, which is grouped into two major categories: feature-based damage detection and model-assisted damage detection. Both damage detection approaches have their own pros and cons. Feature-based damage detection is usually very fast and doesn't involve in the solution of the physical model. The key idea is the dimension reduction of signals to achieve efficient damage detection. The disadvantage is that the loss of information due to the feature extraction can induce significant uncertainties and reduces the resolution. The resolution of the feature-based approach highly depends on the sensing path density. Model-assisted damage detection is on the opposite side. Model-assisted damage detection has the ability for high resolution imaging with limited number of sensing paths since the entire signal histories are used for damage identification. Model-based methods are time-consuming due to the requirement for the inverse wave propagation solution, which is especially true for the large 3D structures.

The motivation of the proposed method is to develop efficient and accurate model-based damage imaging technique with limited data. The special focus is on the efficiency of the damage imaging algorithm as it is the major bottleneck of the model-assisted approach. The computational efficiency is achieved by two complimentary components. First, a fast forward wave propagation solver is developed, which is verified with the classical Finite Element(FEM) solution and the speed is 10-20 times faster. Next, efficient inverse wave propagation algorithms is proposed. Classical gradient-based optimization algorithms usually require finite difference method for gradient calculation, which is prohibitively expensive for large degree of freedoms. An adjoint method-based optimization algorithms is proposed, which avoids the repetitive finite difference calculations for every imaging variables. Thus, superior computational efficiency can be achieved by combining these two methods together for the damage imaging. A coupled Piezoelectric (PZT) damage imaging model is proposed to include the interaction between PZT and host structure. Following the formulation of the framework, experimental validation is performed on isotropic and anisotropic material with defects such as cracks, delamination, and voids. The results show that the proposed method can detect and reconstruct multiple damage simultaneously and efficiently, which is promising to be applied to complex large-scale engineering structures.

ACKNOWLEDGMENTS

I would like to express my sincere gratitude towards my advisor, Dr. Yongming Liu for his constant guidance and support throughout the duration of my study. I would like to thank him for his great mentorship and valuable insights which helped me to achieve the research objectives. I would also like to thank the members of my Supervisory Committee, Dr. Marc Mignolet, Dr. Aditi Chattopadhyay, Dr. Hao Yan and Dr. Yi Ren.

I am grateful to my fellow group members, current and former, for their willingness to help and their strong work ethic which motivated me in my own research. Finally, I would like to thank my family and friends for their support.

TABLE OF CONTENTS

Page

LIST OF TABLES

Table Page

LIST OF FIGURES

1. INTRODUCTION

1.1. Background

Engineering structures have embedded defects such as voids, cracks, inclusions from manufacturing. Other structural damage and failure which are commonly seen in ageing structures (pressure vessels, aircraft wings, buildings, manufacturing machinery), such as fatigue cracking, corrosion, and delamination, which are critical for structural integrity. Early detection of damage is important for prognosis and risk management of engineering structures. Due to the complexity of engineering structures and small length scale of the damage, the properties and locations of embedded defects are generally unknown and hard to detect. Therefore, quality control and anomaly detection are important for the risk assessment of engineering structures.

Non-destructive testing (NDT) and/or structural health monitoring (SHM) techniques are widely used to ensure the safety and reliability of structures. Different types of SHM techniques have been proposed for the damage detection, such as Acoustic Emission (AE), strain load monitoring, guided wave (GW) as reviewed in [1], diagnostic damage imaging as discussed in [2], eddy current pulsed thermography [3], microwave, ultrasound and other methods are widely used in damage detection on metallic material and composites material. SHM methods are classified into different categories based on its applications and working algorithm: Detection methods using strain gauges, fiber optics are classified as Passive methods, which the input and loading are usually unknown [2][4]. The other classification is Active methods like wave-based damage detection methods are widely used because of cost-effective and flexibility. Some wave-

based methods are reviewed here, Lamb wave has been used for damage detection in metallic structures and composites as discussed in [2], [5], [6]. A wavelet active sensing method is proposed for delamination detection [7]. The fatigue crack detection using Lamb wave is proposed in [8]. A guided wave based damage indexing is mentioned in [9].

The advantages of wave propagation methods in SHM is discussed here. The prior knowledge of input also great facilitates the damage identification based on waveform information. Since the waveform from one actuator can be received by multiple receivers, any change on received waveform is a strong indicator of damage existence. Therefore, the waveform or extracted features are key information of damage detection.

Based on the information used in acoustic wave-based detection methods, it can be divided into two major categories: feature-based damage detection and model-based damage detection. In feature-based damage detection, features from physics model are extracted and used as indicators of damage. A decision-making model based on selected feature is used to deicide existence of novelty. A brief review on some feature-based model is discussed here: a neural network is implemented for damage detection purpose using selected acoustic wave features [10]. The Bayesian network imaging method is proposed for delamination detection in composites [11]. Diagnostic imaging based on feature from Lamb wave propagation is mentioned in [12]. A combined feature regression for fatigue damage detection is discussed in [13]. The highlight of feature-based methods is because they are not sensitive to the physics model. However, the computational complexity is an important consideration in feature-based method such as Neural network. Another drawback is the time spent on training dataset for high

dimensional data. Therefore, the efficiency of damage detection highly depends on the learning rate in the data-driven methods [14].

For model-assisted damage detection, acoustic wave propagation model is directly used for damage identification. Some well-developed model-based methodologies are briefly reviewed here. An anomaly detection in images via smooth-sparse decomposition method is propose in [15]. A finite element model updating method (FEMU) and virtual field method(VFM) based on full-field measurements were discussed for damage detection in [16]. Some numerical damage detection methods such as Levenburg-Marquart based method coupled with finite element (FEM) was proposed for material parameter estimation purpose[17]. A trust-region algorithm coupled with FEM modeling was proposed for damage identification in reinforced concrete [18]. The wide use of FEM for inverse wave propagation is due to its maturity in solving the acoustic problems. However, damage detection usually requires the finer mesh for the high frequency acoustic waves and is not computationally efficient for large 3D structures. They are also noise-sensitive due to the uncertainties in measurement as mentioned. The benefits for model-assisted damage detection is the ability for high resolution imaging with limited number of sensing paths since the entire signal histories are used for damage identification.

1.2. Research Objective

Based on the above brief review, the motivation of the proposed study is to develop very efficient damage imaging technique for 2D and 3D structures using model-assisted approach. The special focus is on the efficiency of the imaging algorithm as it is the

major bottleneck of the model-assisted approach. The computational efficiency is achieved by two complimentary components. First, a fast forward wave propagation solver is needed. A k-space (wavenumber-space) approach [19] is proposed for the damage imaging. The implementation of k-space method highly speeds up the simulation efficiency and saves computational memory compared to classical FEM solver [20]. Next, an efficient inverse wave propagation algorithm is proposed for damage detection and identification. An adjoint method-based optimization algorithms is proposed, which avoids the repetitive finite difference gradient calculations for every imaging variables. Thus, superior computational efficiency can be achieved by combining these two methods together for the damage imaging.

Some advantages and uniqueness of the proposed study are: 1. The proposed framework only needs limited measurements to reconstruct the damage to improve computational efficiency. 3. The forward problems is solved based on coupled first-order equations, which is easy to solve in mathematical view [21]. 4. Compared to the most applications on soft and homogeneous materials using the k-space method, the focus is on materials with strong discontinuity widely seen in engineering structures. 5. Sensitivity equations commonly seen in inverse problems are also solved using the k-space method to improve the computational efficiency.

The report consists of three major tasks: 1) the wave propagation solution algorithms for elastic solids using k-space model; 2). the adjoint method-based optimization algorithms for damage imaging; 3) the experimental damage detection on laminated composites based on adjoint method and k-space method.

The tasks above are divided into five chapters. First, a modified pseudo-spectral (k-space) numerical model for wave propagation is proposed in Chapter 2. One major advantage of the proposed method is the superior computational efficiency compared to the classical finite element method-based wave propagation and gradient-based optimization algorithms, which also great facilitates damage detection. The k-space formulation for wave propagation in 2D and 3D anisotropic solids are discussed. It's first verified with analytical solution and FEM (Finite Element Method). Demonstration examples on wave propagation in healthy (no damage) anisotropic material are performed. Example with defects are added in the numerical model like cracks, delamination, corrosions which are defects commonly seen in engineering structures are also discussed. The proposed method shows capability of modeling wave propagation in general anisotropic material. The proposed study shows high computational efficiency and accuracy compared to classical FEM, which great facilitates the application on inversion wave problems like damage detection which will be discussed in Chapter 3.

Chapter 3 talks about an inverse tomography method for damage detection using adjoint and k-space method. A novel damage imaging of engineering structures and materials methodology using the inverse wave propagation in k-space with adjoint method is proposed for damage imaging. Following this, parametric studies for measurement duration, number of sensors, noise effect, and computational efficiency are discussed in detail. Next, demonstration examples for concrete structures with and without reinforcement are presented. The proposed inverse damage detection show capability to localize the damage and estimate the shape and properties of damage.

In Chapter 4, the experimental damage detection on laminated composites is discussed. At the current stage, experimental data is preprocessed to be used in the numerical model. Due to the uncertainties related to material properties, the numerical model is calibrated using a healthy composites plate (no damage). The experimental inverse damage detection on laminated composites will be discussed in the future work. At last, several conclusions are drawn, and future work is discussed in the last chapter.

Chapter 5 is on Uncertainty Quantification and reliability analysis of the proposed study. The uncertainty associated to material properties in manufacturing process, noisy measurements in the test and uncertainties in the model parameters, will cause variation on the system performance. Therefore, an uncertainty management method should be created to control the uncertainty propagation in the model. A Bayesian updating model show capability of reducing uncertainties in damage diagnosis as mentioned in [11]. An overview is given, and detailed study will be included in future work.

The overview of the methods mentioned above, and the proposed framework is shown in Fig.1-1 and Fig. 1-2.

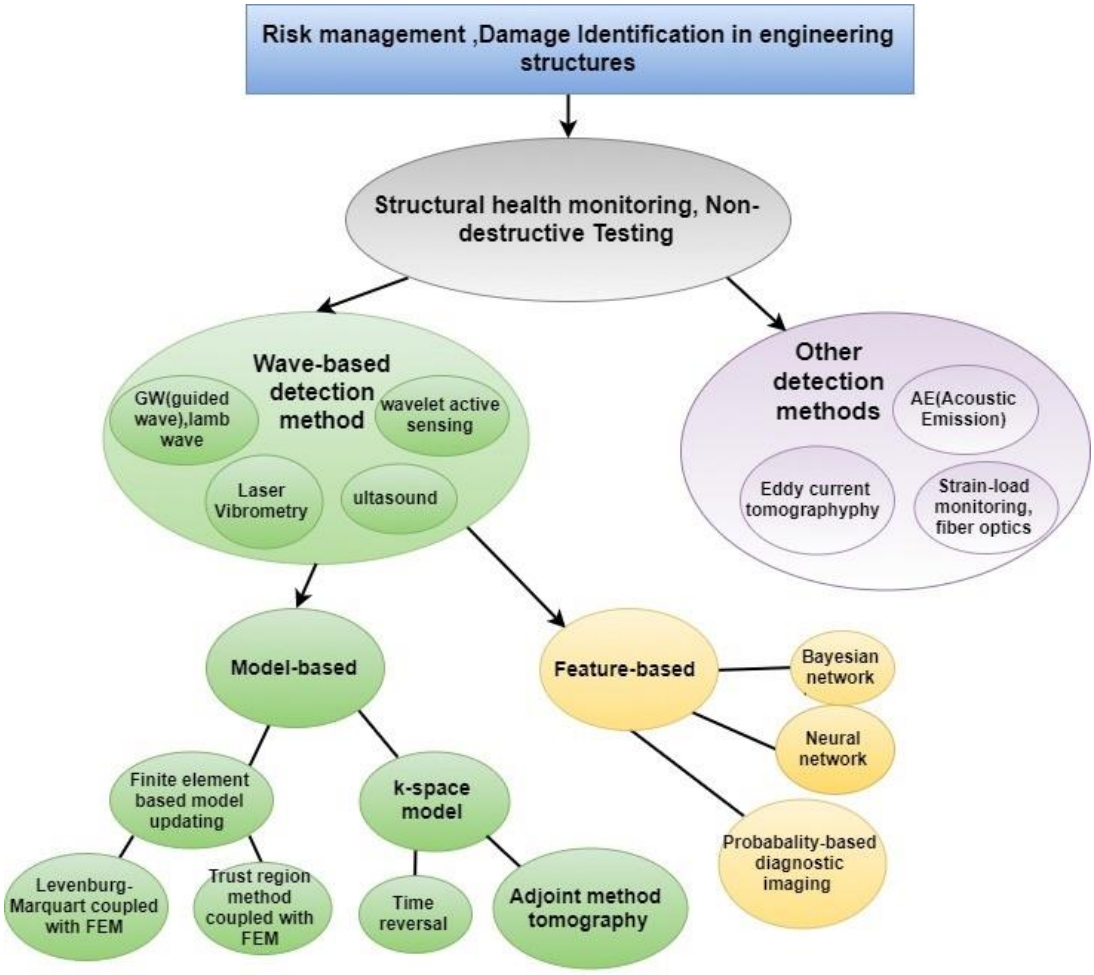

Figure 1. 1 Review of damage detection methods in SHM

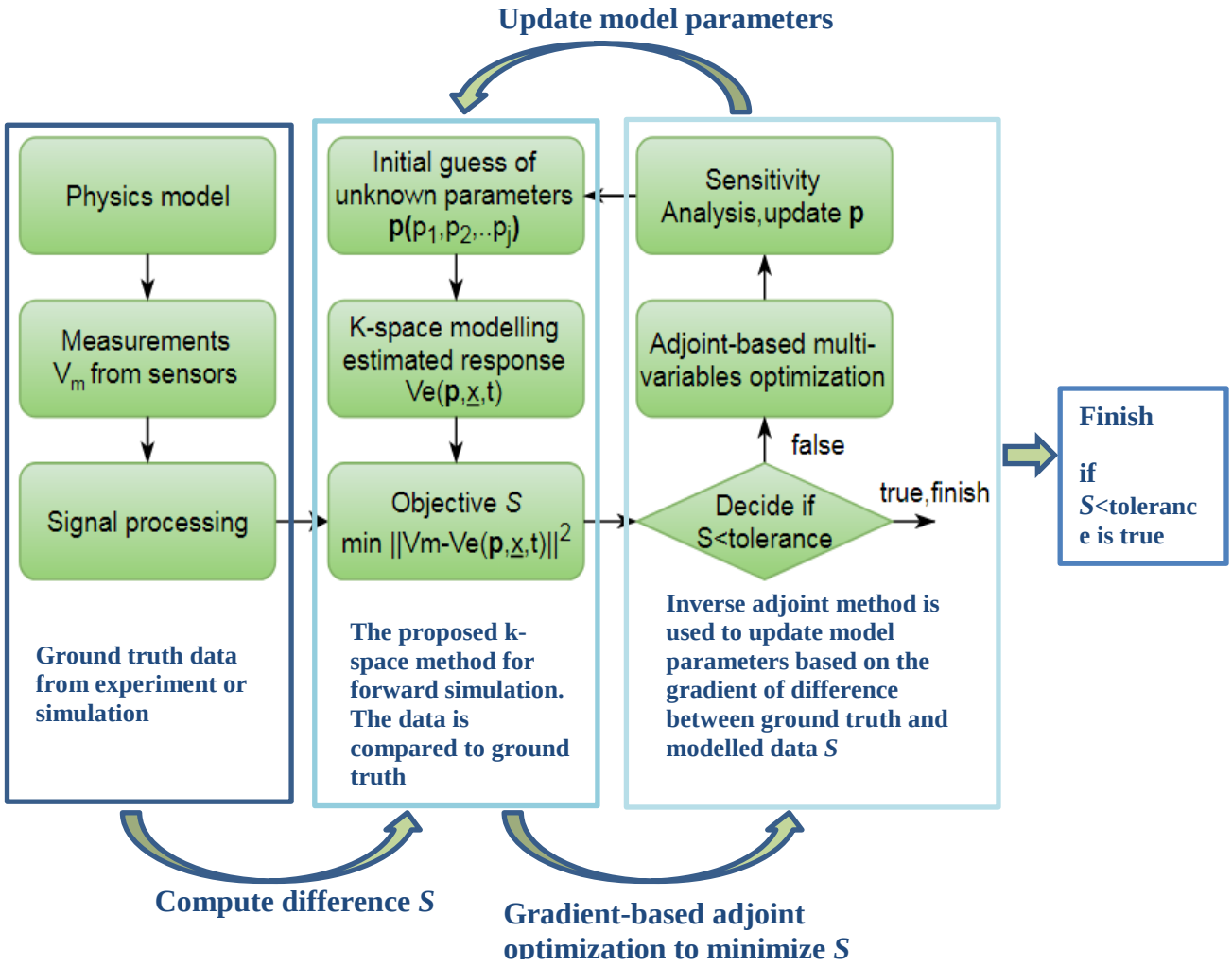

Figure 1. 2 Flow chart of proposed framework

2. WAVE PROPAGATION SIMULATION IN DAMAGED ISOTROPIC AND ANISOTROPIC SOLIDS USING K-SPACE METHOD

2.1. Abstract

A numerical model for wave propagation simulation in damaged isotropic and anisotropic solids is proposed in this paper. The wave propagation problem is formulated using two coupled first-order differential equations for both isotropic and anisotropic solids and a wavenumber corrector-based pseudo-spectral method is used to obtain the time-domain solution using the forward and inverse Fourier transformation. Following this, explicit modelling of crack-like damage commonly seen in engineering materials are investigated. Parametric and convergence study are performed to investigate the proposed simulation algorithms. Numerical examples are used to verify the proposed methodology by comparing the results from analytical solutions and classical finite element methods. Discussions and conclusions are drawn based on the proposed study.

Keywords: wave propagation, pseudo-spectral, k-space, anisotropic, crack

2.2. Introduction

Wave propagation-based detection methods, such as ultrasound imaging [22], Lamb-wave propagation [23], laser ultrasound [24], and photoacoustic imaging methods [25], are widely used for damage and anomaly detection. Accurate and efficient numerical simulation of wave propagation is critical for the mechanism understanding of the above-mentioned damage detection methodologies. Extensive studies have been proposed for this purpose, such as finite element method, finite difference method, boundary element

method, spectral element method, and k-space method. Some previous studies are briefly reviewed below. Recently, a discontinuous Galerkin pseudo spectral-time domain (DG-PSTD) [26] method for solving elastic and acoustic wave propagation problems is proposed, which can handle both conformal and non-conformal meshes. The finite difference method was implemented for wave propagation in heterogeneous materials [27]. The hybrid boundary element method was used to investigate elastic guided wave scattering for surface defects in [28]. It was shown that the Spectral Finite Element method can be applied to detect very small size damage [29]. Co-simulation of Lamb wave propagation in composites models with both delamination and matrix cracking using FEM was proposed in [30]. A non-conformal mesh discontinues Galerkin (DG) PSTD method for elastic wave scattering with arbitrary fracture inclusion is recently proposed in [31], in which a linear-slip model is used to mesh thin-layer fracture to reduce the computational cost at the same time provides high accuracy.

Most existing elastic wave propagation problems are solved with finite difference and finite element methods. Both are known to be local methods since wave equation of each point is solved based on nearby points in numerical solutions. One example is that in the first-order forward finite difference scheme in which the gradient of a point is represented by the local points nearby in the numerical model. To increase the accuracy, the number of points per wavelength associated with the gradient calculation should be increased. This requirement significantly increases the computational cost for large 3D structures with high frequency wave components. The k-space method is a global method since the spatial derivative of a point is derived with the Fourier collocation method which requires a forward and inverse Fourier transformation of all points in the field of interest [32]. It's

based on the Pseudo-Spectral method with improved stability and accuracy by introducing the k-space operator. The k-space method only requires two points per wavelength based on the nature of Fourier series and Nyquist Sampling theorem [33] [34] [35]. The Fourier series can be written in the form of sinusoidal functions which can be represented by two points sampled per wavelength based on the Nyquist-Shannon sampling theorem [35] . Thus, in the case of large-scale simulation, finite element and finite difference methods are computationally more expensive than the k-space method. The proposed study focuses on the k-space method as it has superior computational efficiency for large-scale structural applications.

The k-space formulation was first applied to electromagnetic scattering problem in [36]. Most recent advances of the k-space method are for biomedical applications in soft materials. A simplified version of k-space method by defining a *k-t* propagator for wave propagation in tissues was proposed in [33]. Relatively few studies focus on the extension of the k-space method to solids. The k-space formulation was generalized to solve the elastodynamic scattering problem in which the second-order differential equations were solved for wave propagation in isotropic solids [13]. Alternative approaches have been proposed by using a set of coupled first-order differential equations for acoustic wave propagation in homogeneous and heterogeneous materials [38]. The above-mentioned studies are for isotropic materials and very few studies have been proposed for general anisotropic materials until very recently [39][40] . A simulation framework using the k-space formulation for anisotropic solids based on the second-order differential equation representations was proposed for applications on elastic imaging in geophysics [39]. The main differences of the proposed study with the methods discussed in [35] -[40] are: 1) the

proposed study uses two coupled-first order differential equations of anisotropic elastic wave propagation rather one second-order differential equation. The major benefit using the coupled first-order equations is that the system equations are relatively easy to be solved [41]; 2) the proposed study focuses on the discontinuity widely seen in structural materials (e.g., crack-like damage). Special algorithm setting is required to ensure the convergence when using the k-space method and is investigated in this study.

The proposed study has the advantage on computational efficiency and memory as mentioned in [42] that "The pseudo-spectral method (PSM) or the K-space method is an attractive alternative to the FDM that exploits the fast Fourier transform (FFT) algorithm for computing the spatial derivatives." However, they have their own difficulties when solving the first-order elastic wave equations, among which the Nyquist errors and the generation of non-causal ringing artefacts cause serious challenge, particularly in the presence of large abrupt changes in the medium. As well known, the use of staggered-grid formulations mitigates these problems. But the standard staggered-grid PSM cannot tackle anisotropy with symmetry lower than orthorhombic [42]. A previous study on this issue can be found in [42].

The paper is organized as follows. First, the general formulation of isotropic and anisotropic materials using the k-space method is discussed. The algorithm is discussed in Section 2. Next, inclusion of crack-like damage in the proposed simulation is discussed by explicitly including the crack with proper time step modifications. Following this, several numerical examples are used to verify and validate the developed numerical simulation framework, for both undamaged and damaged, homogeneous and heterogeneous solids. The accuracy is quantified by computing the error between the proposed method and the

FEM result or with the analytical solution. The computational efficiency using the k-space method and the classical FEM is compared and discussed. Finally, several conclusions are drawn based on the proposed study.

2.3. K-Space Formulation for General Isotropic And Anisotropic Solids

The constitutive equation in a general elastic, isotropic/anisotropic, homogeneous material is shown below based on the generalized Hooke's Law,

$$\sigma_{ij} = C_{ijkl}\varepsilon_{kl} \tag{0.1}$$

The strain-displacement relation is,

$$\varepsilon_{kl} = \frac{1}{2}\left(\frac{\partial u_k}{\partial x_l} + \frac{\partial u_l}{\partial x_k}\right) \tag{0.2}$$

where u_k is the *k-th* component of displacement. ε_{kl} is a second-order strain tensor component, σ_{ij} is second-order Cauchy stress tensor component and C_{ijkl} is a fourth-order stiffness tensor in the Cartesian coordinate. Subscripts *i, j, k, l* follows the Einstein summation convention. The equation of motion can be expressed as

$$\rho \frac{\partial^2 u_i}{\partial^2 t} = \frac{\partial \sigma_{ij}}{\partial x_j} + f_i \tag{0.3}$$

where *t* is time, ρ is the material's density, f_i is the *i-th* component of external force. To simplify the equation of motion into coupled first-order partial differential equations, one can replace the time derivative of displacement by velocity. Therefore, Eq. 3 is expressed in term of velocity as,

$$\rho \frac{\partial v_i}{\partial t} = \frac{\partial \sigma_{ij}}{\partial x_j} + f_i \tag{0.4}$$

where v_i is i-th component of the particle velocity. By taking the time derivative of Eq. 0.1,

$$\frac{\partial \sigma_{ij}}{\partial t} = \frac{C_{ijkl}}{2}\left(\frac{\partial v_k}{\partial x_l} + \frac{\partial v_l}{\partial x_k}\right) \tag{0.5}$$

Eq. 2.3.0.4 and Eq. 2.3.0.5 are the first-order coupled formulation used in k-space method. The reason of using first-order equations is discussed here. The Perfect match layer (PML) is an efficient way to prevent wave wrapping happening in Fourier series based method solving wave propagation problems which is necessary for the proposed method [43]. The technique of PML was first introduced in 1994 which implemented on electromagnetic to avoid wave reflection on the boundary [44]. The PML not only applies to electromagnetic wave, but the acoustic wave and elastic wave propagation as mentioned in [45], [46]. The techniques mentioned above are all based on the first-order wave equations. Therefore, to implement the PML for the proposed k-space method, the first-order equations are used in this paper.

Thus, a first order k-space or wavenumber operator of elastic wave equation is required. The wavenumber operator is the key point in the proposed framework. It turns out to be helpful in the gradient calculation. A k-space operator was proposed for solving acoustic wave propagation problem [38]. Similar procedures will be followed in this paper. The uniqueness of the k-space operator in the proposed framework is that the operator is derived based on the elastic wave equations and applied to damaged solids. It's easy to get the k-space operator if the material is isotropic since the wave speed is only related to two Lame constants. A more complicated case that wave propagation in damaged anisotropic material is considered and details are discussed in following sections.

To find the first-order wavenumber operator, we start from Eq.0.3. It can be formed as,

$$\rho \frac{\partial^2 \boldsymbol{u}}{\partial^2 t} = [\boldsymbol{\nabla C \nabla}^T]\boldsymbol{u} + \boldsymbol{f} \tag{0.6}$$

where $\boldsymbol{\nabla}$ is the gradient operator and $\boldsymbol{u}$ is the displacement vector. Detailed derivation of Eq. 2.3.6 is included in the Appendix. The components of the displacement are (u_x, u_y, u_z). A wave decomposition methodology by solving the Christoffel equation is applied to the proposed method [47]. Eq. 2.3.6 can be written in a simplified form,

$$\frac{\partial^2 \boldsymbol{u}}{\partial^2 t} = \boldsymbol{T}\boldsymbol{u} + \boldsymbol{f} \tag{0.7}$$

where $\boldsymbol{T}$ is called the Christoffel matrix, which is derived based on the solution of the plane wave propagating in anisotropic material [48]. By taking the Fourier Transform on Eq. 0.7,

$$\omega^2 \bar{\boldsymbol{u}} = \boldsymbol{T}\bar{\boldsymbol{u}} \tag{0.8}$$

where $\bar{\boldsymbol{u}}$ is in the *k-f* domain (i.e., spatial and temporal frequency domain). Eq. 2.3.8 can be written in an indicial form to show its relativity with the wavenumber $\boldsymbol{k}$,

$$\omega^2 \bar{u}_i = T_{il}\bar{u}_l \tag{0.9}$$

where ω is the angular frequency and $T_{il} = \frac{1}{\rho}k^2 C_{ijkl} n_k n_j$ and k is the magnitude of wavenumber $\boldsymbol{k}$, n_k is the unit vector of wave propagation direction. Eq.8 can be written as an eigenvalue problem,

$$(T_{il} - {v_i}^2 k^2 \delta_{il})\, \bar{u}_l = 0, \tag{0.10}$$

$$v = \frac{\omega}{k}$$

where δ_{il} is the Kronecker delta function and v is the phase velocity. It has been shown that v^2k^2 is the eigenvalue of $\boldsymbol{T}$ and $\bar{u}_l$ is the corresponding eigenvector [49].

Since $\boldsymbol{T}$ is positive definite due to the symmetry of $\boldsymbol{C}$, it can be factorized using the eigendecomposition,

$$\boldsymbol{T} = \boldsymbol{Q}\boldsymbol{\alpha}\boldsymbol{Q}^{\mathrm{T}} \tag{2.3.11}$$

where $\boldsymbol{Q}$ is a matrix with each column being the eigenvector of $\boldsymbol{T}$. $\boldsymbol{Q}$ is orthogonal, indicating that $\boldsymbol{Q^TQ=I}$, where I is 3 by 3 identity matrix and $\boldsymbol{\alpha}$ is the eigenvalue matrix where its component $\alpha_{ij} = v_i^2k^2\delta_{ij}$. If an inverse Fourier Transform in temporal domain is applied to Eq. 2.3.8, the new equation can be written in terms of $\widetilde{\boldsymbol{u}}$ (i.e., the displacement vector $\boldsymbol{u}$ in the wavenumber space),

$$\boldsymbol{Q}\boldsymbol{\alpha}\boldsymbol{Q}^{\mathrm{T}}\widetilde{\boldsymbol{u}} + \frac{\partial^2\widetilde{\boldsymbol{u}}}{\partial^2 t} = \boldsymbol{0} \tag{2.3.12}$$

It should be noted that $\boldsymbol{T}$ is independent of time step and it remains same when transformed to the temporal domain. Because of the orthogonality of $\boldsymbol{Q}$, the following equation is derived by multiplying Eq. 2.3.12 by $\boldsymbol{Q}^{\mathrm{T}}$,

$$\boldsymbol{I}\boldsymbol{\alpha}\boldsymbol{Q}^{\mathrm{T}}\widetilde{\boldsymbol{u}} + \boldsymbol{Q}^{\mathrm{T}}\frac{\partial^2\widetilde{\boldsymbol{u}}}{\partial^2 t} = \boldsymbol{0} \tag{2.3.13}$$

Or in a compact form,

$$\boldsymbol{\alpha}\widetilde{\boldsymbol{U}} + \frac{\partial^2\widetilde{\boldsymbol{U}}}{\partial^2 t} = \boldsymbol{0} \tag{0.14}$$

where $\widetilde{\boldsymbol{U}}=\boldsymbol{Q}^{\mathrm{T}}\widetilde{\boldsymbol{u}}$. The indicial form of Eq. 2.3.14 can be discretized by using a second-order finite difference scheme. The second-order time derivative of $\widetilde{\boldsymbol{U}}$ is approximated,

$$\frac{\widetilde{U}_i(t+\Delta t)-2\widetilde{U}_i(t)+\widetilde{U}_i(t-\Delta t)}{(\Delta t)^2}=-{b_i}^2\widetilde{U}_i \tag{2.3.15}$$

where $b_i=v_ik$, or $b_i^2=\alpha_i$. Eq. 15 needs to be transformed back to spatial domain by using the inverse spatial Fourier Transform,

$$\frac{U_i(t+\Delta t)-2U_i(t)+U_i(t-\Delta t)}{(\Delta t)^2}=-{v_i}^2F^{-1}\{k^2F(U_i)\} \tag{2.3.16}$$

where U_i is the displacement component in the spatial space. The spatial Fourier Transform of U_i and the spatial derivative of U_i is,

$$\widetilde{U}_i=F(U_i)=\frac{1}{2\pi}\iint_{-\infty}^{+\infty}U_i\,e^{jkx}dx \tag{0.17}$$

$$\frac{dU_i}{dx_m}=F^{-1}(jk_mF(U_i))$$

where j is the imaginary number and x is a spatial variable in the Cartesian coordinate.

One important factor that affects the accuracy of the pseudo-spectral solution is the numerical dispersion [50]. The dispersion error can be reduced if a smaller time step Δt or a higher order numerical scheme is used. However, reducing the time step may results in very high computational cost. Thus, a k-space correction is introduced to cancel the effect caused by the dispersion error. Similar scheme called *k-t* space operator was implemented for acoustic wave propagation problems [38]. Such correction was proved to improve the accuracy even when the time step is large [33]. A wavenumber operator of elastic wave in anisotropic material is proposed and applied to Eq. 0.15. The details are discussed in the following sections,

Eq. 0.15 can be also formed as,

$$\ddot{\tilde{U}} + b^2\tilde{U} = 0 \tag{0.18}$$

where the subscripts are omitted in the equation above for brevity. Instead of using a standard FD method to get the time derivative as shown in Eq.15, an exact FD scheme is used due to the high numerical stability as discussed in [51]. A set of two independent solution of Eq.18 are,

$$\tilde{U}^{(1)} = \mathrm{e}^{ibt},\ \tilde{U}^{(2)} = e^{-ibt} \tag{0.19}$$

The discretized of Eq. 0.18 can be written as,

$$\begin{vmatrix} \tilde{U}^{n-1} & e^{ib\Delta tn} & e^{-ib\Delta tn} \\ \tilde{U}^{n} & e^{ib\Delta t(n+1)} & e^{-ib\Delta t(n+1)} \\ \tilde{U}^{n+1} & e^{ib\Delta t(n+2)} & e^{-ib\Delta t(n+2)} \end{vmatrix} = 0 \tag{0.20}$$

$$\text{or } \tilde{U}^{n+1} + \tilde{U}^{n-1} - 2\cos(b\Delta t)\,\tilde{U}^{n} = 0 \tag{0.21}$$

where *n* is the discretized time step. Since,

$$\cos(x) = 1 - 2sin^2(\frac{x}{2}) \tag{0.22}$$

By using the trigonometric identity in Eq. 0.22, Eq. 0.21 is written as,

$$\tilde{U}^{n+1} + \tilde{U}^{n-1} - 2\tilde{U}^{n} + 4\sin^2(\frac{b\Delta t}{2})\tilde{U}^{n} = 0 \tag{0.23}$$

Eq. 0.23 can be also put in a form comparable to the FD scheme,

$$\frac{\tilde{U}^{n+1} + \tilde{U}^{n-1} - 2\tilde{U}^{n}}{(\Delta t)^2} = \frac{-4\sin^2(\frac{b\Delta t}{2})\tilde{U}^{n}}{(\Delta t)^2} \tag{0.24}$$

and by replacing $sin(\frac{b\Delta t}{2}))$ by $sinc(\frac{b\Delta t}{2})\frac{b\Delta t}{2}$ in Eq. 0.24, we found that,

$$\frac{\tilde{U}^{n+1} + \tilde{U}^{n-1} - 2\tilde{U}^{n}}{(\Delta t)^2 sinc^2(\frac{b\Delta t}{2})} = -\mathrm{b}^2\tilde{U}^{n} \tag{0.25}$$

Therefore, Eq. 0.15 can be formed as,

$$\frac{\widetilde{U}_i(t+\Delta t)-2\widetilde{U}_i(t)+\widetilde{U}_i(t-\Delta t)}{(\Delta t)^2 sinc^2(b_i\Delta t/2)}=-{b_i}^2\widetilde{U}_i \tag{0.26}$$

Since $\widetilde{\boldsymbol{U}}=\boldsymbol{Q}^{\mathrm{T}}\widetilde{\boldsymbol{u}}$ (represented by the indicial form $\widetilde{U}_i=Q_{ij}\tilde{u}_j$), where index *i* represents the wave modes corresponding to three eigenvalues of the Christoffel matrix. Therefore, Eq. 0.26 can be also written as,

$$\frac{Q_{ij}\widetilde{u_j}(t+\Delta t)-2Q_{ij}\widetilde{u_j}(t)+Q_{ij}\widetilde{u_j}(t-\Delta t)}{(\Delta t)^2} \tag{0.27}$$

$$=-{b_i}^2 sinc^2(b_i\Delta t/2)Q_{ij}\widetilde{u_j})$$

Eq. 0.27 is expressed in a simple form by multiplying both sides by $\boldsymbol{Q}^{\mathrm{T}}$ or Q_{ji}. Therefore, Eq.28 can be derived due to the orthogonality of $\boldsymbol{Q}$,

$$\frac{\widetilde{u_j}(t+\Delta t)-2\widetilde{u_j}(t)+\widetilde{u_j}(t-\Delta t)}{(\Delta t)^2}=-Q_{ji}{b_i}^2 sinc^2(b_i\Delta t/2)Q_{ij}\widetilde{u_j}) \tag{0.28}$$

An inverse Fourier Transform is applied to Eq. 0.28 and the new scheme can be formed as,

$$\frac{\boldsymbol{u}(t+\Delta t)-2\boldsymbol{u}(t)+\boldsymbol{u}(t-\Delta t)}{(\Delta t)^2}=F^{-1}\{\boldsymbol{Q}\boldsymbol{B}\boldsymbol{Q}^{\mathrm{T}}F(\boldsymbol{u}))\} \tag{0.29}$$

where $\boldsymbol{B}$ is a diagonal matrix , where $B_{ij}=j^2(kv_i)^2 sinc^2(b_i\Delta t/2)\delta_{ij}$, and $j^2=-1$. Index *i*=1,2,3 represents the polarization direction of elastic wave in anisotropic material, respectively [52], [53].

Since we are solving a velocity-stress based formulation, a first-order wavenumber operator should be found similar to the *k-t* operator derived from the acoustic wave equation as mentioned in [33]. The derivation of the first-order operator is discussed in the following section.

By multiplying the right-hand side of Eq. 0.29 by $\boldsymbol{Q}^{\mathrm{T}}\boldsymbol{Q}$,

$$\frac{\boldsymbol{u}(t+\Delta t)-2\boldsymbol{u}(t)+\boldsymbol{u}(t-\Delta t)}{(\Delta t)^2}=F^{-1}\{\boldsymbol{QK^2Q}^{\mathrm{T}}\boldsymbol{QVQ}^{\mathrm{T}}F(\boldsymbol{u}))\} \tag{0.30}$$

where both $\boldsymbol{K}$ and $\boldsymbol{V}$ are diagonal matrixes and $\boldsymbol{B}=k^2\boldsymbol{K^2V}$,

$$\boldsymbol{K}^2=\begin{bmatrix} j^2sinc^2(b_1\Delta t/2) & 0 & 0 \\ 0 & j^2sinc^2(b_2\Delta t/2) & 0 \\ 0 & 0 & j^2sinc^2(b_3\Delta t/2) \end{bmatrix} \tag{0.31}$$

$$\boldsymbol{V}=\begin{bmatrix} (v_1)^2 & 0 & 0 \\ 0 & (v_2)^2 & 0 \\ 0 & 0 & (v_3)^2 \end{bmatrix}$$

If an inverse spatial FT is applied on Eq. 0.12,

$$\frac{\partial^2\boldsymbol{u}}{\partial^2 t}=F^{-1}\{j^2\boldsymbol{Q\alpha Q}^{\mathrm{T}}F(\boldsymbol{u})\} \tag{0.32}$$

where $\alpha_{ij}=\delta_{ij}v_i^2k^2$. Comparing Eq. 0.32 and Eq. 0.30, it's seen that the wavenumber term jk can be replaced by $k\boldsymbol{QKQ}^{\mathrm{T}}$.

Therefore, the first-order wavenumber operator $\boldsymbol{\nabla_k}$ is defined based on the spatial derivative using the pseudo-spectral method [34],

$$\boldsymbol{\nabla_k}(\boldsymbol{f})=F^{-1}\{\boldsymbol{kQKQ}^{\mathrm{T}}F(\boldsymbol{f})\} \tag{0.33}$$

where $K_{mn}=jsinc(b_m\Delta t/2)\,\delta_{mn}$, and $j^2=-1$ The index *m, n* equals 1,2,3, respectively. The wavenumber operator $\boldsymbol{\nabla_k}$ is a first-order partial derivative operator which works for the first-order velocity-stress formulation, i.e., the derivative of the particle velocity in Eq. 0.5 is expressed as,

$$\boldsymbol{\nabla_k}(\boldsymbol{v})=F^{-1}\{\boldsymbol{kQKQ}^{\mathrm{T}}F(\boldsymbol{v})\} \tag{0.34}$$

where each column of **Q** contains the eigenvector of **T** and $\mathbf{QQ^T=I}$, The **K** matrix is written as,

$$\boldsymbol{K} = \begin{bmatrix} jsinc(\frac{b_1\Delta t}{2}) & 0 & 0 \\ 0 & jsinc(\frac{b_2\Delta t}{2}) & 0 \\ 0 & 0 & jsinc(\frac{b_3\Delta t}{2}) \end{bmatrix} \tag{0.35}$$

and *j* is the imaginary unit. The derivative of velocity ***v*** can be written in a detailed indicial form as,

$$\frac{\delta v_i}{\delta x_m} = F^{-1}(jk_m F\ (F^{-1}(Q_{il}K_{lk}Q_{kn}{}^T v_n))) \tag{0.36}$$

and F, F^{-1} is the FT (Fourier Transform) and IFT (Inverse Fourier Transform), respectively. The symbol F^{-1} is the short form of spatial FT in the wavenumber space. The variable $\tilde{v}_n$ is the spatial FT of velocity component v_n, such that,

$$\tilde{v}_n(k,t) = F(v_n(x,t)) \tag{0.37}$$

where a similar operation on the displacement *U* is shown in Eq. 0.17 of the paper. The idea behind Eq. 0.36 is to first project velocity in the cartesian coordinate on the direction of ***Q,*** which is the eigenvector of the Christoffel matrix. The decomposed velocity components are multiplied by the k-space operator and is projected back to the Cartesian coordinate again as shown in Eq. 36. In this paper, the decomposition is based on velocity since we focus on first-order stress-velocity wave equations. Eq. 0.36 can be also written in the compact form,

$$
\begin{aligned}
&\nabla(v)_{im} = F^{-1}(jk_m V_i)),\\
&V_i = F(F^{-1}(Q_{il}K_{lk}Q_{kn}{}^{T}F(v_n))),\\
&or\\
&V_i = F(F^{-1}(M_{in}F(v_n)))\\
&where\\
&M_{in} = Q_{il}K_{lk}Q_{kn}{}^{T}\\
&K_{lk} = K_{lh}\delta_{hk}\\
&\delta_{hk} = 1, h = k\\
&\delta_{hk} = 0, h \neq k
\end{aligned}
\tag{0.38}
$$

where $\nabla(v)_{im} = \dfrac{\delta v_i}{\delta x_m}$, the repeated index follows the Einstein summation rule.

The divergence of stress $(\nabla \bullet \boldsymbol{\sigma})$ can be also written as a function of the k-space operator, such that,

$$
\frac{\delta \sigma_{ij}}{\delta x_j} = F^{-1}(jk_m F(F^{-1}(Q_{nl}K_{lk}Q_{ki}{}^{T}\sigma_{mn})))
\tag{0.39}
$$

Since the divergence of stress tensor is a vector, Eq. 0.39 can be written as a compact form such that,

$$
\begin{aligned}
&(\nabla \bullet \boldsymbol{\sigma}) = (S_i, S_j, S_k)\\
&S_i = \sigma_{im,m}\\
&S_i = F^{-1}(jk_m\theta_{mi})\\
&\theta_{mi} = F^{-1}(jk_m F(F^{-1}(Q_{nl}K_{lk}Q_{ki}{}^{T}F(\sigma_{mn}))))\\
&or\\
&\theta_{mi} = F^{-1}(jk_m F(F^{-1}(M_{ni}F(\sigma_{mn}))))\\
&where\\
&M_{ni} = Q_{nl}K_{lk}Q_{ki}{}^{T}\\
&K_{lk} = K_{lh}\delta_{hk}\\
&\delta_{hk} = 1, h = k\\
&\delta_{hk} = 0, h \neq k
\end{aligned}
\tag{0.40}
$$

where *m, n, l, h* is dummy index using Einstein Summation rule and Subscript *i, j, k* is the direction in Cartesian coordinate [52], [53]..

An example is given to show the details of above operations, the first-order wave equation in the x-direction is discussed in the Appendix.

The k-space operator is based on the first-order velocity-stress formulation, therefore the variables used are velocity components in the paper. A detailed discussion on wave decomposition based on displacement is discussed in [39], which proposes a very efficient low-rank mixed-integral operator for the wavefield decomposition in anisotropic elastic wave equation [39].

The coupled wave equations can be solved iteratively by implementing a finite difference scheme in the temporal domain. The numerical method is programmed and implemented in MATLAB and is based on the framework developed for acoustic wave propagation in soft materials such as tissue and liquid [32]. A pseudocode and flowchart (Fig. 2-1) is given to show how the k-space operator works in the proposed framework,

---

set up
mesh and material properties
initial values of velocity and stress
time step Δt and length N

---

for i=1: N step
{
compute divergence $\nabla \bullet (\sigma(\mathbf{x},i))$ using Eq. 39
update velocity $\mathbf{v}(\mathbf{x},i+1) = \mathbf{v}(\mathbf{x},i)\Delta t + \nabla \bullet (\sigma(\mathbf{x},i))\Delta t$ using Eq. 4
update gradient of velocity $\nabla \mathbf{v}(\mathbf{x},i+1)$ using Eq. 38
update stress $\boldsymbol{\sigma}(\mathbf{x},i+1) = \boldsymbol{\sigma}(\mathbf{x},i)\Delta t + \mathbf{C} : \nabla \mathbf{v}(\mathbf{x},i+1)$
if {i==N;
break;
end}
set i=i+1;
}
end

(a)

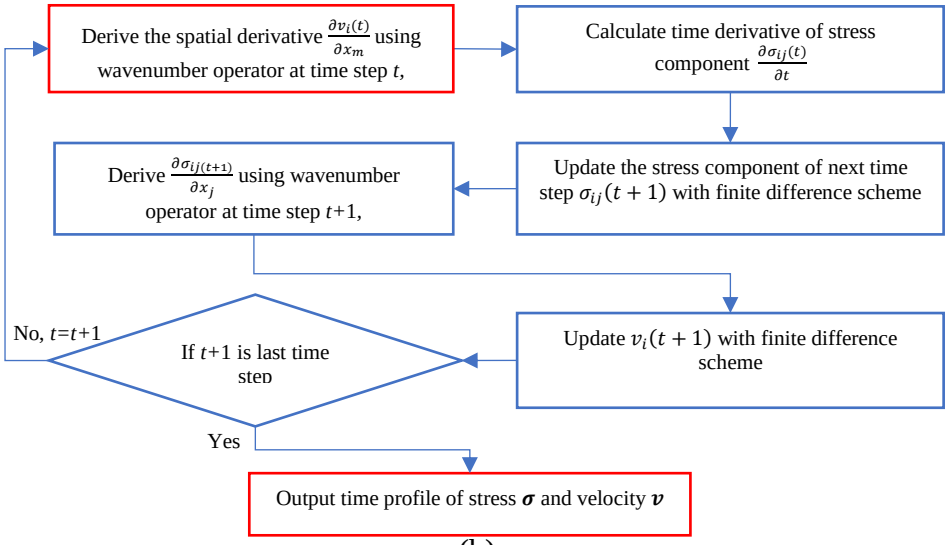

(b)

Figure 2. 1 (a) Pseudocode and (b) flow chart of the proposed simulation framework

2.4. Wave Propagation With Crack-Like Strong Discontinuities

Most existing wave propagation simulations using the k-space method considering the heterogeneous materials are for discontinuities introduced by acoustic properties mismatch. In structural materials, other types of discontinuity, such as crack, delamination, and sharp notches, can appear under the service conditions. One unique focus of the proposed study

is the investigation of this type of discontinuities as the simulation tool will be eventually used for damage detection purposes.

The above-mentioned formulation is readily available for application to crack problems, by assigning different material properties to the computational grid in the k-space formulation. The major difficulty is the computational stability due to the discontinuity introduced by inserted cracks. To ensure the stability of the numerical method, the time step should be selected properly. Therefore, the *CFL* (*Courant –Friedrichs-Lewy)* condition [33] [54], [55] is used as the guideline for the stability control. It is shown that the time step in the simulation should be smaller than the time step of the fastest wave travelling across one mesh. The *CFL* condition relates the mesh size and the time step in the numerical model as mentioned in [54], [55]. The *CFL* number is defined as,

$$\begin{aligned} CFL &= \frac{V_0 \Delta t}{\Delta x}, \\ V_0 &= \max(\mathbf{V}) \end{aligned} \tag{2.4.41}$$

where Δt is the time step and Δx is the mesh size, and V_0 is the maximum velocity in the material. In the derivative calculation, the wavenumber k is replaced by the k-space operator in Eq. (0.33). It's seen that,

$$\begin{aligned} \hat{K}_n &= j \sin c(\frac{b_m \Delta t}{2}) \delta_{mn}, \\ b_m &= v_m k \end{aligned} \tag{2.4.42}$$

where $\hat{K}_n$ is the diagonal terms in $\boldsymbol{K}$ in Eq. 0.35. The symbol v_m is known to be the phase velocity of wave propagation in generalized anisotropic material. It's also known to be the eigenvalue derived from the Christoffel equation as discussed in [56]. Therefore, the CFL condition in Eq. 2.4.41 is generalized into the form,

$$CFL = \frac{V_0 \Delta t}{\Delta x}, \qquad V_0 = \max(\mathbf{v}) \tag{2.4.43}$$

We discussed the CFL condition of the demonstration examples, where the material is transversely isotropic. It's known that for transversely isotropic material, the maximum phase velocity along the symmetric axis will be the compressional wave speed V_P ($V_p = \sqrt{\frac{C_{11}}{\rho}}$). For isotropic material, the maximum phase velocity will also be the compressional wave speed due to the same wave speed in any direction. Therefore, V_p is used in the CFL equation in the proposed study. However, for general anisotropic material, we should write CFL condition in terms of phase velocity **v** because it depends on both Stiffness matrix and direction**.** The choice of *CFL* number should be carefully selected considering the balance between computational cost and numerical stability and accuracy. The criterion of *CFL* number to provide the numerical stability using k-space method is also described in [33] [41] [20], such that

$$\sin(\frac{\pi CFL}{2}) \leq \frac{V_0}{V_{max}} \tag{2.4.44}$$

which provides the stability condition using the ratio between V_0 and V_{max}, where V_{max} is the maximum wave speed supported by the physics model. The left-hand side of Eq. 2.4.44 is bounded between -1 to 1 due to the nature of sinusoidal function. The condition can be easily satisfied by setting the $V_{max\ larger}$ than V_0 by refining the grid size of numerical model.

The other factor needs to be considered is the accuracy of numerical simulation, especially when the material is heterogeneous where many cracks and inclusions exist. Such error needs to be compensated by refining the mesh size and time step. Based on the Nyquist

Sampling Theorem [35], the sampling frequency should be at least twice or higher than the highest frequency contained in the signal. Eq. 0.36 shows the relation between the time step Δt and the frequency,

$$\Delta t = \frac{1}{f_{sample}} \tag{2.4.45}$$

$$f_{sample} \geq 2 f_{signal}$$

where f_{sample} is the sampling frequency and f_{signal} is the highest frequency component in the signal. Therefore, f_{sample} should be properly selected to avoid aliasing in the simulation. Nyquist theorem can also be represented by the *CFL* condition based on Eq. 2.4.46, which is also discussed in the k-space method used in wave propagation in tissue in [33], such that,

$$CFL \leq \frac{V_0}{V_{max}} \tag{2.4.46}$$

Eq. 2.4.44 and Eq. 2.4.46 give restrictions on the selection of *CFL* number in consideration of stability and accuracy in the k-space method [33] [41] [20]. In the current study, *CFL* number is set to 0.3 for homogeneous material based on a previous study [41]. For the model with discontinuity such as cracks and delamination, it's is shown that a *CFL* number of 0.1 can provide good results for all investigated cases with a single crack or a group of cracks in the following examples in Section 4.

2.5. Model Verification and Validation

2.5.1. 2d Isotropic Solids

A simple isotropic material 2D model is verified by comparing the k-space result and the FEM result. A 2D aluminum model of 0.1 m by 0.1 m is used for demonstration. The material properties are given in

. A time varying point source is applied in the middle of the model. A sensor is located 0.05 m from the left of the source. The FEM simulation is done by the commercial software ABAQUS using 1,000,000 CPS4R elements. In the proposed framework, only the time of arrival and the waveform of the first-time window is important for damage detection purpose. Thus, only the first-time window signal is shown in the figure. Results are shown in Fig. 2-2. In Fig. 2-2, it's seen that the time of arrival and wave in the first-time window match well between k-space and FEM solutions. The percentage difference is also presented in the figure. To quantify the comparison, the compression wave speed is estimated using the k-space and FEM and they are compared to the theoretical value, respectively. The error in the first-time window between k-space and FEM solution is within 6%, respectively as seen in Fig. 2-2. The reference line is added indicating the end of the first-time window. In the FEM model, a free boundary is used and reflections using FEM can be seen in Fig. 2-2. An absorption boundary layer is used in the k-space model. Therefore, only the error of first-time window is compared.

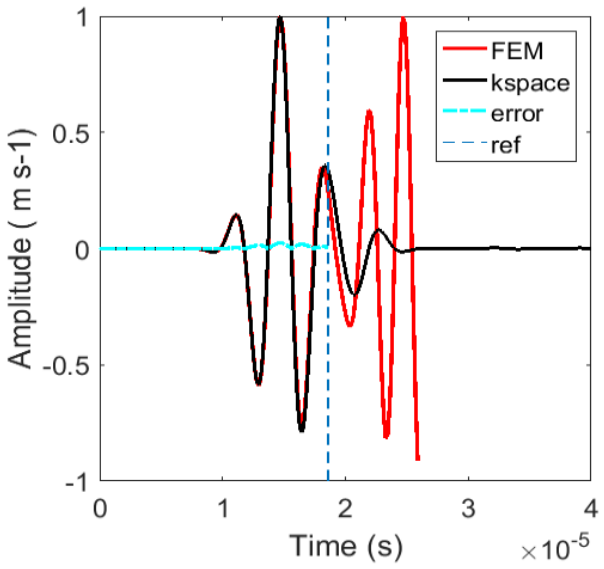

Figure 2. 2 Velocity recorded by the sensor in isotropic 2D model

Table 2. 1 Compressional wave speed comparison

	k-space	FEM	theoretical
V_p (m s^{-1})	5077.3	5087.9	5282.1

2.5.2. 2d Anisotropic Solids

Wave propagation in homogeneous, anisotropic material in 2D case is performed and is compared with the analytical solution for verification. The analytical solution for apatite is provided in [57]. For easy comparison with the analytical solution, the material of the demonstration example is also apatite, which is homogeneous and transversely isotropic. Material properties are in Table. 2-2. A concentrated force is applied on the horizontal direction in the 2D model. The symmetry axis of the material is aligned with the horizontal direction. The source is time varying with the shape of the Ricker wavelet [58]. The source has a central frequency of 500 kHz with a time delay of 6μs. The 2D model is 20 cm by 20

cm with the source applied in the center. The model is discretized by 400 by 400 grid points in the k-space model. The *CFL* number is set to be 0.1.

Table 2. 2 Material properties of apatite

	C_{11}(Pa)	C_{12}(Pa)	C_{13} (Pa)	C_{33} (Pa)	C_{44} (Pa)	ρ(kg m^{-3})
Apatite	16.7e10	2.31e10	6.6e10	14e10	6.63e10	3200
Clay shale	6.66e10	1.97e10	3.94e10	3.99e10	1.09e10	2590

One receiver is in the horizontal direction which is 0.08 m from the source. The velocity on the horizontal direction is compared with the analytical solution [59]. Figure 2. 3 shows analytical solution compared with the numerical result of velocity and displacement, respectively. Almost identical agreement is observed between the analytical solutions and numerical results. To quantify the difference, the relative error is shown together in the figure. The highest error is 6% as seen in Fig. 2-3(a) and 5% in Fig. 2-3 (b).

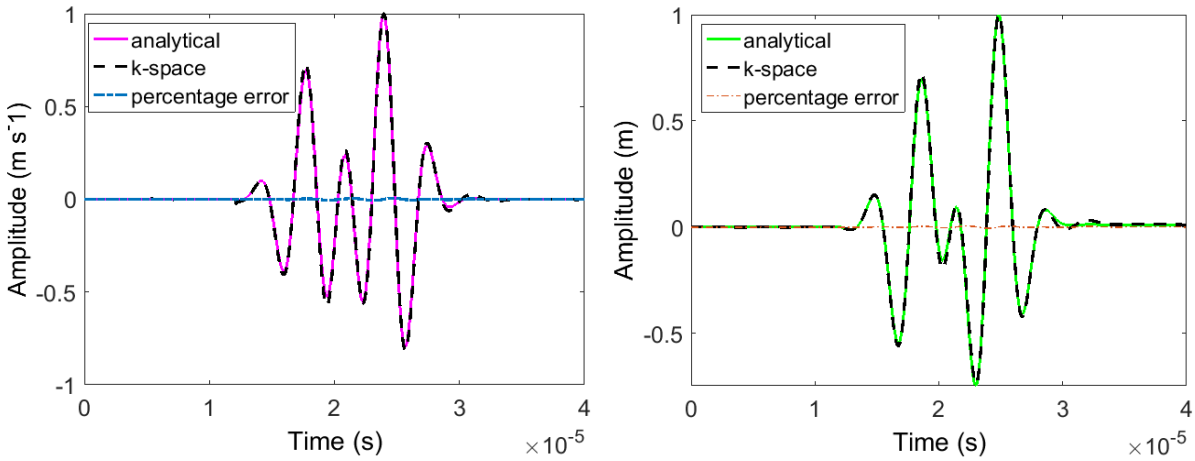

Figure 2. 3 Comparison of the numerical simulation with analytical solutions, a) normalized velocity(left), b) normalized displacement(right)

2.5.3. 3d Anisotropic Solids

The next verification example is the wave propagation in clay shale (i.e., homogeneous and anisotropic material) in 3D. Similar problem was solved using the spectral scheme and the analytical solution along the symmetry axis was provided in [60]. Again, for demonstration purpose, the material used in the 3D model is also clay shale. The size of

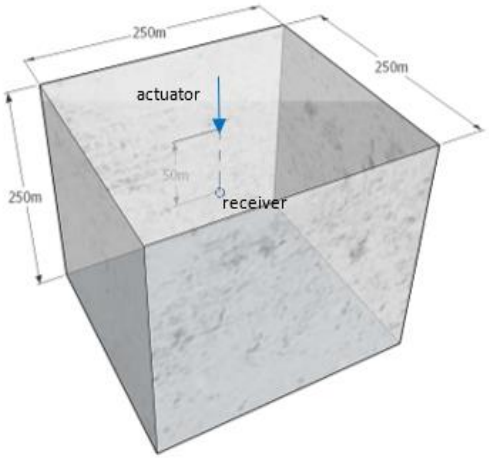

Figure 2. 4 An anisotropic model in 3D

the model is 250 m by 250 m by 250 m with a mesh size of 5 m in all directions in the k-space model. The source is a Ricker wavelet with the central frequency of 50 Hz and a time delay of 0.1 s, which is applied on the top surface in the direction of symmetry axis. The receiver is 50 m from the actuator along the symmetric axis. The time step is set to be 2.958e-4 *s* and the *CFL* number is 0.1.

In order to verify the 3D model, we compared numerical result with the analytical solution [60], as seen in Figure 2. 5. Again, almost identical solutions of the analytical methods and the proposed numerical framework can be observed.

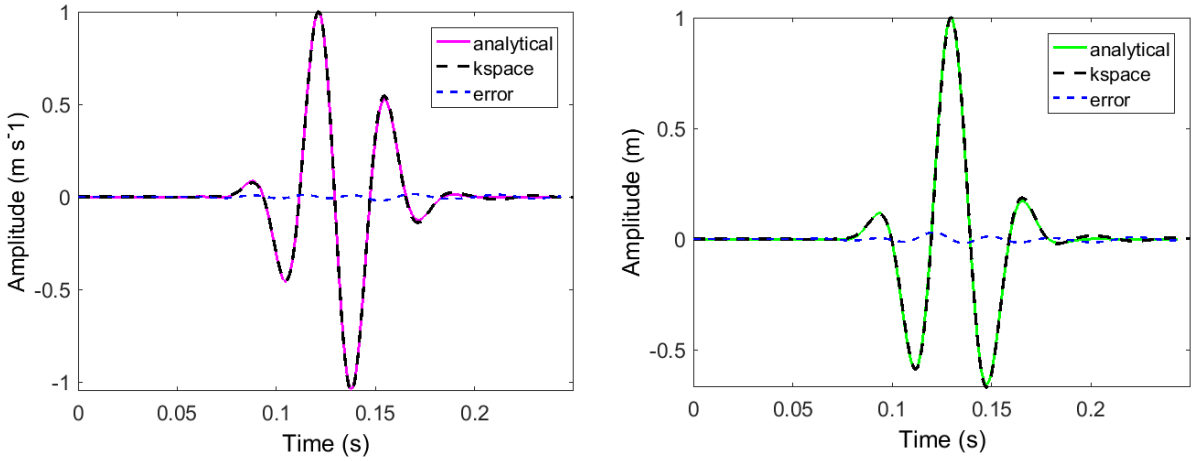

Figure 2. 5 Comparison of the numerical simulation with analytical solutions. a) Normalized velocity(left); b) Normalized displacement(right)

The convergence on the mesh size is investigated in this section as it is related to the computational efficiency and accuracy for large-scale simulations. For damage detection problems, signal features are usually employed as the indicators for damage, such as the wave amplitude and the time of arrival. In the case of wave propagation in anisotropic materials in the 3D domain, it is observed that the wave amplitude is not affected much by the mesh size but the time of arrival changes as the mesh size changes as seen in Figure 2. 6(a). A Central Difference scheme is compared with the Forward Difference in time domain. The time of arrival of each waveform is found by setting a threshold value, which is shown as the reference line in Fig. 2-6(a) and Fig. 2-6(b). The time of arrival is shown in Fig. 2-6(c). Both schemes are converged when mesh size is equal to or smaller than 6.25m.

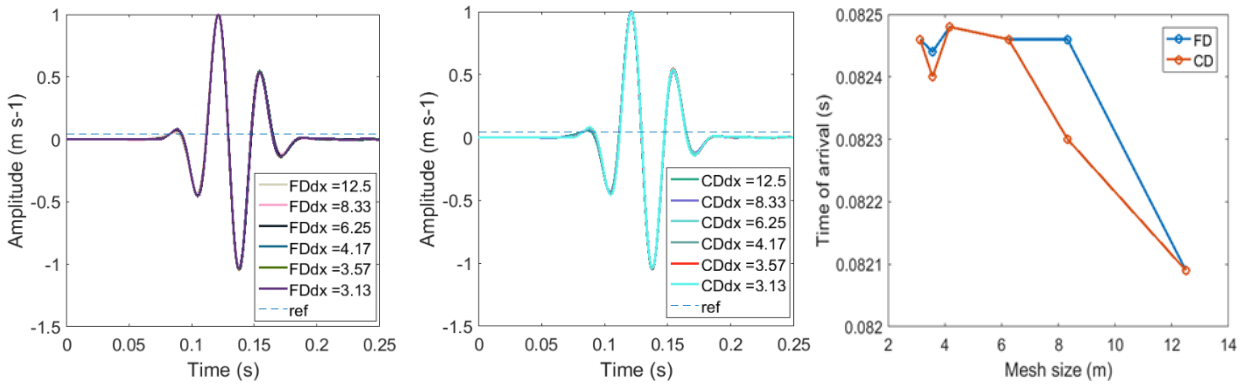

Figure 2. 6 Mesh convergence study. a) received wave form for different mesh size using FD (Forward Difference); b), received wave form for different mesh size using CD (Central Difference); c) time of arrival vs. mesh size for CD and FD

2.6. Verification of the Crack Model

Above examples are for the general verification on homogeneous material without considering crack-like discontinuities. This section is for the verification of the crack model. Since analytical solutions for crack models are rarely found in the open literature, the verification is done by comparing the proposed method results with the finite element results using ABAQUS. The model is a 0.4 m by 0.1 m with a crack near the left end as shown in Fig. 2-7. The crack tip meshing is enriched for the convergence. The element type is CPS4R and solved explicitly in the FEM model. A time varying pressure is applied on the left boundary to see the wave propagation through crack. The crack in the finite element model is a mathematically sharp crack [61]. The crack has a length of 0.08m, perpendicular to the length of model and is 0.05 m from the left edge in Figure 2. 7

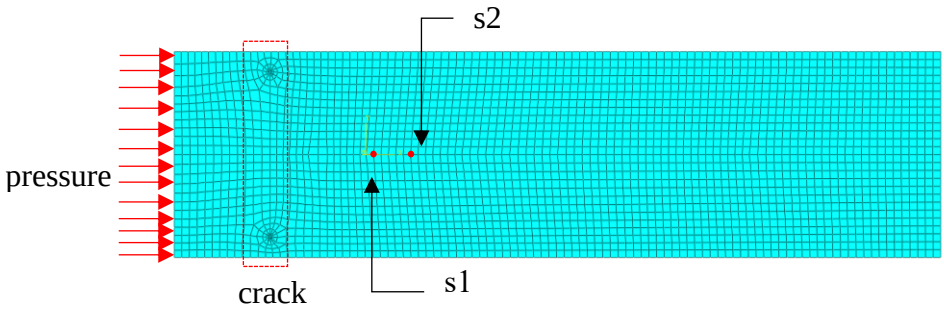

Figure 2. 7 2D crack model. s1 and s2 are sensors

The wave amplitude at receivers s_1 and s_2 are used for the verification purpose. They are 0.07m and 0.08m, from the left edge, respectively. It should be noted that, since an absorption boundary condition is used in the k-space method, the reflected wave from the boundary is not considered in the current study as the focus is on the transmitted wave. Therefore, only features like time of arrival and amplitude in the first-time window are considered in this paper. It is seen that the results of the k-space method agree with the FEM results very well in Figure 2. 7. To quantify the results, the relative percent error is computed and the highest difference turns out to be 2.6% as shown in Fig. 2-8(a) and 2(b).

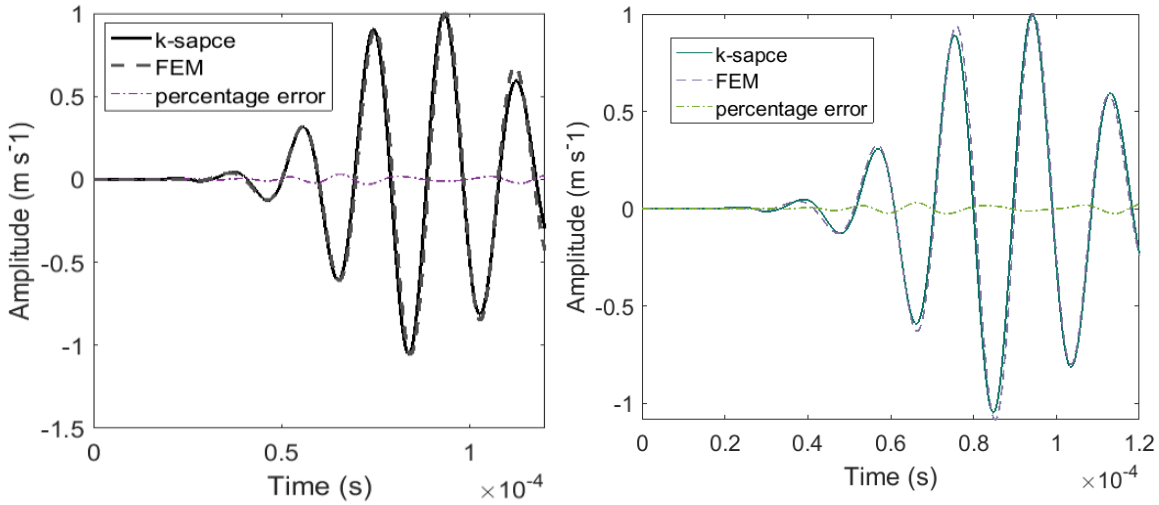

Figure 2. 8 Time profile of normalized velocity at sensor s1(left) and s2(right) of crack model using FEM gap model and k-space solver

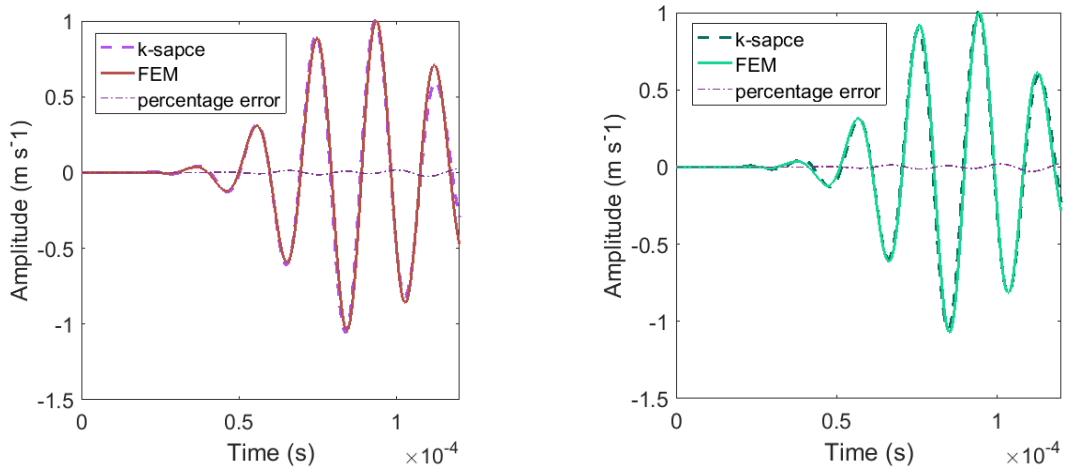

Figure 2. 9 Time profile of velocity recorded by s_1 and s_2

In the literature, internal damage (e.g., inclusions and sharp notches) has also been modelled in the FEM. This is usually achieved by removing a layer of element in the model to create finite width discontinuity. This type of discontinuities is widely seen in structures due to the imperfections, manufacturing errors, or a blunted crack due to overloading. A numerical model is designed to reflect this scenario. A gap of 8e-2 m is created in both the FEM and the k-space model. The other parameters are same with the mathematical crack

model. The results are shown in Figure 2. 9. Again, excellent agreement is observed between the FEM solution and the proposed k-space solution. The relative error is quantified that the highest error is 3% in both scenarios as shown in Fig. 2-9.

2.7. Numerical Simulation Results for Representative Engineering Applications

The previous section focuses on the model verification and validation using simple models. Once the proposed method is verified, it can be applied to investigate the engineering wave propagation problems with cracks. Three examples are used to illustrate the capability of the proposed method: 1) a 2D model with single or multiple cracks. This represents the fatigue crack problems in commonly used fuselage structure in aircraft; 2) an embedded subsurface crack within an isotropic solid. This represents the ultra-high cycle fatigue in metallic components where the crack is usually initiated internally. 3) the delamination in 3D anisotropic layered structures. This represents the fatigue or impact damage of carbon fiber reinforced composite laminates. Details are discussed below.

2.7.1. 2d Model With A Single or Group of Cracks

The simulation target is a 10cm by 2cm aluminum model discretized by 252 by 62 grids. The grid spacing is 3.68e-2 cm in both directions. A centered crack of 0.6 cm in length and one grid spacing in width is considered. The material in the crack is air. The density is set to be 1.2041 kg/m^3 and the compressional wave speed is 343.2 m/s. A point source in the *x* direction is applied on the top edge. The source is a 5.5cycles tone-burst of 50 kHz. A receiver is located at 7 cm from the source along *x*-direction in Figure 2. 10(a), where the scale in figure is in mm. It shows the contour of the normalized velocity.

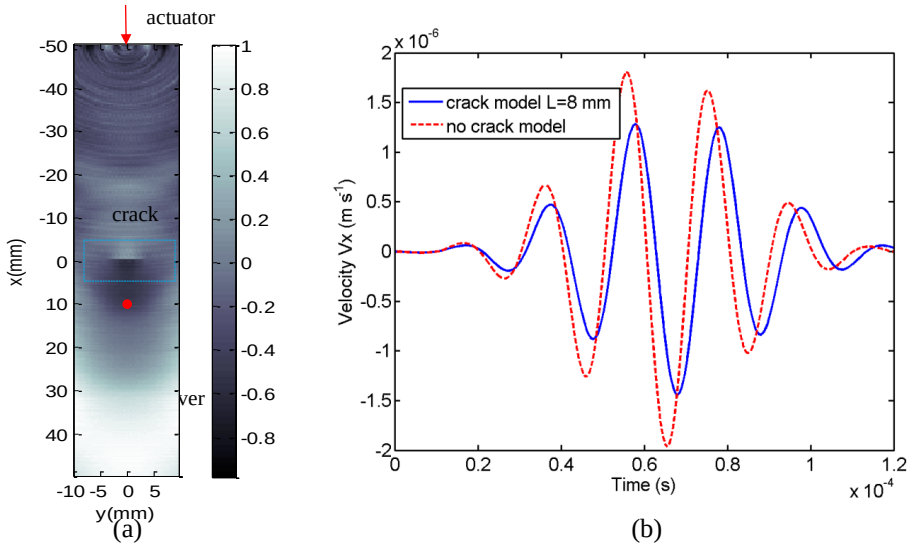

Figure 2. 10 (a) Contour of normalized velocity of cracked model, (b) velocity at the receiver, non-crack model (dashed line) and crack model (solid line)

Table 2. 3 Material properties of aluminum

	E(Pa)	$\boldsymbol{G}$**(Pa)**	**v**	$\boldsymbol{\rho}$**(kg**$\boldsymbol{m^{-3}}$**)**
aluminum	79Gpa	1.31e10	0.33	2770

The time history of received wave at the sensor location is shown in Figure 2. 10(b). The wave of a non-cracked aluminum model is plotted together for comparison. It is clearly seen that the amplitude drops and phase changes due to the existence of crack. This has been experimentally observed and explained empirically in [13].

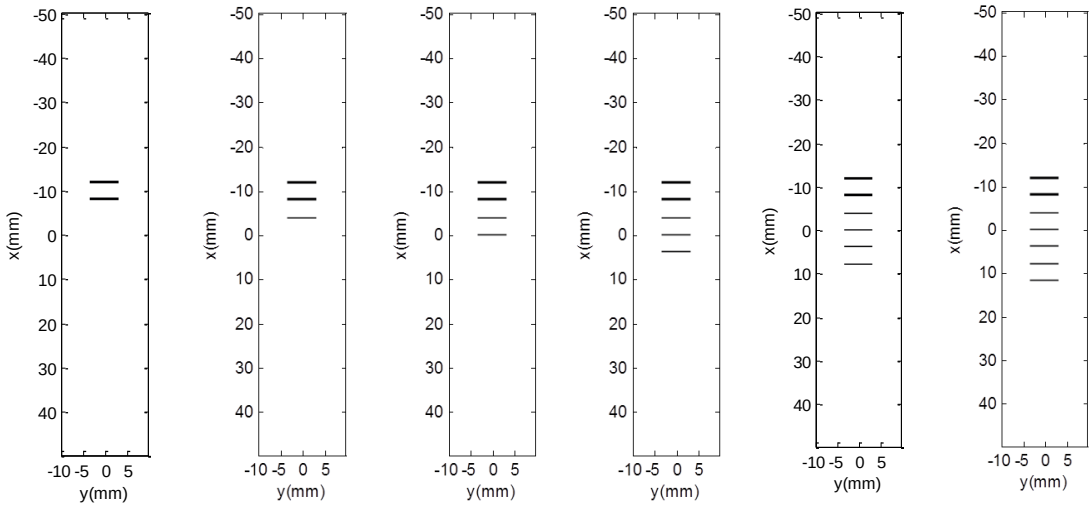

Figure 2. 11 Crack distribution at various crack number

It has been reported that the crack length and the number of cracks both have significant effect on the received wave signals [30]. To see the effect of crack number and length on wave propagation, parametric studies are performed using the proposed simulation method. Distribution of cracks is shown in Figure 2. 11 .The number of cracks starts from 2 to 7. Cracks are distributed uniformly where the gap between adjacent cracks is 4 mm. Results are shown in Fig. 2- 2-12(a)- (c), where the normalized velocity amplitude and time of arrival when different number of cracks is considered at a specific crack length is shown. It's seen that the amplitude depends on number of cracks that the wave amplitude decreases with the increase of crack numbers. The time of arrival has a dependence on crack number as well that the time of arrival is delayed as the crack number increased. The relationship appears to be nonlinear.

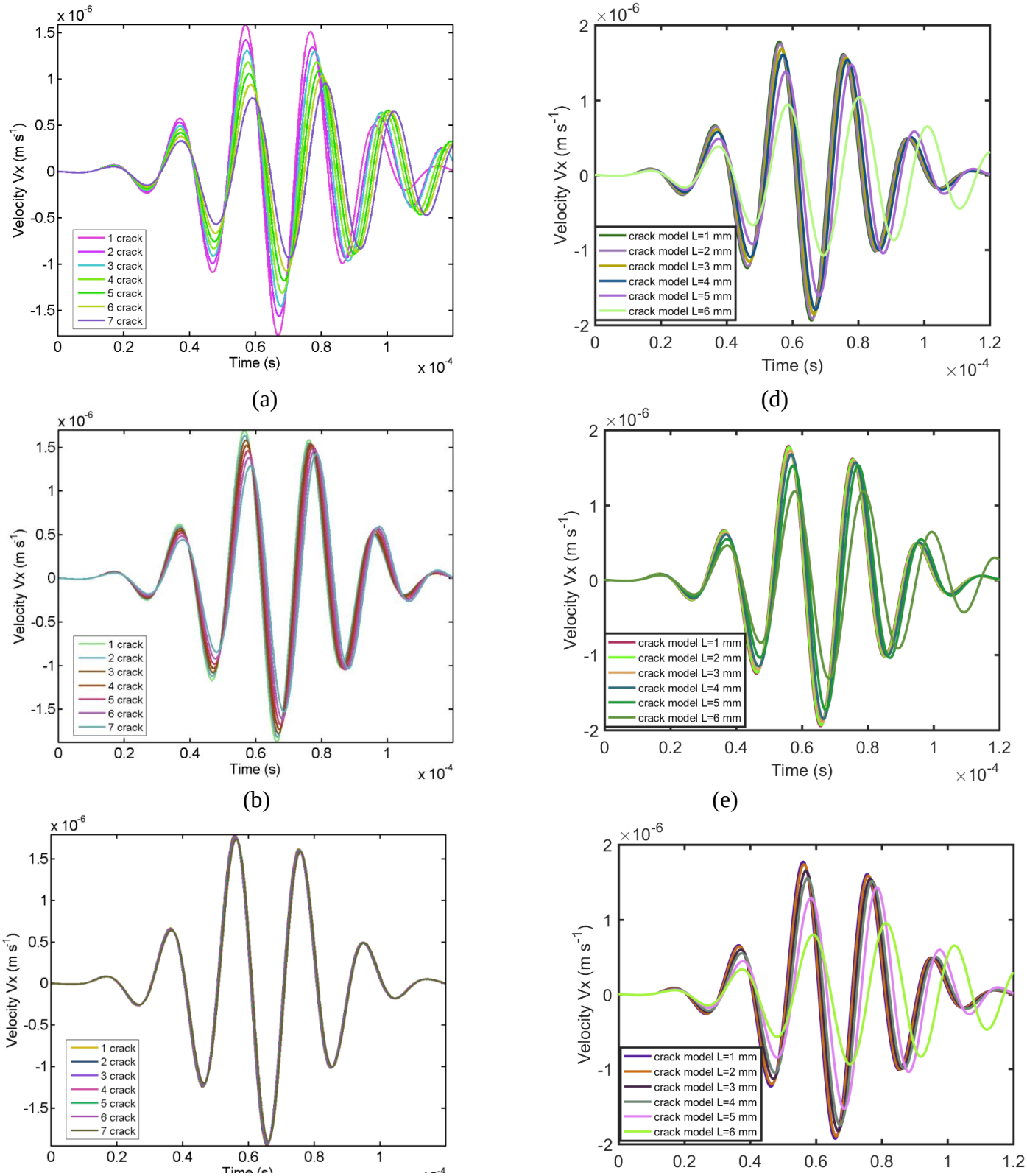

Figure 2. 12 (a)-(c) Horizontal velocity of various crack number when the length of each crack is 6 mm, 5 mm and 2 mm, (d)-(f) Horizontal velocity v_s of various crack length when number of cracks is 6,4, and 2, respectively

The effect of crack length on wave propagation is also discussed. Figure 2. 12(d)-(f) shows received wave in the case of different crack length when the number of cracks is constant in each figure. For small crack lengths, the change of waveform is not significant. Amplitude and time of arrival of crack length and crack numbers are compared to see their effect on wave propagation. It's seen when the crack length is bigger than 3 mm in this case, the wave amplitude decreases significantly as the crack length increases as shown in Figure 2. 13(a). The time of arrival also increases as the increase of crack length as shown in Figure 2. 13(b). There is a sudden jump on time of arrival when number of cracks increased from 3 to 4 at the same time the crack length equals 6mm and 7 mm. Compared with the effect of the number of cracks, the crack length has much more significant impact on the wave amplitude and the time of arrival.

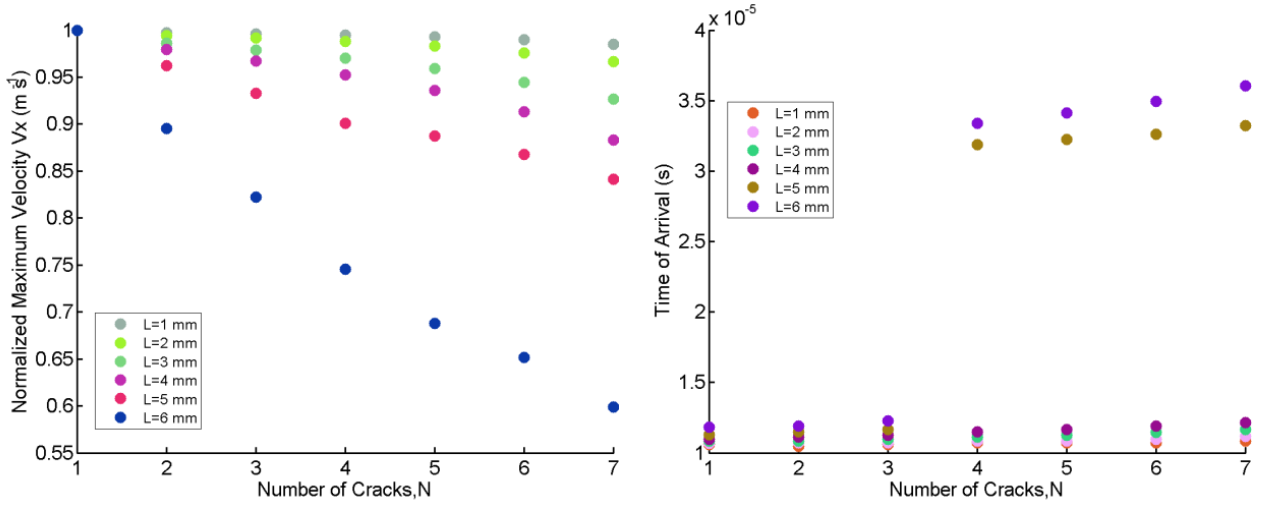

(a) (b)

Figure 2. 13 (a)-(c) Horizontal velocity of various crack number when the length of each crack is 6 mm, 5 mm and 2 mm, (d)-(f) Horizontal velocity v_s of various crack length when number of cracks is 6,4, and 2, respectively

2.7.2.Delamination In 3d Isotropic Solids

The example is aluminum material with a disc-like delamination in the 3D domain. Material properties are shown in Table. 2-3. The model is 0.05 m by 0.05 m by 0.001 m and is discretized by 43 by 43 by 22 elements. The location of the damage is shown in Figure 2. 14. The damage is 4.55e-5 m from the top surface. A total of 11 receivers (A1-S7, S9-S12) and one actuator (S8) are placed in a circular manner on the surface. The radius of the sensors is 0.2 m.

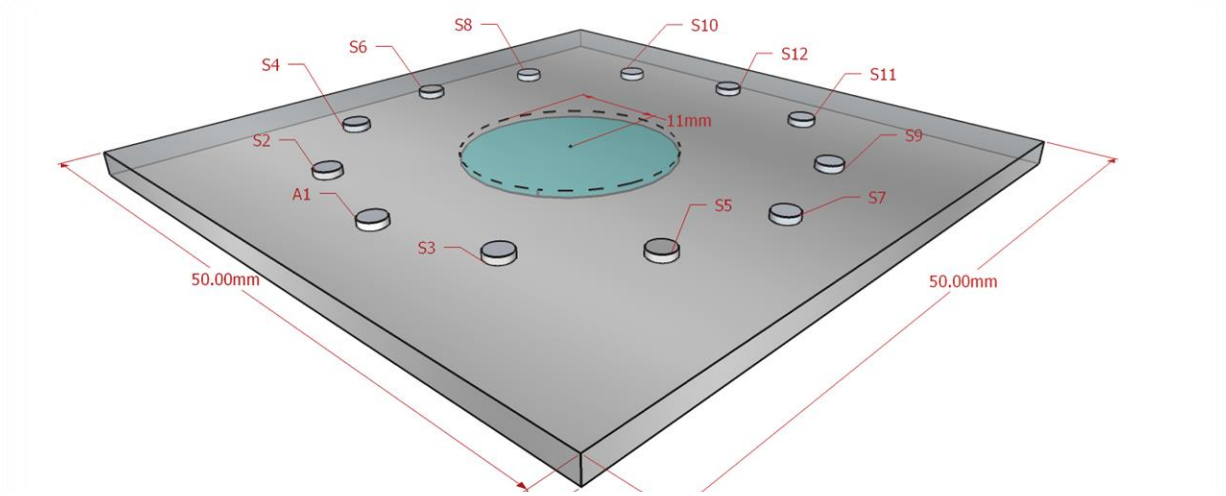

Figure 2. 14 Illustration of the model of 3D isotropic solid with embedded damage

Sensor 8 excites a tone-burst signal and other sensors are receivers. The time profile of horizontal velocity is shown in Figure 2. 15. Again, current study focuses on the waveform in the first-time window and time of arrival since they are important features in damage detection problems. The waveform of pristine conditions (or no damage) in the first-time window are shown together for comparison. The behavior of wave propagation is complex and needs further investigation in the future.

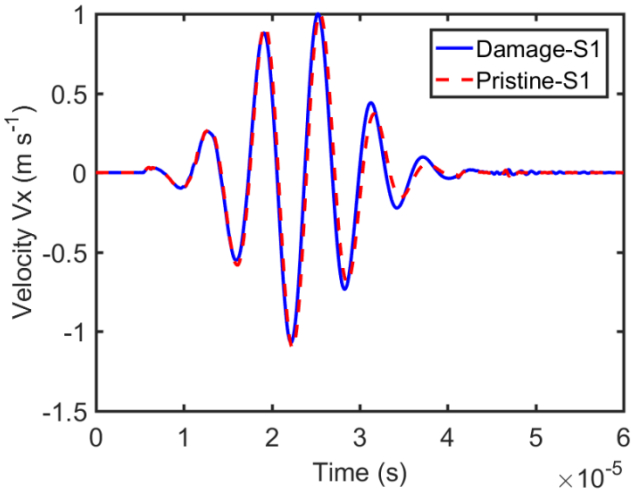

(a) Normalized Horizontal velocity at Sensor 1

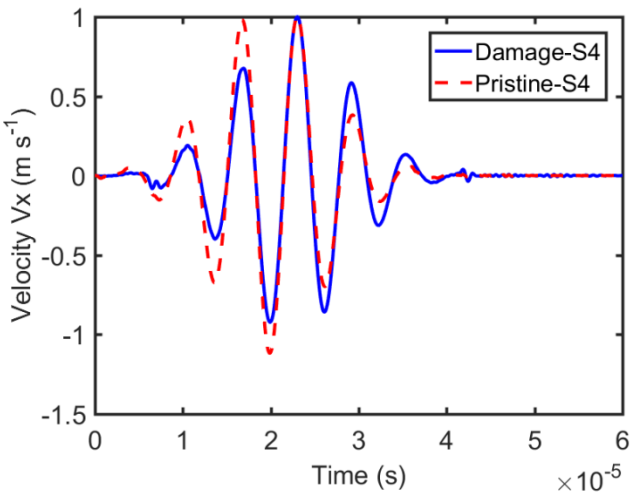

(b) Normalized Horizontal velocity at Sensor 4

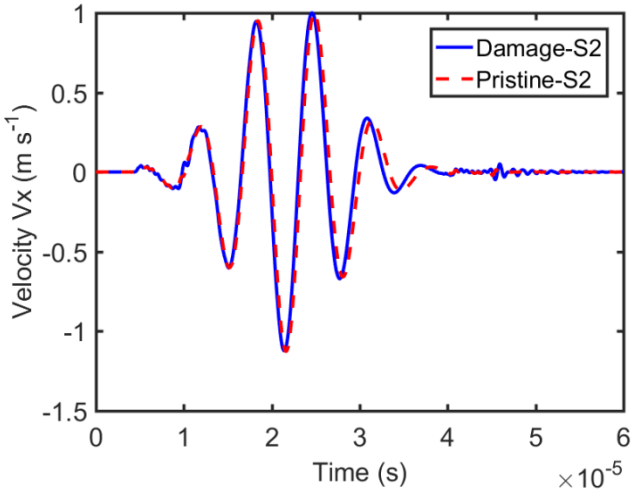

(c) Normalized Horizontal velocity at Sensor 2

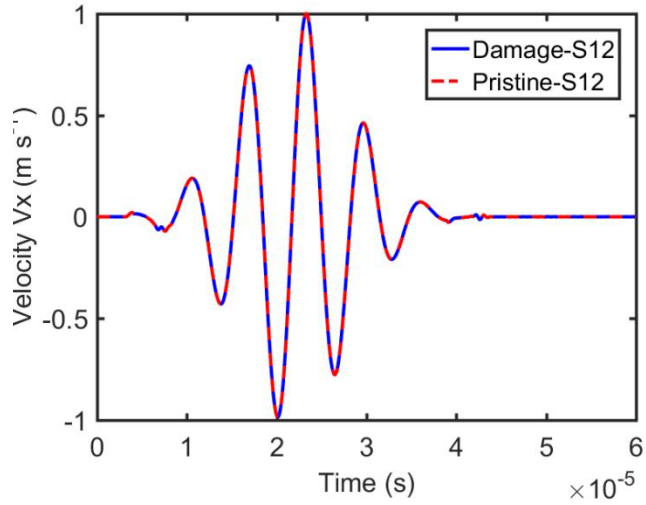

(d) Normalized Horizontal velocity at Sensor 12

Figure 2. 15 Normalized velocity at different receivers

2.7.3. DELAMINATION IN 3D ANISOTROPIC LAYERED SOLID

Composite laminates with delamination is modelled to investigate effect of delamination on wave propagation in composites. The material is Torayca T700G unidirectional carbon-prepreg material [30]. The material is widely used in aircraft and sports goods. Material

properties are provided in Table 2. 4. The laminate has 12 plies with each ply in different fibre direction. The geometry is 0.02 m by 0.015 m by 0.0024 m for demonstration purpose. The fiber direction of each ply from top surface to bottom surface is [0°/ 90°/ 90° /45°/ -45°/ 90°/90°/ -45°/ 45°/ 90°/ 90°/ 0°], respectively. Total of 6 pairs of sensors are attached on top surface as shown in Figure 2. 16. S5 is the actuator exciting a 5.5 cycles tone-burst of 150 *kHz*. The location of a square delamination is shown in Fig. 2-16. The delamination is modelled as a separation between the Ply 5 and Ply 6.

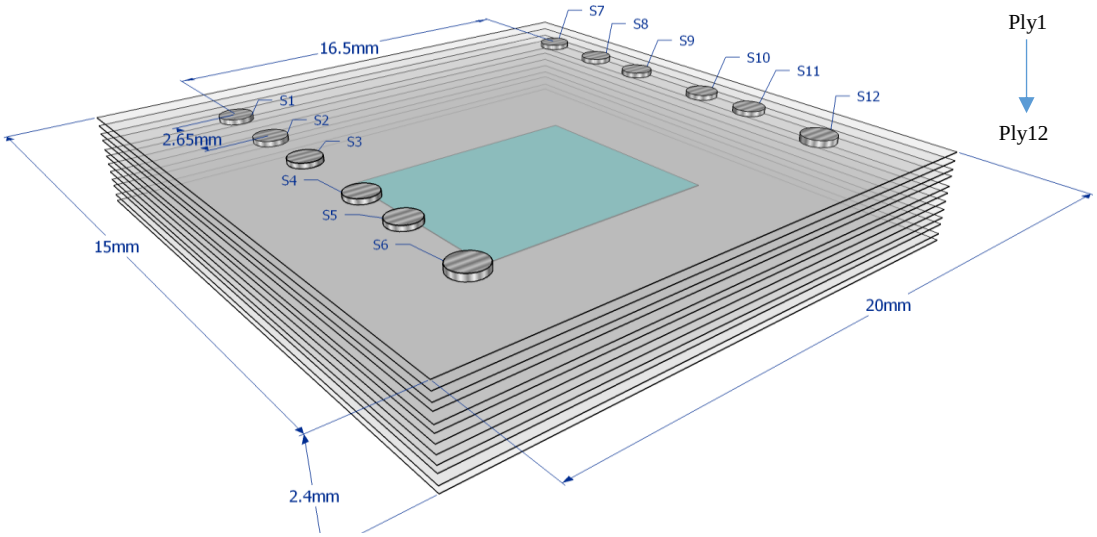

Figure 2. 16 Composite laminate with delamination between plies

Table 2. 4 Material properties of *Torayca* T700G

E_{11}(*Gpa*)	E_{22}(*Gpa*)	E_{33}(*Gpa*)	G_{12}(*Gpa*)	G_{23}(*Gpa*)	G_{13}(*Gpa*)	ν_{12}	ν_{23}	ν_{13}
127.5	8.4	8.4	6.2	3.4	6.2	0.31	0.36	0.31

shows the time profile of wave propagation recorded by different sensors. The wave recorded by sensor 3, 5 and 9 in the delamination model show no major difference with the wave of non-delamination (pristine) model. For sensor 2,4 and 6, it's found that the wave going through the delamination area contributes to the amplitude decay, but almost no difference in the time of arrival compared to the wave in the non-delamination model. Comparison of the waveform from sensor 6 and sensor 9 with the results of pristine model are shown for brevity, respectively. Again, it is shown that the delamination has less impact on the received signal which was also mentioned in [30].

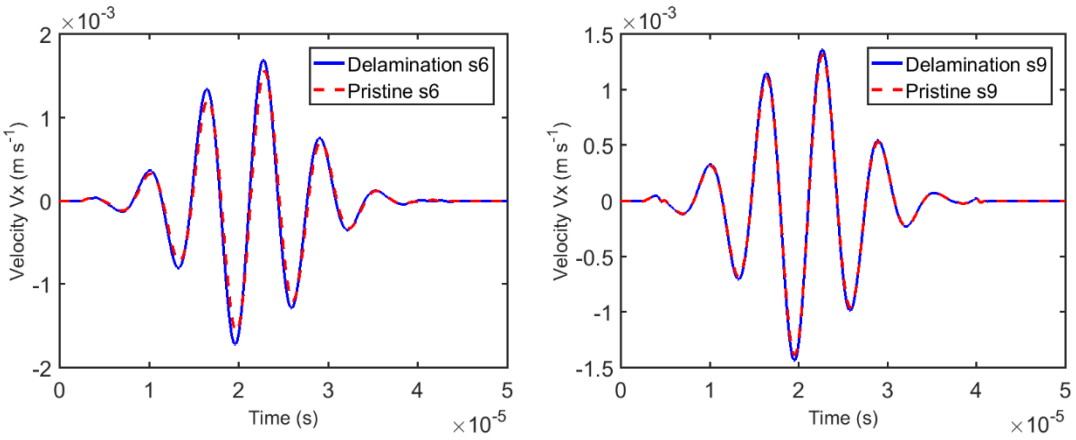

(a) Horizontal velocity at sensor 6 **(b) Horizontal velocity at sensor 9**

Figure 2. 17 (a), (b) Horizontal Velocity at different receivers

2.8. Computational Efficiency of Proposed Framework

As mentioned in the previous sections, the implementation of k-space method highly increases the computational efficiency. To quantify the efficiency, the CPU time of 2D model using the proposed framework is compared with the classical FEM solution. A 2d aluminum model like previous examples are used for demonstration. The waveform is not shown in this section for brevity.

The model is 0.1m by 0.1 m. The mesh size of the k-space model and FEM model are both 1e-3m. A 3.5 cycles tone-burst of 100khz is excited near the edge of the model. For accurate comparison, the FEM model and the k-space model are both coded in MATLAB. The CPU time of proposed framework is compared with the time using the FEM solver in MATLAB. The quantitative result is shown in Table 2. 5. It's seen that the proposed framework is about 19 times faster than the classical FEM solver. The superior efficiency the proposed framework will benefit the large-scale models in real-world engineering problems.

Table 2. 5 CPU time comparison

Method	CPU time(s)
k-space	5.5433
FEM	94.6291

2.9. Acknowledgement

The work is partially supported by NASA University Leadership Initiative (NNX17AJ86A; program officer: Dr. Kai Goebel). The support is greatly appreciated.

2.10. Appendix

The detailed derivation of Eq. 2-6 is discussed as below. An example is given to show the term in the bracket of Eq. 2-6 is the divergence of stress in Eq. A1. A Voigt Notation C_{jp} is used for stiffness matrix **C** in Eq. A1. The details of derivation of k-space operator and implementation on stress and velocity terms in x-direction is discussed here as shown in Eq. A2.

$$\rho(\frac{\partial^2 u_i}{\partial t^2}) = (\sigma_{ij,j}) + f_i$$

$$(div(\boldsymbol{\sigma}))_i = \sigma_{ij,j} = C_{ijkl} u_{k,lj} = [\nabla_{ij} C_{jp} \nabla_{pk}{}^T] u_k$$

$$\rho(\frac{\partial^2 u_i}{\partial t^2}) = M_i + f_i$$

$$M_i = [\nabla_{ij} C_{jp} \nabla^T{}_{pk}] u_k$$

$$\nabla = \begin{bmatrix} \frac{\delta}{\delta x_1} & 0 & 0 & 0 & \frac{\delta}{\delta x_3} & \frac{\delta}{\delta x_2} \\ 0 & \frac{\delta}{\delta x_3} & 0 & \frac{\delta}{\delta x_2} & 0 & \frac{\delta}{\delta x_1} \\ 0 & 0 & \frac{\delta}{\delta x_3} & \frac{\delta}{\delta x_2} & \frac{\delta}{\delta x_1} & 0 \end{bmatrix}$$

$$\begin{cases} M_1 = [\nabla_{ij} C_{jp} \nabla^T{}_{pk}] u_k \\ \quad = \nabla_{11} C_{11} \nabla^T{}_{11} u_1 + \nabla_{12} C_{21} \nabla^T{}_{11} u_1 + \nabla_{13} C_{31} \nabla^T{}_{11} u_1 + \ldots + \nabla_{16} C_{61} \nabla^T{}_{11} u_1 \\ \quad + \nabla_{11} C_{12} \nabla^T{}_{21} u_1 + \nabla_{11} C_{13} \nabla^T{}_{31} u_1 + \ldots + \nabla_{11} C_{16} \nabla^T{}_{61} u_1 + \ldots \\ \quad \ldots + \nabla_{16} C_{66} \nabla^T{}_{63} u_3 \\ \quad = \sum_{j=1,p=1,k=1}^{j=6,p=6,k=3} \nabla_{ij} C_{jp} \nabla^T{}_{pk} u_k \\ M_2 = \sum_{j=1,p=1,k=1}^{j=6,p=6,k=3} \nabla_{2j} C_{jp} \nabla^T{}_{pk} u_k \\ M_3 = \sum_{j=1,p=1,k=1}^{j=6,p=6,k=3} \nabla_{3j} C_{jp} \nabla^T{}_{pk} u_k \end{cases} \tag{A1}$$

$$\begin{cases} as \\ div(\boldsymbol{\sigma})_1 = \frac{\delta \sigma_{11}}{\delta x_1} + \frac{\delta \sigma_{12}}{\delta x_2} + \frac{\delta \sigma_{13}}{\delta x_3} \\ = \frac{\delta (C_{11} u_{1,1} + C_{12} u_{2,2} + C_{13} u_{3,3} + C_{14} u_{2,3} + C_{15} u_{1,3} + C_{16} u_{1,2})}{\delta x_1} + \ldots \\ + \frac{\delta (C_{66} u_{1,2} + C_{66} u_{2,1})}{\delta x_2} + \ldots \\ + \frac{\delta (C_{55} u_{1,3} + C_{55} u_{1,3})}{\delta x_3} \end{cases}$$

$$\Rightarrow M_1 = div(\boldsymbol{\sigma})_1$$

$$\begin{cases} \rho \dfrac{\delta v_1}{\delta t} = S_1 + f_1 \\ \dfrac{\partial \sigma_{11,1}}{\partial t} = C_{11kl}(\nabla v)_{k,l}, k = 1,2,3, l = 1,2,3 \end{cases}$$

where

$$S_1 = \sigma_{11,1} + \sigma_{12,2} + \sigma_{13,3}$$

$$\nabla(v)_{11} = F^{-1}(jk_1V_1)), \text{where}$$

$$V_1 = F(F^{-1}(Q_{1l}K_{lk}Q_{kn}{}^T F(v_n))), \text{where}$$

$$\begin{cases} V_1 = F(F^{-1}(Q_{11}K_{11}Q_{11}{}^T F(v_1) + Q_{11}K_{11}Q_{12}{}^T F(v_2) + Q_{11}K_{11}Q_{13}{}^T F(v_3))) + \ldots \\ \quad F(F^{-1}(Q_{12}K_{22}Q_{21}{}^T F(v_1) + Q_{12}K_{22}Q_{22}{}^T F(v_2) + Q_{12}K_{22}Q_{23}{}^T F(v_3))) + \ldots \\ \quad F(F^{-1}(Q_{13}K_{33}Q_{31}{}^T F(v_1) + Q_{13}K_{33}Q_{32}{}^T F(v_2) + Q_{13}K_{33}Q_{33}{}^T F(v_3))) \end{cases}$$

$$\begin{cases} \nabla(v)_{1,2} = F^{-1}(jk_2V_1)), \\ \nabla(v)_{1,3} = F^{-1}(jk_3V_1)), \\ \nabla(v)_{2,1} = F^{-1}(jk_1V_2)), \\ \nabla(v)_{2,2} = F^{-1}(jk_2V_2)), \end{cases}$$

$$\begin{cases} V_2 = F(F^{-1}(Q_{2l}K_{lk}Q_{kn}{}^T F(v_n))) \\ \quad = F(F^{-1}(Q_{21}K_{11}Q_{11}{}^T F(v_1) + Q_{21}K_{11}Q_{12}{}^T F(v_2) + Q_{21}K_{11}Q_{13}{}^T F(v_3))) + \ldots \\ \quad F(F^{-1}(Q_{22}K_{22}Q_{21}{}^T F(v_1) + Q_{22}K_{22}Q_{22}{}^T F(v_2) + Q_{22}K_{22}Q_{23}{}^T F(v_3))) + \ldots \\ \quad F(F^{-1}(Q_{23}K_{33}Q_{31}{}^T F(v_1) + Q_{23}K_{33}Q_{32}{}^T F(v_2) + Q_{23}K_{33}Q_{33}{}^T F(v_3))) \end{cases} \quad \text{(A2)}$$

$$\nabla(v)_{31} = F^{-1}(jk_1V_3)),$$

$$\begin{cases} V_3 = F(F^{-1}(Q_{3l}K_{lk}Q_{kn}{}^T F(v_n))) \\ \quad = F(F^{-1}(Q_{31}K_{11}Q_{11}{}^T F(v_1) + Q_{31}K_{11}Q_{12}{}^T F(v_2) + Q_{31}K_{11}Q_{13}{}^T F(v_3))) + \ldots \\ \quad F(F^{-1}(Q_{32}K_{22}Q_{21}{}^T F(v_1) + Q_{32}K_{22}Q_{22}{}^T F(v_2) + Q_{32}K_{22}Q_{23}{}^T F(v_3))) + \ldots \\ \quad F(F^{-1}(Q_{33}K_{33}Q_{31}{}^T F(v_1) + Q_{33}K_{33}Q_{32}{}^T F(v_2) + Q_{33}K_{33}Q_{33}{}^T F(v_3))) \end{cases}$$

$$S_1 = F^{-1}(jk_1\theta_{11}) + F^{-1}(jk_2\theta_{21}) + F^{-1}(jk_3\theta_{31})$$

$$\theta_{11} = F^{-1}(jk_1F(F^{-1}(Q_{nl}K_{lk}Q_{k1}{}^T F(\sigma_{1n}))))$$

$$\begin{cases} \theta_{11} = F^{-1}(jk_1F(F^{-1}(Q_{11}K_{11}Q_{11}{}^T F(\sigma_{11}) + Q_{12}K_{22}Q_{21}{}^T F(\sigma_{11}) + Q_{13}K_{33}Q_{31}{}^T F(\sigma_{11}) + \ldots \\ \quad Q_{21}K_{11}Q_{11}{}^T F(\sigma_{12}) + Q_{22}K_{22}Q_{21}{}^T F(\sigma_{12}) + Q_{23}K_{33}Q_{31}{}^T F(\sigma_{12}) + Q_{31}K_{11}Q_{11}{}^T F(\sigma_{13}) + \ldots \\ \quad Q_{32}K_{22}Q_{21}{}^T F(\sigma_{13}) + Q_{33}K_{33}Q_{31}{}^T F(\sigma_{13})))) \end{cases}$$

$$\begin{cases} \theta_{21} = F^{-1}(jk_2F(F^{-1}(Q_{11}K_{11}Q_{11}{}^T F(\sigma_{21}) + Q_{12}K_{22}Q_{21}{}^T F(\sigma_{21}) + Q_{13}K_{33}Q_{31}{}^T F(\sigma_{21}) + \ldots \\ \quad Q_{21}K_{11}Q_{11}{}^T F(\sigma_{22}) + Q_{22}K_{22}Q_{21}{}^T F(\sigma_{22}) + Q_{23}K_{33}Q_{31}{}^T F(\sigma_{22}) + Q_{31}K_{11}Q_{11}{}^T F(\sigma_{23}) + \ldots \\ \quad Q_{32}K_{22}Q_{21}{}^T F(\sigma_{23}) + Q_{33}K_{33}Q_{31}{}^T F(\sigma_{23})))) \end{cases}$$

$$\begin{cases} \theta_{31} = F^{-1}(jk_3F(F^{-1}(Q_{11}K_{11}Q_{11}{}^T F(\sigma_{31}) + Q_{12}K_{22}Q_{21}{}^T F(\sigma_{31}) + Q_{13}K_{33}Q_{31}{}^T F(\sigma_{31}) + \ldots \\ \quad Q_{21}K_{11}Q_{11}{}^T F(\sigma_{32}) + Q_{22}K_{22}Q_{21}{}^T F(\sigma_{32}) + Q_{23}K_{33}Q_{31}{}^T F(\sigma_{32}) + Q_{31}K_{11}Q_{11}{}^T F(\sigma_{33}) + \ldots \\ \quad Q_{32}K_{22}Q_{21}{}^T F(\sigma_{33}) + Q_{33}K_{33}Q_{31}{}^T F(\sigma_{33})))) \end{cases}$$

3. TOMOGRAPHIC DAMAGE IMAGING BASED ON INVERSE ACOUSTIC WAVE PROPAGATION IN K-SPACE USING ADJOINT METHOD

3.1. Abstract

A novel damage imaging of engineering structures and materials methodology using the inverse wave propagation in k-space with adjoint method is proposed in this paper. The proposed methodology consists of two parts: the wave propagation solution algorithms for elastic solids in k-space and adjoint method-based optimization algorithms for damage imaging. One major advantage of the proposed method is the superior computational efficiency compared to the classical finite element method-based wave propagation and gradient-based optimization algorithms. The k-space formulation for wave propagation in 2D and 3D solids are discussed first. Adjoint method and a modified conjugate gradient method is presented for the inverse problem of damage imaging. Following this, parametric studies for measurement duration, number of sensors, noise effect, and computational efficiency are discussed in detail. Next, demonstration examples for concrete structures with and without reinforcement are presented. Several conclusions and future work are given based on the proposed study.

Key words: k-space, adjoint, damage detection, imaging, tomography

3.2. Introduction

Aging-related damage and failure in structures, such as fatigue cracking, corrosion, and delamination, are critical for structural integrity and early detection of damage is beneficial for prognosis and risk management of aging infrastructure system. In addition, most engineering structures have embedded defects such as voids, cracks, inclusions, etc.

from manufacturing. The properties and locations of embedded defects are generally unknown and hard to detect in complex engineering structures. Quality control and anomaly detection is important for the risk assessment of structures under external loadings.

Non-destructive testing (NDT) and/or structural health monitoring (SHM) are widely used for this purpose. Different types of NDT techniques have been proposed for the damage detection, such as ultrasound, thermography, eddy current, microwave, and others[62][63]. The focus in this study is on the acoustic/ultrasound wave-based detection and only the related previous studies are briefly discussed below. Acoustic wave-based damage detection can be grouped into two major categories: feature-based damage detection and model-assisted damage detection. For feature-based damage detection, features from signals (e.g., amplitude, phase change, time of arrival, correlation) are extracted and used as indicators of damage. In this approach, the acoustic wave propagation model is not directly used for damage identification. For example, a SHM(structural health monitoring) technique based on novelty detection for damage detection on aircraft panel was discussed in [64]. A comparative study on NDE techniques on concrete structures including the shear wave ultrasound technique, ground penetrating radar, semi-coupled ultrasonic tomography were discussed in [65]. The techniques mentioned above can detect defects in thick, heavy concrete structures. Other techniques such as PCA (principle component analysis), PLS(partial least square) were discussed in [66]. A combined feature regression using signal magnitude, phase change, and correlation coefficient has been proposed for fatigue damage detection using piezo sensor network-induced Lamb waves[13][67]. Other methods, such as the neural

network, was also implemented for damage detection purpose using selected acoustic wave features [10]. Neural network-based method has wide applications in engineering structures. The highlight is that the method is not sensitive to the model information. However, the drawback is the time requirement on training the dataset. The efficiency highly depends on the learning rate in data-driven methods [14].The above techniques are used to reduce dimensions in damage detection problems and have been proven to be very efficient. The general steps of the method are that features are obtained from measured data. Regression or machine learning algorithms are applied to represent the relationship between selected features and damage sizes and/or locations.

For model-assisted damage detection, acoustic wave propagation model is directly used for identification or imaging of damage. This usually involves the inverse wave propagation solution for imaging. Such problems are consisting of model parameter estimation and damage identification. Most inverse wave propagation problems can be treated as an optimization problem where the objective is to minimize deviation of simulated sensor responses from the measured responses. Some well-developed methodologies based on optimization are briefly reviewed here. A finite element model updating method (FEMU) and virtual field method(VFM) based on full-field measurements were discussed for damage detection problem[16]. FEMU and VFM need information of full-field measurements to compute deviation between measurements and numerical estimation. Both methods show good accuracy and work for model of complex geometry. The drawbacks are such method can be computationally prohibitive when solving large-scale structures. They are also noise-sensitive due to the uncertainties in measurement as mentioned in 11. Levenburg-Marquart based method coupled with finite

element(FEM) was proposed for material parameter estimation purpose[17]. The computation on the Jacobian matrix is required due to the nature of Levenburg method. Therefore, this method is also computationally expensive for the large-scale model. Similarly, a trust-region algorithm coupled with FEM modeling was proposed for damage identification in reinforced concrete [18]. The wide use of FEM for inverse wave propagation is due to its maturity in solving the acoustic problems. Damage detection usually requires the finer mesh for the high frequency acoustic waves and is not computationally efficient for large 3D structures. A time reversal technique using the k-space wave propagation was applied on photoacoustic tomography in soft biological medium[69]. The demonstrated computational efficiency in the imaging reconstruction is due to the spectral nature of the k-space formulation and has a great potential for solid structures in engineering applications.

Both damage detection approaches have their own pros and cons. Feature-based damage detection is usually very fast and does not involves the inverse wave propagation solution. The key idea is the dimension reduction of signals to achieve the efficient damage detection. The disadvantage is that the loss of information due to the feature extraction can induce significant uncertainties for the damage detection and reduces the resolution. The resolution of the feature-based approach highly depends on the sensing path density (e.g., number of sensors permanently installed or the probe scanning steps). Model-assisted damage detection is on the opposite side. The damage detection is usually slow due to the requirement for the inverse wave propagation solution, which is especially true for the large 3D structures. The benefits for model-assisted damage

detection is the ability for high resolution imaging with limited number of sensing paths since the entire signal histories are used for damage identification.

Based on the above brief review, the motivation of the proposed study is to develop very efficient damage imaging technique for 2D and 3D structures using model-assisted approach. The special focus is on the efficiency of the imaging algorithm as it is the major bottleneck of the model-assisted approach. The computational efficiency is achieved by two complimentary components. First, a fast forward wave propagation solver is needed. A k-space (wavenumber-space) approach [19] is proposed for the damage imaging. Classical finite element-based solver is not appropriate for small damage detection due to the fine mesh requirement for the high frequency signals. Most model-based inverse methods mentioned in 10–13,16 are based on FEM method. Compared to classical FEM method, the implementation of k-space method in the proposed framework highly speeds up the simulation efficiency and saves computational memory [20]. Next, efficient inverse wave propagation algorithms is proposed. Classical gradient-based optimization algorithms usually requires finite difference method for gradient calculation, which is prohibitively expensive for large degree of freedoms (e.g., damage imaging in 3D structures) [71]. Adjoint method-based optimization algorithms is proposed, which avoids the repetitive finite difference calculations for every imaging variables. Thus, superior computational efficiency can be achieved by combining these two methods together for the damage imaging.

Some advantages and uniqueness of the proposed framework are: 1.compared to feature- based approach as mentioned in [14], the proposed framework relaxes the requirements on measurements and time spent on training data; 2. In the VFM and

FEMU method, full-field measurements are required [68]. The proposed framework only needs limited measurements to reconstruct the damage. Therefore, the efficiency of damage reconstruction is highly improved. 3. The forward problems is based on coupled first-order equations, which is easy to solve in mathematical view [21]. 4. Compared to the most applications on soft and homogeneous materials using the k-space method, the focus is on materials with strong discontinuity widely seen in engineering structures. The adjoint method is combined with the k-space method for damage detection purpose. The formulation based on this application is given. 5. Sensitivity equations commonly seen in inverse problems are also solved using the k-space method to improve the computational efficiency.

The paper is organized as follows. First, the formulation of the damage imaging using the proposed methodology is proposed. Forward wave propagation in k-space is briefly reviewed. Adjoint-based inverse formulation is discussed in detail and the optimization algorithms and flow chart are presented. Following this, engineering representative examples are used to illustrate the proposed methodology. The reconstruction of defects and rebar in a reinforced concrete structure is studied using the structural information shown in [65]. The superior efficiency of the proposed framework is verified by comparing with the FEM-based model. As mentioned above, the stability and accuracy of inverse problem are related to factors such as the number of measurements, simulation duration, and measurement noise [72]. Therefore, a parametric study on measurement noise, duration, and the number of measurements is discussed in detail.

3.3. Damage Imaging Based on Forward And Inverse Wave Propagation

This section discussed the proposed methodology in detail. A brief review of the forward wave propagation solver using the k-space formulation is given first for the completeness of the proposed study. Detailed derivation and verification can be found in [19]. Following this, the formulation of the damage imaging and solution algorithm is discussed in detail.

3.3.1. K-Space Method for Forward Wave Propagation Analysis In Damaged Solids

Model-assisted approach for damage detection require a forward solver to obtain the system output under external excitations. The proposed study will use the k-space method as the forward solver due to its superior efficiency. The k-space method is based on the Pseudo-Spectral method with improved stability and accuracy by introducing the k-space operator based on spatial Fourier Transform. The use of k-space operator relax the requirement on time step and comparable accuracy is achieved even when a larger time step is used [33]. The other advantage of k-space method is the high efficiency due to the nature of Fourier series. The Fourier- based functions can be represented by sinusoidal functions and a sinusoidal function can be well represented by at least two points sampled per wavelength according to Nyquist-Shannon sampling theorem[73]. Classical finite element and finite difference methods require 15-20 points sampled per wavelength. Therefore, the k-space method has superior computational efficiency for large scale structural applications.

Most recent advances of the k-space method are biomedical applications on soft materials [33] [38] and isotropic materials[37]. The application of k-space method focuses on the strong discontinuity or damage widely seen in structural materials in this paper.

The k-space method is based on a stress-velocity formulation as shown in Eq. (3.3.1) and (3.3.2), where $\boldsymbol{v}$ is the component of particle velocity, $\boldsymbol{\sigma}$ is second-order Cauchy stress tensor and $\boldsymbol{C}$ is a fourth-order stiffness tensor,

$$\rho \frac{\partial \boldsymbol{v}}{\partial t} = \frac{\partial \boldsymbol{\sigma}}{\partial \boldsymbol{x}} + \boldsymbol{f} \tag{3.3.2}$$

$$\frac{\partial \boldsymbol{\sigma}}{\partial t} = \frac{\boldsymbol{C}}{2}(\nabla \boldsymbol{v} + \nabla \boldsymbol{v}^{\boldsymbol{T}}) \tag{3.3.3}$$

The above equations are solved numerically in a k-t (wavenumber-time) domain. A k-space operator $\boldsymbol{\nabla_k}$ is derived for the computation of spatial derivative based on Fourier Transform pair[19],

$$\boldsymbol{\nabla}_k(\boldsymbol{v}) = F^{-1}\{k\boldsymbol{Q}\boldsymbol{K}\boldsymbol{Q}^T F(\boldsymbol{v})\} \tag{3.3.4}$$

where k is the wavenumber, and **Q** is the matrix with each column being the eigenvector of Christoffel matrix **T**. **T** is a positive definite matrix, which can be written in a eigen-decomposition form, $\mathbf{T}=\mathbf{Q}\boldsymbol{\alpha}\mathbf{Q}^{\mathrm{T}}$ as discussed in [48]. The matrix **K** is diagonal matrix and $K_{ij}=j\delta_{ij}\mathrm{sinc}(b_i\Delta t/2)$, where b_i is square root value of the eigenvalue $\boldsymbol{\alpha}$. F and F^{-1} is the spatial transform pair. The time derivative in Eq. (3.3.1) and (3.3.2) are iteratively solved using a first-order Finite Difference scheme, i.e., Eq. (3.3.1) and (3.3.2) can be written in discretized form,

$$\rho \frac{\boldsymbol{v}(t+\mathbf{1}) - \boldsymbol{v}(t)}{\Delta t} = \boldsymbol{\nabla}_k(\boldsymbol{\sigma}(t)) + \boldsymbol{f}(t) \tag{3.3.5}$$

$$\frac{\boldsymbol{\sigma}(t+1) - \boldsymbol{\sigma}(t)}{\Delta t} = \frac{\boldsymbol{C}}{2}(\boldsymbol{\nabla}_k \boldsymbol{v}(t+1) + \boldsymbol{\nabla}_k \boldsymbol{v}(t+1)^{\boldsymbol{T}}) \tag{3.3.6}$$

where *t* is the current time step, and the spatial derivative of stress and velocity are obtained using Eq. (3.3.3). The displacement can be easily obtained by integrating velocity in time domain. In Section 3.3.2, displacement is used as the variable in the inverse computation.

The steps of k-space method are concluded in the figure below. The numerical verification of the accuracy and efficiency of k-space method for 2D and 3D problems can be found in [19].

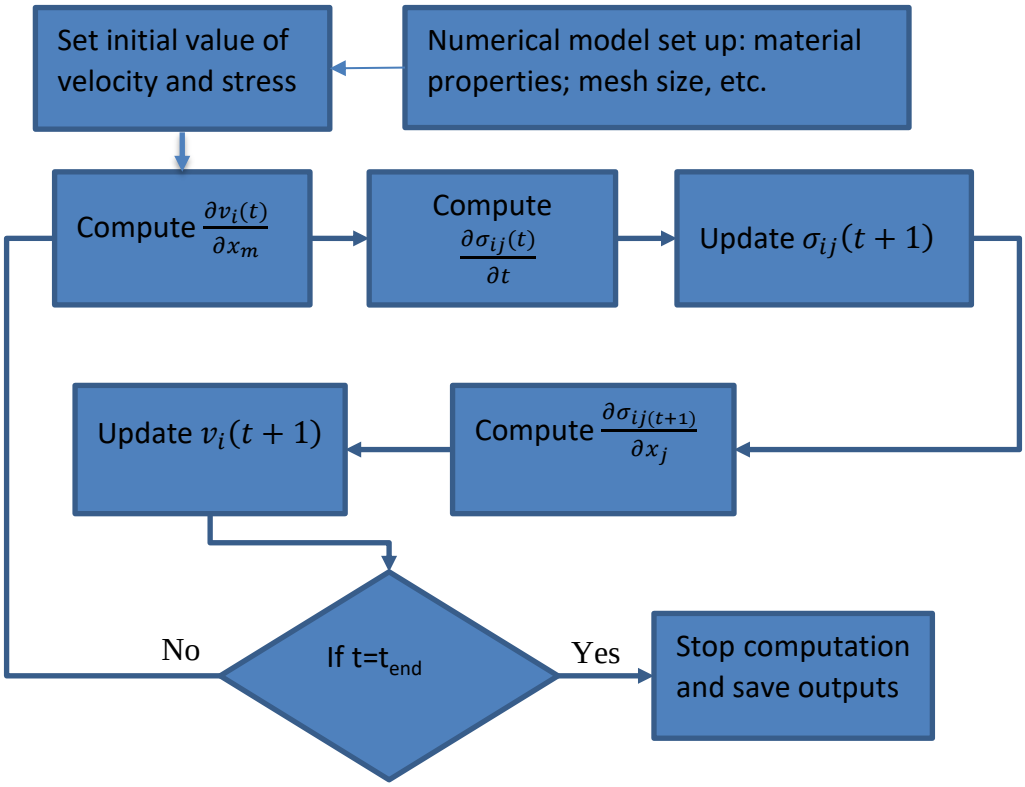

Figure 3. 1 Flowchart Diagram of the k-space method solving forward problem

3.3.2. Damage Imaging Formulation and Solution Algorithms

The main objective of this section is to provide the problem statement and formulation of the damage imaging framework. The formulation of the damage imaging is treated as a constrained optimization problem to inversely identify the material property at each grid point in the simulation domain. The objective function is the summation of the squared error of model predicted displacements and measured displacements as,

$$\min \{S(P)|S(P) = \frac{1}{2}\int_0^T \int_V \sum_{m=1}^{M} \left(u(x_m, t; P) - U_m(x,t)\right)^2 dV dt\} \qquad (3.3.7)$$

where the objective S is written as a function of measured displacement U_m and predicted displacement u. *P* is the unknown parameter to be estimated. *T* is the duration of the measurement, *M* is the total number of sensors, and *V* is the domain of interest. The predicted displacement *u* is obtained by solving the wave propagation equations using the k-space method.

In the proposed study, the objective function is optimized using the constrained CG method with the adjoint method. Classical methods of gradient computation such as finite difference and central difference methods are time-consuming and computationally expensive in a large-scale model. The implementation of adjoint method helps to reduce the computation cost on gradient by introducing a Lagrange multiplier. The adjoint method are widely used to solve inverse heat transfer problem and elastography in medical imaging, source reconstruction in seismology [74]-[75]. A sensitivity problem is discussed first below since the solution is used for the computation of the step size in the CG method. In the following discussion, material stiffness (shear modulus) is used for the parameter P. Other material properties, such as density and attenuation coefficient,

can be used as the parameter P in the similar way. In the sensitivity problem, the variational form of the displacement and model parameter is used. The displacement u becomes (u+Δu) by adding a perturbation Δu and the stiffness tensor C becomes (C+ΔC) along the direction of estimated variable *P*. The displacement variation $\Delta \boldsymbol{u}$ is a function of space coordinate *x*, time *t* , and model parameter variation $\Delta \boldsymbol{P}$, i.e., $\Delta \boldsymbol{u} = \Delta \boldsymbol{u}(\boldsymbol{x}, \boldsymbol{t}; \Delta \boldsymbol{P})$. The variation in force and density are canceled out since they are assumed to be independent of $\boldsymbol{P}$. By using the Taylor expansion, the sensitivity equation can be expressed as

$$\rho \frac{\partial^2 \Delta \boldsymbol{u}}{\partial^2 t} = \nabla \cdot (\Delta \boldsymbol{C} : \nabla \boldsymbol{u} + \boldsymbol{C} : \nabla(\Delta \boldsymbol{u})) \tag{3.3.8}$$

The initial conditions and boundary conditions of the sensitivity problem are,

$$\Delta \boldsymbol{u}(x, 0) = 0, \frac{\partial \Delta \boldsymbol{u}(x, 0)}{\partial t} = 0 \tag{3.3.9}$$

$$\boldsymbol{n} \cdot \Delta \boldsymbol{\sigma} = 0 \; or \; \boldsymbol{n} \cdot (\Delta \boldsymbol{C} : \nabla \boldsymbol{u} + \boldsymbol{C} : \nabla(\Delta \boldsymbol{u})) = 0 \tag{3.3.10}$$

The form of Eq.0.5 is analogous to the wave equation where the variable is Δu instead of u and the force is $\nabla \cdot (\Delta \boldsymbol{C} : \nabla \boldsymbol{u})$ instead of $\boldsymbol{f}$. Therefore, the solution to sensitivity problem can be obtained by the k-space method when the unknown variable is Δu and external force term is $\nabla \cdot (\Delta \boldsymbol{C} : \nabla \boldsymbol{u})$. Following the sensitivity problem discussion, the adjoint problem is discussed below. Based on the chain rule, gradient of the objective function S is computed as

$$\Delta S(\boldsymbol{P}) = \text{grad} S(\boldsymbol{P}) \Delta \boldsymbol{P} \tag{3.3.11}$$

Therefore, the variation ΔS along the direction of estimated variable $\boldsymbol{P}$ can be computed first and the gradient grad$\boldsymbol{S(P)}$ is derived based on it. Before computing the gradient, the objective function need to be modified by introducing a Lagrange multiplier λ (x, t),

$$\begin{aligned} S(\boldsymbol{P}) = \frac{1}{2}\int_0^T \sum_{m=1}^{M} \int_V \left(\boldsymbol{u}(\boldsymbol{x},t;\boldsymbol{P}) - \boldsymbol{U_m}(\boldsymbol{x},t)\right)^2 \delta(\boldsymbol{x}-\boldsymbol{x_m}) dt\, dV dt \\ - \int_0^T \int_V \boldsymbol{\lambda}(\boldsymbol{x},t)\left(\rho \frac{\partial^2 \boldsymbol{u}(\boldsymbol{x},t;\boldsymbol{P})}{\partial^2 t} - \nabla\cdot(\boldsymbol{C}:\nabla(\boldsymbol{u}(\boldsymbol{x},t;\boldsymbol{P}))) - \boldsymbol{f}\right) dV dt \end{aligned} \tag{3.3.12}$$

where δ is a Dirac function, and the number of sensor *m=1…M.* The variation ΔS is found to be,

$$\begin{aligned} \Delta S(\boldsymbol{P}) = \int_0^T \sum_{m=1}^{M} \int_V (\boldsymbol{u}-\boldsymbol{U_m})\delta(\boldsymbol{x}-\boldsymbol{x_m})\Delta\boldsymbol{u} dV dt \\ - \int_0^T \int_V \rho\boldsymbol{\lambda}\frac{\partial^2 \Delta\boldsymbol{u}}{\partial^2 t} dV dt \\ + \int_0^T \int_V \boldsymbol{\lambda}\nabla\cdot\left(\Delta\boldsymbol{C}:\nabla(\boldsymbol{u}) + \boldsymbol{C}:\nabla(\Delta\boldsymbol{u})\right) dV dt \end{aligned} \tag{3.3.13}$$

The second step is to simplify the variation on objective. The first term on the right-hand side in Eq. (3.3.16) is straightforward and there is no need to simplify. The second term can be expanded by integral by parts,

$$\begin{aligned} \int_0^T \int_V \rho\boldsymbol{\lambda}\frac{\partial^2 \Delta\boldsymbol{u}}{\partial^2 t} dV dt &= \int_V \rho\boldsymbol{\lambda}\frac{\partial \Delta\boldsymbol{u}}{\partial t} dV\Big|_0^T - \int_0^T \int_V \rho\frac{\partial\boldsymbol{\lambda}}{\partial t}\frac{\partial\Delta\boldsymbol{u}}{\partial t} dV dt \\ &= \int_V \rho\boldsymbol{\lambda}\frac{\partial \Delta\boldsymbol{u}}{\partial t} dV\Big|_0^T - \int_V \rho\frac{\partial\boldsymbol{\lambda}}{\partial t}\frac{\partial\Delta\boldsymbol{u}}{\partial t} dV\Big|_0^T \\ &\quad + \int_0^T \int_V \rho\frac{\partial^2\boldsymbol{\lambda}}{\partial^2 t}\Delta\boldsymbol{u} dV dt \end{aligned} \tag{3.3.14}$$

If the Gauss' theorem is applied to the last term of Eq.(3.3.16), it's found that,

$$\int_0^T \int_V \boldsymbol{\lambda}\nabla \cdot \left(\Delta \boldsymbol{C}\colon \nabla(\boldsymbol{u}) + \boldsymbol{C}\colon \nabla(\Delta \boldsymbol{u})\right) dV dt$$

$$= \int_0^T \int_S \boldsymbol{\lambda} \cdot (\mathbf{n} \cdot \left(\Delta \boldsymbol{C}\colon \nabla(\boldsymbol{u}) + \Delta \boldsymbol{C}\colon \nabla(\boldsymbol{u})\right)) dS dt \tag{3.3.15}$$

$$- \int_0^T \int_V \nabla\boldsymbol{\lambda}\colon \left(\Delta \boldsymbol{C}\colon \nabla(\boldsymbol{u})\right) dV dt$$

By applying the Gauss' Theorem again to the last term in Eq.(3.3.15), it can be further simplified if the commutativity of double dot product is applied[76],

$$-\int_0^T \int_V \nabla\boldsymbol{\lambda}\colon \left(\boldsymbol{C}\colon \nabla(\Delta \boldsymbol{u})\right) dV dt = -\int_0^T \int_V \Delta\mathbf{u}\colon (\boldsymbol{C}\colon \nabla\boldsymbol{\lambda}) dV dt$$

$$= -\int_0^T \int_S \Delta\mathbf{u} \cdot \left(\boldsymbol{n} \cdot (\boldsymbol{C}\colon \nabla\boldsymbol{\lambda})\right) dS dt \tag{3.3.16}$$

$$+ \int_0^T \int_V \Delta\mathbf{u} \cdot (\nabla \cdot (\boldsymbol{C}\colon \nabla\boldsymbol{\lambda})) dV dt$$

Based on the results in Eq.(3.3.17)-(3.3.19), the variation ΔS is,

$$\Delta S(\boldsymbol{P}) = \int_0^T \sum_{m=1}^{M} \int_V (\boldsymbol{u} - \boldsymbol{U_m})\delta(\boldsymbol{x} - \boldsymbol{x_m})\Delta \boldsymbol{u} dV\, dt - \int_V \rho \boldsymbol{\lambda} \frac{\partial \Delta \boldsymbol{u}}{\partial t} dV|_0^T$$

$$+ \int_V \rho \frac{\partial \boldsymbol{\lambda}}{\partial t} \frac{\partial \Delta \boldsymbol{u}}{\partial t} dV|_0^T - \int_0^T \int_V \rho \frac{\partial^2 \boldsymbol{\lambda}}{\partial^2 t} \Delta \boldsymbol{u} dV dt$$

$$+ \int_0^T \int_S \boldsymbol{\lambda} \cdot (\mathbf{n} \cdot \left(\Delta \boldsymbol{C} : \nabla(\boldsymbol{u}) + \boldsymbol{C} : \nabla(\Delta \boldsymbol{u})\right)) dS dt \tag{3.3.17}$$

$$- \int_0^T \int_V \nabla \boldsymbol{\lambda} : \left(\Delta \boldsymbol{C} : \nabla(\mathrm{u})\right) dV dt$$

$$- \int_0^T \int_S \Delta \mathbf{u} \cdot \left(\boldsymbol{n} \cdot (\boldsymbol{C} : \nabla \boldsymbol{\lambda})\right) dS dt$$

$$+ \int_0^T \int_V \Delta \mathbf{u} \cdot (\nabla \cdot (\boldsymbol{C} : \nabla \boldsymbol{\lambda})) dV dt$$

Based on Eq.(3.3.9) and Eq.(3.3.10), which are the boundary and initial conditions in the sensitivity problem, the terms involving $\frac{\partial \Delta \boldsymbol{u}(\boldsymbol{x},\mathbf{0})}{\partial t}$ and the term containing $\mathbf{n} \cdot \left(\Delta \boldsymbol{C} : \nabla(\boldsymbol{u}) + \boldsymbol{C} : \nabla(\Delta \boldsymbol{u})\right)$=0 can be canceled. Therefore, Eq.(3.3.17) can be expressed as,

$$\Delta S(\boldsymbol{P}) = \int_0^T \sum_{m=1}^{M} \int_V (\boldsymbol{u} - \boldsymbol{U_m})\delta(\boldsymbol{x} - \boldsymbol{x_m})\Delta \boldsymbol{u} dV dt$$

$$- \int_0^T \int_V \rho \frac{\partial^2 \boldsymbol{\lambda}}{\partial^2 t} \Delta \boldsymbol{u} dV dt$$

$$+ \int_0^T \int_V (\nabla \cdot (\boldsymbol{C}: \nabla(\Delta \boldsymbol{\lambda}))) \cdot \Delta \mathbf{u} dV dt - \int_V \rho \boldsymbol{\lambda} \frac{\partial \Delta \boldsymbol{u}}{\partial t} dV|_T \quad (3.3.18)$$

$$+ \int_V \rho \frac{\partial \boldsymbol{\lambda}}{\partial t} \frac{\partial \Delta \boldsymbol{u}}{\partial t} dV|_T - \int_0^T \int_V \nabla \boldsymbol{\lambda}: (\Delta \boldsymbol{C}: \nabla(\boldsymbol{u})) dV dt$$

$$- \int_0^T \int_S \Delta \mathbf{u} \cdot (\boldsymbol{n} \cdot (\boldsymbol{C}: \nabla \boldsymbol{\lambda})) dS dt$$

If terms related to Δu are canceled by assigning a proper value of λ in Eq. (3.3.18), the derivative of ΔS with respect to Δu is avoided in the computation, which is a time-consuming step in the optimization problem. Thus, one can obtain

$$-\rho \frac{\partial^2 \boldsymbol{\lambda}}{\partial^2 t} + \nabla \cdot (\boldsymbol{C}: \nabla \boldsymbol{\lambda}) + \sum_{m=1}^{M} (\boldsymbol{u} - \boldsymbol{U_m})\delta(\boldsymbol{x} - \boldsymbol{x_m}) = 0 \quad (3.3.19)$$

Eq. (3.3.19) is called the adjoint problem achieved by canceling Δu terms in Eq. (3.3.18). The final time conditions are satisfied, which are derived by making terms involving $\frac{\partial \Delta \boldsymbol{u}(\boldsymbol{x},\boldsymbol{T})}{\partial t}$ zero in Eq. (3.3.17),

$$\boldsymbol{\lambda}(\boldsymbol{x}, \boldsymbol{T}) = \mathbf{0}, \frac{\partial \boldsymbol{\lambda}}{\partial \boldsymbol{t}}(\boldsymbol{x}, \boldsymbol{T}) = \mathbf{0} \quad (3.3.20)$$

and the boundary condition of the adjoint problem is,

$$\boldsymbol{n} \cdot (\boldsymbol{C}: \nabla(\boldsymbol{\lambda})) = 0 \; or \; \boldsymbol{n} \cdot \boldsymbol{\sigma}' = 0 \quad (3.3.21)$$

One feasible solution to Eq.(3.3.19) is to define a new time variable t'=T-t. A new adjoint variable **λ**' is defined such that **λ**' (**x**, t') =**λ** (**x**, T-t). By substituting the new time variable t' and **λ**' into Eq.(3.3.19), one can obtain

$$-\rho\frac{\partial^2\boldsymbol{\lambda}'(\boldsymbol{x},t')}{\partial^2 t}+\nabla\cdot(\boldsymbol{C}:\nabla\boldsymbol{\lambda}'(\boldsymbol{x},\boldsymbol{t}'))+\sum_{m=1}^{M}(\boldsymbol{u}(T-t)-\boldsymbol{U_m}(T-t))\delta(\boldsymbol{x}-\boldsymbol{x_m})=0 \tag{3.3.22}$$

which is subject to the new initial condition,

$$\boldsymbol{\lambda}'(x,0)=0\,\frac{\partial\boldsymbol{\lambda}'}{\partial t}(x,0)=0, \tag{3.3.23}$$

The boundary condition is the same as Eq. (3.3.21). It's seen that the form of Eq.(3.3.22) is analogous to the wave equation by replacing displacement $\boldsymbol{u}$ by $\boldsymbol{\lambda}'$ and by replacing force $\boldsymbol{f}$ by the last term in Eq. (3.3.22). Therefore, the adjoint problem is also solved using the k-space method. The original adjoint variable λ can be easily obtained by replacing λ' by λ or set λ (x, t) =λ' (x, T-t'). The variation ΔS in Eq.(3.3.18) is simplified as,

$$\Delta S(\boldsymbol{P})=-\int_0^T\int_V\nabla\boldsymbol{\lambda}:\big(\Delta\boldsymbol{C}:\nabla(\boldsymbol{u})\big)dVdt \tag{3.3.24}$$

Since stiffness is considered as the unknown parameter $\boldsymbol{P}$, Eq. (3.3.24) can also be written as a function of ΔP,

$$\Delta S(\boldsymbol{P})=-\int_0^T\int_V\nabla\boldsymbol{\lambda}:\left(\frac{\partial\boldsymbol{C}}{\partial\boldsymbol{P}}:\nabla(\boldsymbol{u})\right)\Delta\boldsymbol{P}dVdt \tag{3.3.25}$$

By substituting Eq. (3.3.25) into Eq. (3.3.10), the gradient term $gradS(\boldsymbol{P})$ becomes,

$$\text{grad}S(\boldsymbol{P}) = -\int_0^T \int_V \nabla\boldsymbol{\lambda}\colon\left(\frac{\partial \boldsymbol{C}}{\partial \boldsymbol{P}}\colon\nabla\boldsymbol{u}\right) dV dt \tag{3.3.26}$$

Eq. (3.3.26) gives the gradient of the objective in terms of the adjoint variable. It is seen that the gradient solution does not dependent on the dimensionality (number of unknowns in the *P* vector), which greatly enhance the optimization efficiency.

Next, a Conjugate Gradient (CG) method combining the above-mentioned adjoint method is used for parameter estimation. The general formulation of iterative CG method was well-developed and discussed in many optimization problems [77] [78][79]. Only a brief overview is shown here for the completeness of the proposed study. Eq.(3.3.27)and (3.3.29) show the formulation of CG, where *i* is the number of iterations, and $\boldsymbol{P}$ is unknown parameter. The value of $\boldsymbol{P}$ is updated along searching direction $\boldsymbol{d}$ iteratively,

$$\boldsymbol{P}^{i+1} = \boldsymbol{P}^i + \beta^i \boldsymbol{d}^i \tag{3.3.27}$$

where β^i is searching step size. In classical CG, the step size β is a function of sensitivity matrix[72]. In the proposed framework, a line search technique is used to simplify the equation so that the step size is in term of $\Delta\boldsymbol{u}$ instead of the sensitivity term [80]. The expression is shown in Eq. (3.3.28),

$$\beta^i = \frac{\sum_{m=1}^{M}\int_0^T (\boldsymbol{U}^i{}_m - \boldsymbol{u}^i{}_m)\cdot\Delta\boldsymbol{u}^i{}_m dt}{\sum_{m=1}^{M}\int_0^T \Delta\boldsymbol{u}^i{}_m\cdot\Delta\boldsymbol{u}^i{}_m dt} \tag{3.3.28}$$

where Δu is obtained from the solution of the sensitivity problem, Eq. 0.5. The other important parameter in CG is the searching direction $\boldsymbol{d}$,

$$\boldsymbol{d}^i = -\nabla S\left(\boldsymbol{P}^i\right) + \gamma^i \boldsymbol{d}^{i-1} \tag{3.3.29}$$

where initial value $\boldsymbol{d}^0=-\nabla S(\boldsymbol{P}^0)$, γ is the conjugation coefficient and the expression is shown in Eq. (3.3.28) , which is in the form derived by *Polak* as mentioned in [11],[19].

$$\gamma^i = \frac{\nabla S(\boldsymbol{P}^i)^T(\nabla S(\boldsymbol{P}^i) - \nabla S(\boldsymbol{P}^{i-1}))}{\nabla S(\boldsymbol{P}^{i-1})^T \nabla S(\boldsymbol{P}^{i-1})} \tag{3.3.30}$$

where grad$S$ is obtained by Eq. (3.3.26) in terms of adjoint variable $\boldsymbol{\lambda}$.

The computation steps are summarized below,

Step 1. Compute the direct problem Eq. (3.3.1) and (3.3.2) given initial guess of unknown parameter $\boldsymbol{P}$.

Step 2. Compare the measurements $\boldsymbol{U_m}$ recorded by sensors with estimated displacement $\boldsymbol{u_m}$ by computing objective function Eq. (3.3.6).

Step 3. Set a proper stopping criterion based on the objective, i.e. a threshold ε that if $S(\boldsymbol{P})<\varepsilon$, stop the iterations; If not, go to Step 4,

Step 4. Solve sensitivity problem Eq. 0.5 save the solution $\Delta\boldsymbol{u}$,

Step 5. Solve adjoint problem Eq. (3.3.19) and save the solution $\boldsymbol{\lambda}$,

Step 6. Knowing $\boldsymbol{\lambda}$ and estimated $\boldsymbol{P}$, compute gradient grad$S(\boldsymbol{P})$ using Eq. (3.3.25),

Step 7. Compute conjugation coefficient γ^i using Eq. (3.3.30) and searching step size β^i using Eq. (3.3.28),

Step 8. Update $\boldsymbol{P}^i$ to $\boldsymbol{P}^{i+1}$ using Eq. (3.3.27),

Step 9. Let iteration number $i=i+1$ and start from Step 1 to Step 8 again.

3.4. Numerical Simulations and Demonstration Example

Numerical simulation using the proposed methodology is performed in this section. First, parametric studies are used to investigate several sensing parameters on the accuracy and efficiency of the proposed methodology, such as signal duration, number of sensors, and noise level. Next, the proposed methodology is applied to several homogeneous (aluminum plate and plain concrete block) and heterogeneous (reinforced concrete with steel liner) 3D structures for demonstration.

3.4.1. Parametric Study

An aluminum plate of 10cm by 10cm in 2d is modelled using the proposed methodology. Material properties are given in Table. 3-2. A total of 30 sensors is attached near edges of the plate as shown in Fig. 3-2. Damage of various shapes is defined inside the dashed square. Each sensor acts as actuator and receiver.

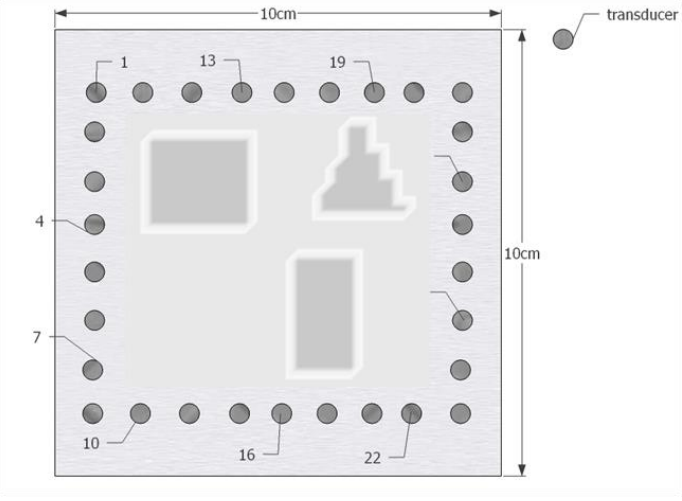

Figure 3. 2 Sensor layout and predefined damage field

The sensor has a certain duration of measurement that may affect the inverse imaging result. Therefore, the duration t_f of 30us, 50us, and 100us are used when the other parameters stay the same. The reconstructed modulus distribution when measurement duration is 30us, 50 us and 100 us, respectively are shown in Fig. 3-3. It is shown from images that the longer duration of signals will improve the imaging. A quantitative assessment is shown in Fig. 3-4 by plotting the cross-correlation coefficient of the reconstructed images with the true damage image with respect to the signal durations. It is seen that increasing the measurement duration increases the imaging performance drastically at the beginning and shows less effect when the measurement duration is beyond a certain limit (e.g., 40 *us*).

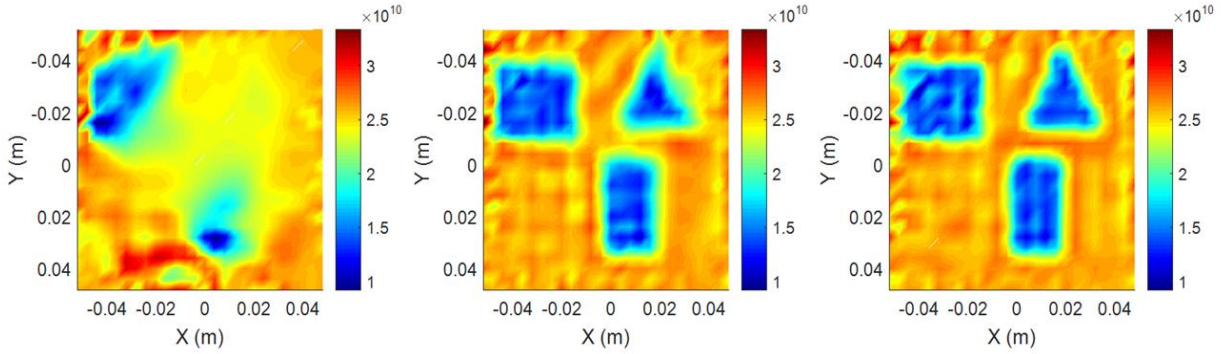

Figure 3. 3Reconstruction when measurement duration is (a) 30us; (b) 50us; (c) 100us.

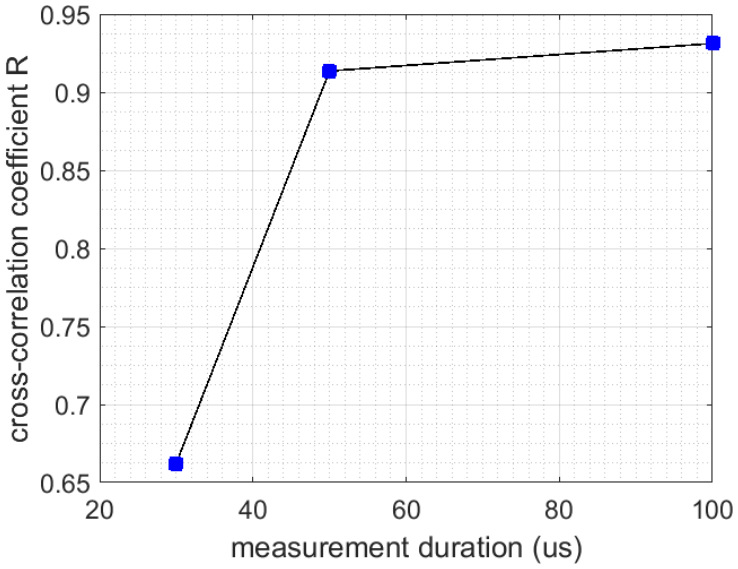

Figure 3. 4 Cross-correlation coefficient plot when t_f is 30us, 50us, and 100us.

Next, the effect of number of sensors on the reconstruction accuracy is discussed. Same model as the above one is used. The number of sensors is reduced to 24,17,9, 6, respectively and the corresponding result is compared with the one using 33 measurements. The duration of 100 us is used in both scenarios. It is seen that the increase of sensors will improve the imaging resolution, but it is not proportional to the number of sensors. For fewer number of sensors, the increase of sensors significantly improves the imaging quality. If the number of sensors is beyond a certain number (e.g., 24 in this case), the imaging is good enough to isolate the damage location and sizes. The cross-correlation coefficients with respect to the number of sensors is shown in Fig. 3-5(f) for this trend.

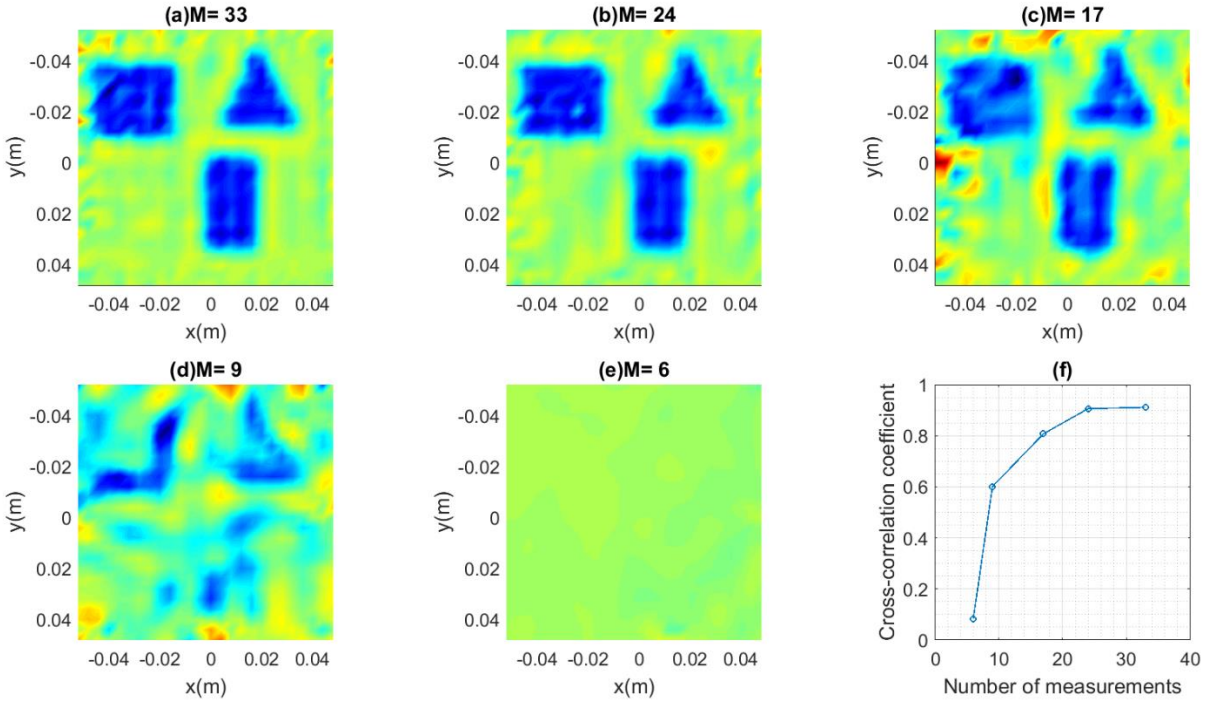

Figure 3. 5 Reconstruction result when (a) 33 measurements are taken; (b) 24 measurements are taken; (c) 17 measurements are taken; (d) 9 measurements are taken; (e) 6 measurements are taken;(f) cross-correlation coefficient between reconstruction result and predefined damage.

Following this, the effect of measurement noise is discussed. The Gaussian random noise of various standard deviation is added to the measurements to see the effect on the inverse result. The same model with duration of 100us and 30 sensors are used. Fig. 3-6 shows the mean value and the plus/minus standard deviation of reconstruction result when noise level of 0.01, 0.1, 0.2 is applied to measurements. In each scenario of certain noise, the Monte Carlo simulation technique is used for random sampling. The mean and variance of results of 50 Monte Carlo simulations are computed. The mean value has little variation when noise level is increased as shown in Fig. 3-6. The standard deviation increases as the noise level increases. Therefore, we conclude that the mean reconstruction result is not sensitive to the noise level range in the current investigation.

The mean damage imaging for different level of noise are shown in Fig. 3-7. The location and shape of damage are well reconstructed in all three scenarios.

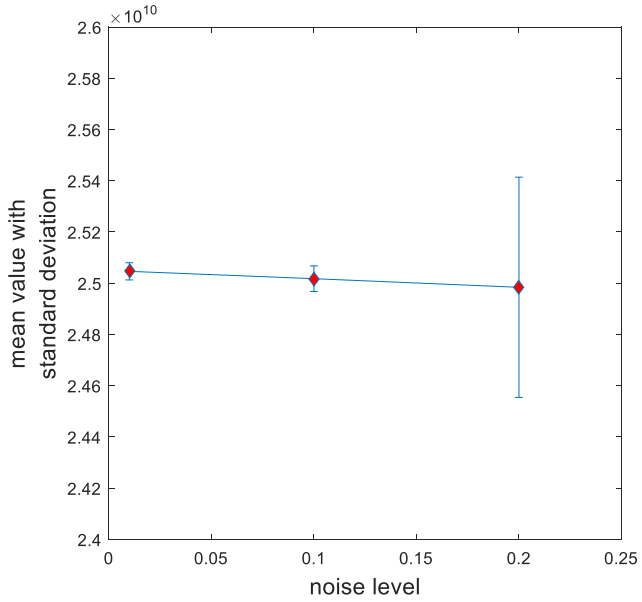

Figure 3. 6 Mean value with standard deviation of reconstruction result when noise level of 0.01,0.1,0.2 is added to measurements.

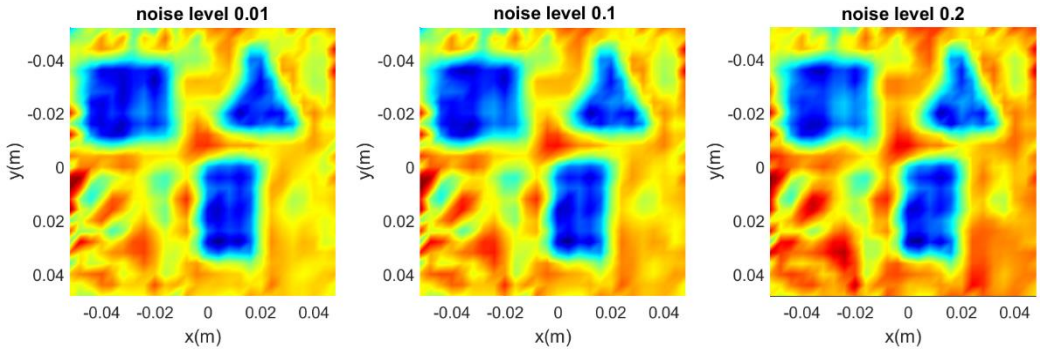

Figure 3. 7 Reconstruction result when level of 0.01,0.1,0.2 Gaussian random noise is added in measurements.

As mentioned in the previous sections, the implementation of k-space and adjoint method highly increases the computational efficiency. To quantify the superior efficiency, the CPU time of proposed framework is compared with the classical FEM solution with CG method under different iterations. The same 2d model is used. The model has 30 sensors

and 100us duration. In Fig. 3-8, the CPU time of proposed framework in different iterations is shown together with the CPU time using the FEM solver. From Fig. 3-8 and Table. 3-1, we can conclude that the proposed framework has superior efficiency compared to classical inverse solver. It should be mentioned that the 3D case will have even higher computational efficiency due to the large number of degree of freedoms.

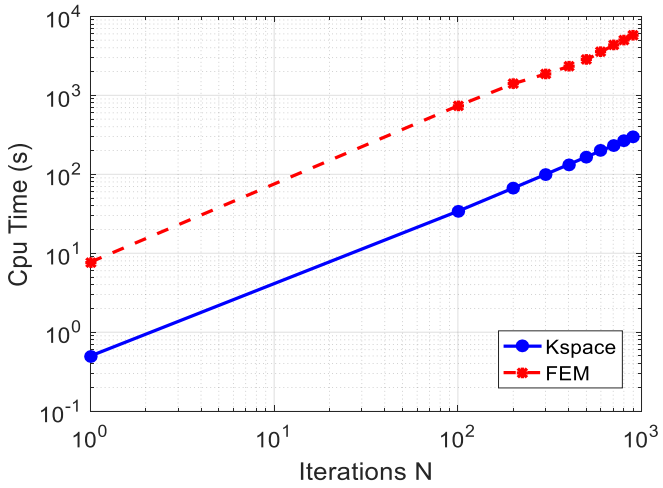

Figure 3. 8 Log-log plot of CPU time using k-space method compared with FEM method in different iterations.

Table 3. 1 CPU time comparison

Number of Iterations	10^0	10^1	10^2	10^3
K-space CPU Time(s)	0.4993	3.476	34.0586	330.0564
FEM CPU Time(s)	7.7128	70.5341	735.4135	6502

3.4.2. Demonstration Examples

Case 1: Homogeneous Material – Aluminum Plate

To illustrate the proposed framework, an example of an aluminum plate with embedded defects is studied. The model is 100mm by 100mm by 20mm, and 15,625 elements are used to discretize the numerical model. A total of 156 sensors are used. Instead of having

one fixed actuator, multiple actuators are used by using a ‘flying’ sensor map and the input is excited by the actuator in sequence following the scanning line as shown in Fig. 3-9. The ‘flying’ sensor improves the accuracy of model. The actuator shoots a tone-burst of 3.5 cycles, and the center frequency is 150Khz. The embedded damage of various shapes is distributed randomly inside the block as shown in Fig. 3-10(b). As discussed in the beginning of Section 2, the damage is considered as a reduction in shear modulus. The material properties are given in Table. 3-2.

Table 3. 2 Material properties of aluminum

	E(GPa)	G(GPa)	v	$\rho(kgm^{-3})$
aluminum	79	26	0.33	2700

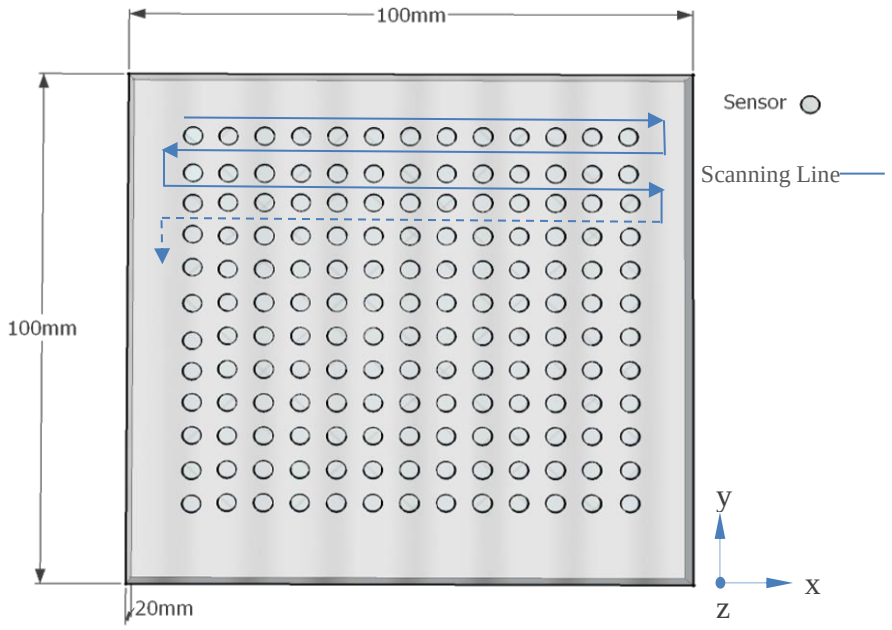

Figure 3. 9Aluminum block with sensors in a scanning pattern

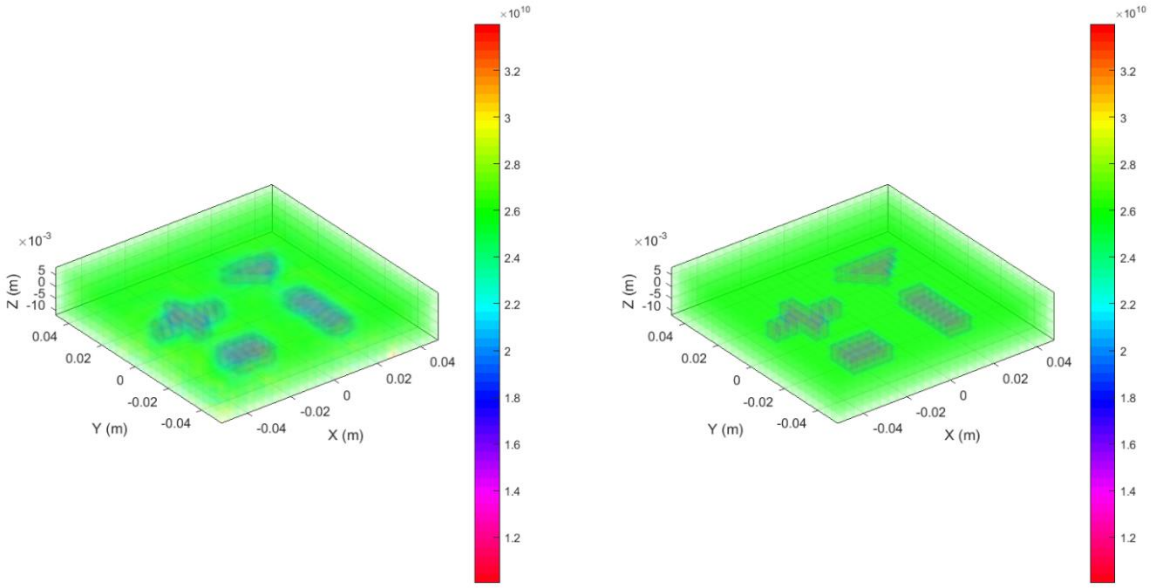

Figure 3. 10(a) Reconstruction of damage in the aluminum block; (b) Pre-defined damage embedded in the block.

A 3D view of the reconstructed and pre-defined damage map is shown in Fig. 3-10. The information of the middle cross-section in *the xy* plane is extracted to have a clear view on the reconstruction result. The synthetic distribution of shear modulus is shown in Fig. 3-11(b) and the reconstruction result is shown in (a). The result and the error compared to synthetic data in the x-direction on A-A' plane and the result in the z-direction(height) on B-B' are shown in Fig. 3-12. Very good agreement is observed for both the location and magnitude of the shear modulus reduction regions.

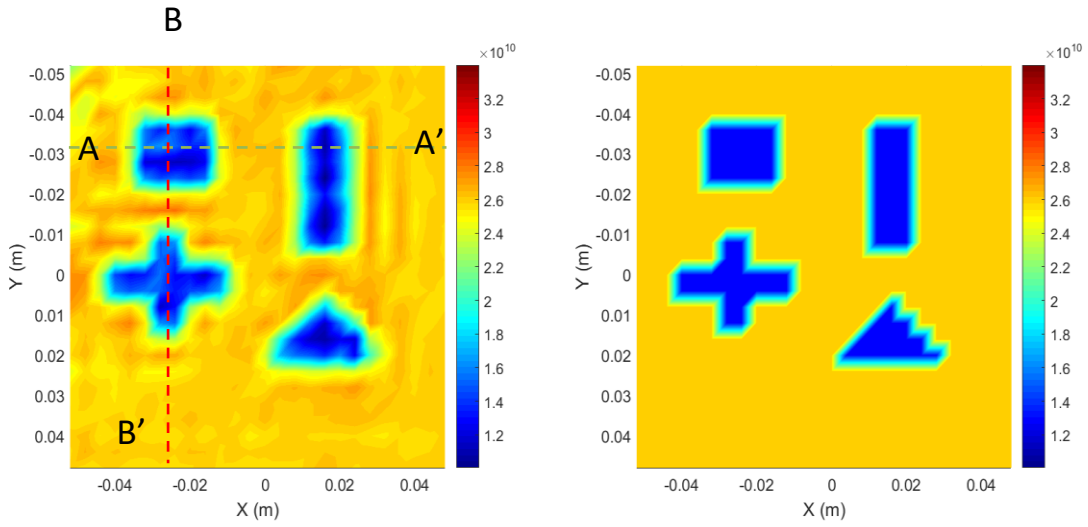

Figure 3. 11 (a) Reconstruction on the middle slice; (b) predefined damage of middle slice.

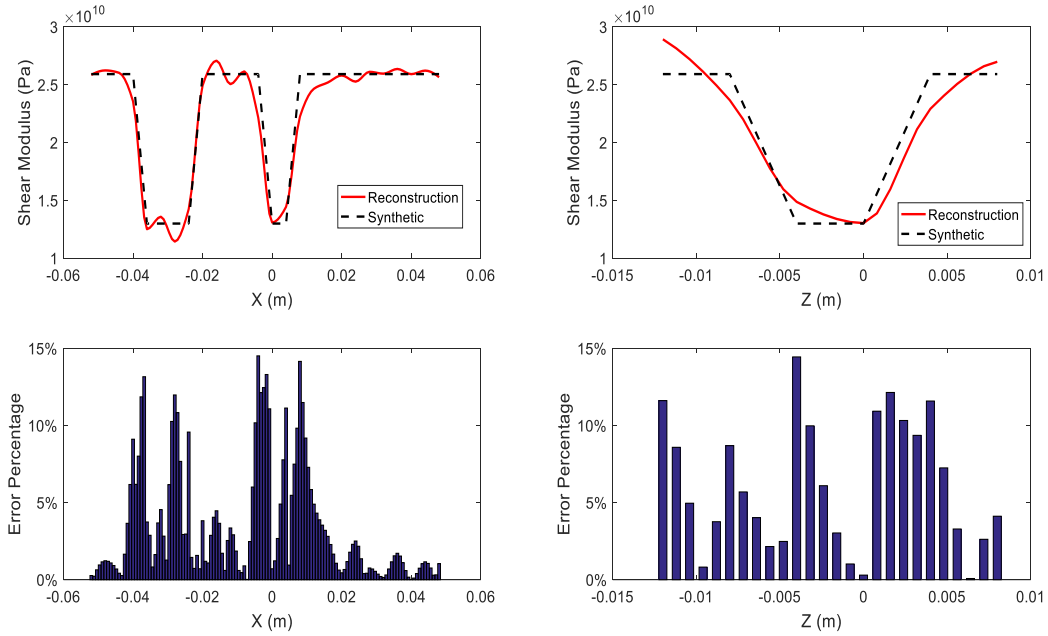

Figure 3. 12 (a)Reconstruction of the line on cross-section A-A' in x direction; (b) Error distribution of line in A-A'; (c) Reconstruction of the line on cross-section B-B' in z direction; (d) Error distribution of line in B-B'.

CASE 2: HOMOGENEOUS MATERIAL – PLAIN CONCRETE

The proposed framework is used to solve a practical problem in this section. A concrete specimen containing voids and flaws is studied. The model was studied using shear-wave ultrasound techniques, ground penetrating radar, air-coupled ultrasonic, etc. in [65]. Material properties and wave speed are shown in Table. 3-3. The pre-defined concrete model is shown in Fig. 3-13(a) where surface crack and honeycombing are on the left part of the concrete block. The block is 200 cm by 120cm by 18cm, and the numerical model is discretized into 87,516 elements. There are 49 sensors arranged in an indexed order on the top surface and the defects are located near the bottom surface. The sensor is either actuator or receiver, like previous examples. The actuator is giving a 10Khz tone-burst of 3.5 cycles.

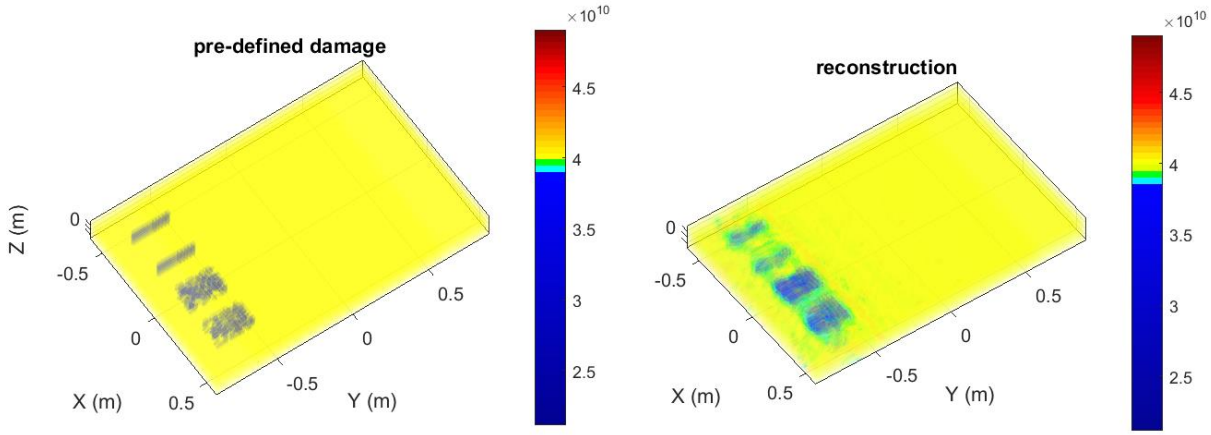

Figure 3. 13 (a) Predefined damage in concrete; (b) Reconstruction in concrete.

In Fig. 3-13, the distribution of shear modulus is shown where the honeycombing and surface crack are well reconstructed. The predefined distribution of honeycombing and cracks are shown in a planar manner in Fig. 3-14(b). The related reconstruction result is shown in (a).

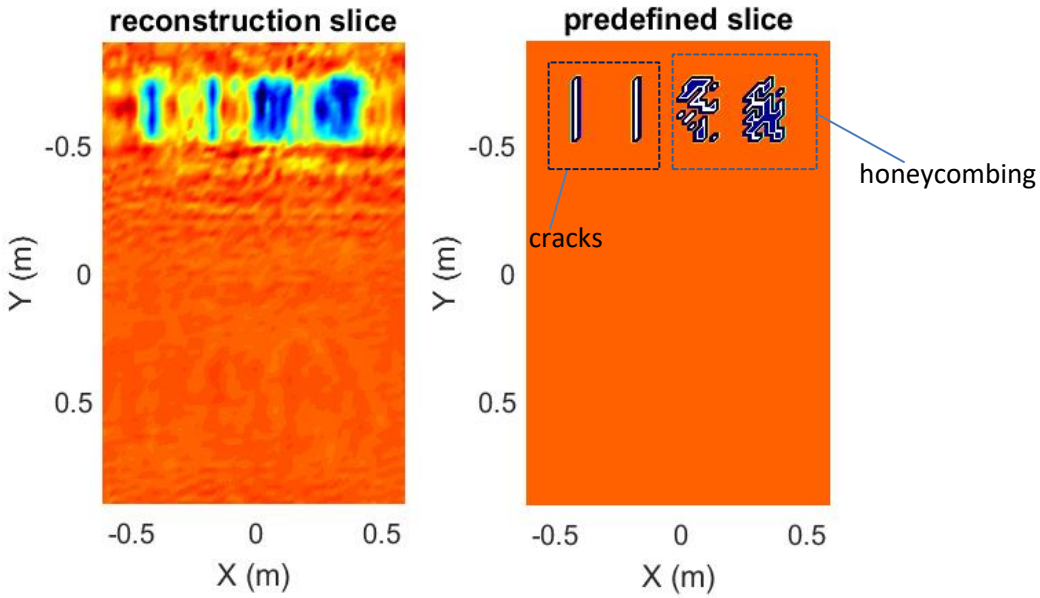

Figure 3. 14 (a) Reconstruction damage in 2D; (b) predefined damage in 2D.

Table 3. 3 Material properties used in plain concrete model.

$V_{compression}$ (ms^{-1})	V_{shear} (ms^{-1})	$\rho(kgm^{-3})$
7637.6	4082.5	2400

Comparing the result with the pre-defined damage from Fig. 3-13,14, it's seen that the proposed framework can identify and reconstruct the defects on the surface and inside the structure.

CASE 3. HETEROGENEOUS MATERIAL – REINFORCED CONCRETE WITH STEEL LINER

The above two examples show the applicability of the proposed method for homogeneous materials. Realistic 3D structures usually involve multiple phase of materials and is heterogeneous, such as composite materials and reinforced concrete structures. A

demonstration example is presented to check the applicability of the proposed methodology for heterogeneous 3D structures. The example studied in this section is inspired by the concrete structure in nuclear power plant[65] . The model is shown in Fig. 3-15 that a 40cm by 40cm by 100cm concrete block and a steel plate liner on the inner surface is modeled. The numerical model is discretized by 128,000 elements. Corrosion is considered happenning on the steel plate contacting the concrete since organic materials contacting steel leads to corrosion[82]. Heavy reinforcement is used for the required safety of nuclear power plant. Defect 1 and 2 are randomly embedded inside the block. The objective is to reconstruct the defects and corrosion through the thickness, and the location of rebar. The 'flying' sensor map is also used in the numerical model. A total of 49 sensors/actuators are placed in an indexed order on the bottom surface. The source is a 3.5 cycle tone-burst of 5kHz in *z* direction. The reconstruction result is shown in Fig. 3-16, which is a binarized image to only show the damage part. The pixel value of the reconstruction image is normalized to be in range of 0-1, then an optimized threshold of 0.4 is set to isolating the damages from the model[83]. The pixel value turns to be one if its value is bigger than the threshold and are shown in green in Fig. 3-16; it becomes blank/zero if the value is bigger than the threshold, as shown in Fig. 3-16. Therefore, only the damage part is isolated and displayed. Since the threshold is a constant, it may not work perfectly to all different types of damage in the model. Therefore, some of the non-damaged part is mistaken to be damage and vice versa, as seen in Fig. 3-16. In general, the proposed methodology can characterize the overall damage distribution in this large 3D structure. It is seen that the results for this complex structure is not as good as the

homogeneous case. Complex internal deflection of waves makes the identified damage very noisy. Both type I and type II errors are s

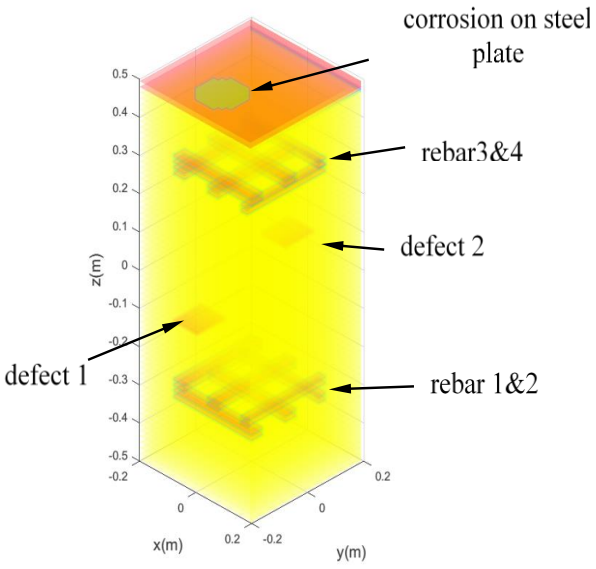

Figure 3. 15 Reinforced concrete wall of a reactor, rebar and damage distribution

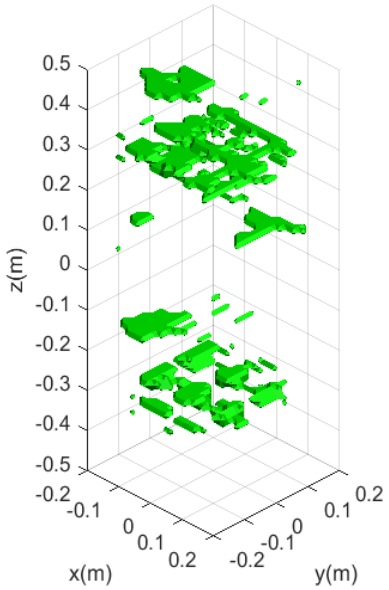

Figure 3. 16 Reconstruction result by setting a threshold to only show the rebar and defects.

3.5. Numerical Inverse Tomography on Simple Laminated Composites

In Chapter 3, the inverse tomography on isotropic model is performed, where the tuning variable can be one of mechanical properties like Young's modulus, Shear modulus, density and Poisson ratio, absorption coefficient, etc. In composites or anisotropic material, the defects have variety of property change where two or more tuning parameters should be considered in the model. Demonstration examples of multiple parameters deduction in the material is discussed in the following sections.

3.5.1. Elastic Constants Damage Reconstruction in Orthotropic Material At Multiple Location

The model is a simple two-layer composites and properties can be found in Table. 3-1. The model is 10cm by 10cm by 2mm. Two types of defects are defined, E_1 and E_2 reduction which are arbitrarily located on the sample as shown in Fig. 3-7(a). Both damages are through thickness. Sensors is located near the edges on the sample. Each sensor can act either as actuator or receiver to scan the model surface. The true damage distribution is shown in (c) (e) and reconstruction results are shown in (b) and (d). The damage location and value of properties can be well reconstructed.

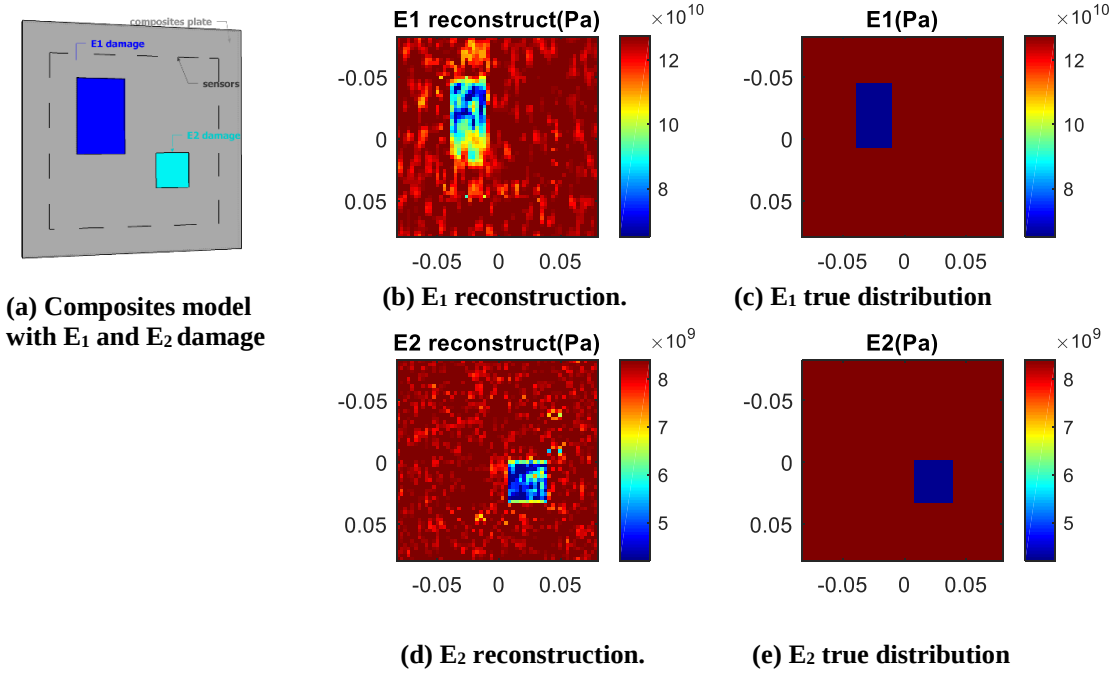

(a) Composites model with E_1 and E_2 damage

(b) E_1 reconstruction.

(c) E_1 true distribution

(d) E_2 reconstruction.

(e) E_2 true distribution

Figure 3. 17 E1 and E2 reconstruction results

3.5.2. Multiple Stiffness Deduction Damage Reconstruction at One Location

The constitutive relation can be either written in the form of elastic constants, E_1, E_2, E_3 and Poisson ratio v_{12},v_{23}, v_{13}. It can be also written in the form of stiffness matrix C_{ij}. The advantage of directly using stiffness components is relieving the pain on gradient

calculation using multiple chain rule. More specifically, the gradient of objective function S w.r.t E_1 can be formed as,

$$
\begin{aligned}
c_{11} &= E_1(1-v_{23}v_{32})r, \\
\frac{\delta S}{\delta E_1} &= \frac{\delta S}{\delta c_{11}}\frac{\delta c_{11}}{\delta E_1} + \frac{\delta S}{\delta c_{12}}\frac{\delta c_{12}}{\delta E_1} + \frac{\delta S}{\delta c_{13}}\frac{\delta c_{13}}{\delta E_1} + \ldots, where \\
\frac{\delta S}{\delta c_{11}}\frac{\delta c_{11}}{\delta E_1} &= (1-v_{23}v_{32})r + \frac{\delta S}{\delta E_1}(E_1(1-v_{23}v_{32})), wher \\
\frac{\delta S}{\delta E_1} &= \frac{\delta r}{\delta v_{21}}\frac{\delta v_{21}}{\delta E_1}, where \\
r &= \frac{1}{(1-v_{12}v_{21}-v_{23}v_{32}-v_{32}v_{13}-2v_{21}v_{32}v_{13})}
\end{aligned}
\tag{3.5.1}
$$

It's seen that multiple chain rule is used if the tuning variable is elastic constant. The additional computational cost can be avoided by using the stiffness components instead of elastic constants. The stiffness deduction damage is discussed in the following example. Multiple components [c_{11} c_{12} c_{22} c_{23} c_{44} c_{55}] have certain level deduction at the same time in one location. The material is same as the one using elastic constants.

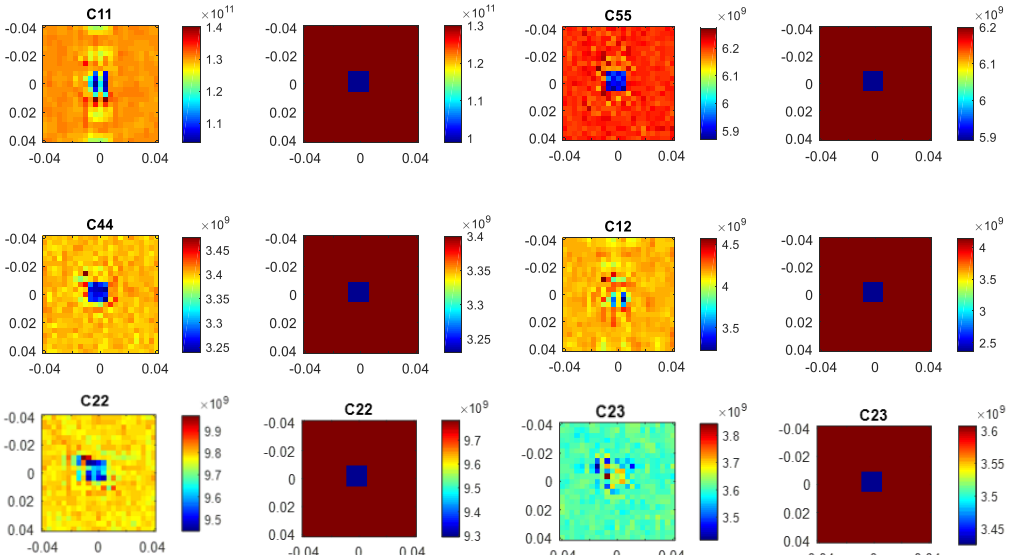

Figure 3. 18 Damage reconstruction and true damage of stiffness components

The objective function update under each iteration of some stiffness components is plotted in Fig. 3-9. The convergence rate will be discussed in the future work.

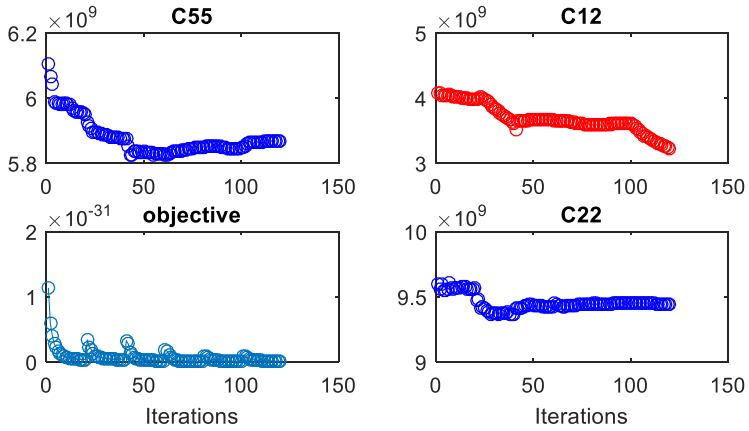

Figure 3. 19 The objective function under each iteration of c_{55}, c_{12} and c_{22}

4. Experimental Validation of The Adjoint Inversion Damage Imaging

4.1. Abstract

Aging-related damage and failure in structures, such as fatigue cracking, corrosion, and delamination, are critical for structural integrity. Most engineering structures have embedded defects such as voids, cracks, inclusions from manufacturing. The properties and locations of embedded defects are generally unknown and hard to detect in complex engineering structures. The structures integrity highly depends on the long-term damage accumulation. Therefore, early detection of damage is beneficial for prognosis and risk management of aging infrastructure system. Quality control and abnormality detection is important for the risk assessment of structures under external loadings.

Non-destructive testing (NDT) and structural health monitoring (SHM) are widely used for this purpose. Different types of NDT techniques have been proposed for the damage

detection, such as acoustic wave, thermography, eddy current, microwave. The advantages of acoustic wave propagation methods are discussed here. The prior knowledge of input great facilitates the damage identification based on waveform information. Since the waveform from one actuator can be received by multiple receivers, any change on received waveform is a strong indicator of damage existence. Therefore, the waveform or extracted features are key information of damage detection. The focus in this study is on the acoustic wave-based detection method, which is grouped into two major categories: feature-based damage detection and model-assisted damage detection. Both damage detection approaches have their own pros and cons. Feature-based damage detection is usually very fast and doesn't involve in the solution of the physical model. The key idea is the dimension reduction of signals to achieve efficient damage detection. The disadvantage is that the loss of information due to the feature extraction can induce significant uncertainties and reduces the resolution. The resolution of the feature-based approach highly depends on the sensing path density. Model-assisted damage detection is on the opposite side. The highlight for model-assisted damage detection is the ability for high resolution imaging with limited number of sensing paths since the entire signal histories are used for damage identification. Model-based methods are time-consuming due to the requirement for the inverse wave propagation solution, which is especially true for the large 3D structures.

Based on the brief review, the motivation of the proposed method is to develop efficient and accurate model-based damage imaging technique with limited data. The special focus is on the efficiency of the damage imaging algorithm as it is the major bottleneck of the model-assisted approach. The computational efficiency is achieved by

two complimentary components. First, a fast wave propagation solver is proposed, which is verified with the classical Finite Element(FEM) solution and the speed is 10-20 times faster. Next, efficient inverse wave propagation algorithms is proposed. Classical gradient-based optimization algorithms usually require finite difference method for gradient calculation, which is prohibitively expensive for large degree of freedoms. An adjoint method-based optimization algorithms is proposed, which avoids the repetitive finite difference calculations for every imaging variables. Thus, superior computational efficiency can be achieved by combining these two methods together for the damage imaging. A coupled Piezoelectric (PZT) damage imaging model is proposed to include the interaction between PZT and host structure. Following the formulation of the framework, experimental validation is performed on isotropic and anisotropic material with defects such as cracks, delamination, voids. The results show that the proposed method can detect and reconstruct multiple damage simultaneously and efficiently, which is promising to be applied to complex large-scale engineering structures.

The formulation of the forward and inverse damage imaging is discussed in previous chapters, the focus of this chapter is on the experimental validation on various materials with common engineering structures such as cracks, delamination, holes. A novel PZT-coupled damage imaging model is proposed and validated with experimental data. The major advantages and uniqueness are summarized:

1. Compared to feature- based approach [14], the proposed framework relaxes the requirements on measurements and time spent on training data;
2. The forward solver uses coupled first-order equations which is easy to solve in mathematical view.

3. The sensitivity problem is derived and solved using the k-space method which helps to improve the computational efficiency.
4. A novel PZT-coupled adjoint damage imaging is proposed, the interaction between PZT and host structures are included in the damage imaging methods, which further improves the accuracy compared to the coupled FEM models.
5. The capability of simultaneous multiple damage identification with a sparse sensors configuration compared to full-filed measurements methods [68].
6. PZT sensors are used to generate and receive waveform data in the experiments. The generated wave can travel long distance which works well for large engineering structures with insulation and coating and are sensitive to multiple defects[84].
7. The proposed study shows feasibility and potential of efficient baseline-free for multiple damage detection on engineering structures with a sparse sensor configuration.

4.2. Introduction

Aging-related damage and failure in structures, such as fatigue cracking, corrosion, and delamination, are critical for structural integrity and early detection of damage is beneficial for prognosis and risk management of aging infrastructure system. In addition, most engineering structures have embedded defects such as voids, cracks, inclusions, etc. from manufacturing. The properties and locations of embedded defects are generally unknown and hard to detect in complex engineering structures. Quality control and

abnormality detection is important for the risk assessment of structures under external loadings.

Non-destructive testing (NDT) and/or structural health monitoring (SHM) are widely used for this purpose. Different types of NDT techniques have been proposed for the damage detection, such as acoustic wave, thermography, eddy current, microwave, and others[62][63]. The focus in this study is on the damage detection of strong discontinuity defects such as cracks and delamination using experimental wave-based method. Therefore, only the related previous studies are briefly discussed as the following.

Crack is one of the most common defect in structures and are indicators of degradation of structures integrity. Early detection is necessary to prevent crack propagation which leads to possible structure failures. Non-destructive crack detection methods are well developed in recent years since fast for this purpose. The state of the art is briefly reviewed. Image-based damage detection methods such as Infrared (IR) thermography, ultrasonic imaging, thermography are used for surface crack detection[87]. Image-based methods has the advantage of high resolution than manual inspection methods. However, it requires efficient technique for data processing such as image segmentation and data deduction[88].Other methods such as MEMS based Structure Health monitoring(SHM) methods used for defect detection in aerospace structures[87].

PZT-based wave propagation is widely used in Structure Health Monitoring. It has the advantage of nonintrusive, inexpensive, broadband wave generation and lightweight for the purpose of in-situ and offline structure inspection[92][93]. Therefore, accurate and efficient model of wave propagation using PZT sensors are necessary. Due to the

complex wave propagation pattern especially in composites material and large-scale structures, FEM-based model is widely used to study the wave integration with defects. a FEM wave propagation model and Neural network method for detection of through-hole defect in laminate composites is discussed [94]. A 2d lamb wave interaction with slot-like defects in metallic structure using FEM is discussed in,[95] [96]. A Spectral Element Method(SEM) is used to simulated PZT induced wave in metallic material[97].

Some analytical methods are investigated. Analytical method on the PZT induced wave interacting with damage are proposed [98]. Scattering of wave in model with discontinuity damage is discussed in [99] . An integrated PZT sensor plate model in metallic material is proposed based on Mindlin Plate theory[100]. An equivalent nodal force solution to model PZT actuator is mentioned in[101]. Some hybrid methods combining both numerical model analytical methods are studied [100][102].

To ensure accuracy of model in piezo sensor-based Structure Health Monitoring(SHM), it's essential to integrate direct and converse Piezo electric with the dynamics of the structure model. However, the computational efficiency of is the major bottleneck of model-based methods. In classical FEM dynamic model, 15-20 nodes should be sampled per wavelength is necessary to ensure convergence and accuracy. Therefore, the computational cost is heavy especially for large-scale structures and those made of anisotropic material.

The proposed study focus on the above difficulty and the motivation is to develop an efficient and baseline-free PZT induced forward and inverse wave propagation model for damage detection in isotropic and anisotropic material. The computational efficiency is

achieved by two complimentary components: first, a fast-forward wave propagation solver is needed. A k-space approach [19] is proposed for the damage imaging. Classical finite element-based solver is not appropriate for small damage detection due to the fine mesh requirement for the high frequency signals. Most model-based inverse methods mentioned in [10–13],[16] are based on FEM method. Compared to classical FEM method, the implementation of the k-space method in the proposed framework highly speeds up the simulation efficiency and saves computational memory [20]. Next, an efficient inverse wave propagation algorithm is proposed. Classical gradient-based optimization algorithms usually require finite difference method for gradient calculation, which is prohibitively expensive for large degree of freedoms (e.g., damage imaging in 3D structures) [71]. In this paper, an adjoint method-based optimization algorithms is proposed, which avoids the repetitive finite difference calculations for every imaging variables. Thus, superior computational efficiency can be achieved by combining these two methods together for the damage imaging.

The paper is organized as follows: First, the background and objective of the proposed damage imaging, and the state of art of existing damage detection methodology are reviewed. The improved model integrated with PZT damage imaging formulation is discussed. Demonstration experiments on various materials are performed. The detailed experiment preparation and procedures are discussed. Cracks, delamination, voids, which are commonly seen defects in engineering structures are reconstructed using the proposed method. It demonstrated that the ability of localization and identification the size and shape of various defects in the proposed study, which is promising to apply to complex structures. finally, some conclusions and future work are drawn based on the above study

4.3. Integrated PZT Damage Imaging Model

4.3.1. Coupled PZT Model Formulation

The piezoelectric constitutive equation in a strain-charge form is written as

$$S = s\sigma + dE \quad \text{Eq.4- 1}$$

$$D = d\sigma + \varepsilon E \quad \text{Eq.4- 2}$$

In which S is the strain components, s is the compliance coefficient, σ is the stress tensor, d is the piezoelectric coupling coefficient, ε is the electric permittivity and E is the electric field components. The PZT sensor in the tests are type PZT-5A disc from Steminc. The material properties and dimension are shown in the Table 4. 1. The PZT sensors can work either in an actuator mode when the input voltage is converted to strain. The receiver mode vice versa.

Actuator Mode

One common method to infer the displacement field for a structural component is done using the finite element method as shown in [30], [103]. A simplification is used in the proposed method that the equivalent displacement from the piezo sensor (PZT) disc is proportional to the electric voltage output of the PZT. The details of this simplification can be found in [104].

The PZT sensor is attached to the surface of the specimen. In the actuator mode, the strain in plane induced by an external voltage V_i applied on the PZT sensor is written as,

$$\varepsilon_{ra} = d_{31} V_i / h \quad \text{Eq.4- 3}$$

to the surface of the host structure. Therefore, the strain distribution in the thickness direction is continuous at the interface between the host structure and PZT surface [105]. The radial displacement at the interface is,

$$d_r = \frac{r_{pzt} d_{31}}{h}\left(\frac{E_h(1-\upsilon_{pzt})}{E_{pzt}} + 1\right)V_i = f(V_i) \quad \text{Eq.4- 4}$$

where r_{pzt} is the disc radius, ε_{ra} is the in-plane strain induced by the external voltage.

$$E_h = \frac{AE_{pzt}}{E} D - \frac{E_{pzt}}{(1-\upsilon_{pzt})} \quad \text{Eq.4- 5}$$

$$A = \left(\frac{1-\upsilon}{1-\upsilon_{pzt}}\right) \quad \text{Eq.4- 6}$$

$$B = 2EE_{pzt}Hh(1-\upsilon)(2h^2 + 3Hh + 2h^2) \quad \text{Eq.4- 7}$$

$$C = \frac{(E^2H^4(1-{\upsilon_{pzt}}^2) + {E_{pzt}}^2 h^4(1-\upsilon^2))}{(1-\upsilon_{pzt})} \quad \text{Eq.4- 8}$$

$$D = \frac{EE_{pzt}h(4EH^3 + 3EH^2h + AE_{pzt}h^3)}{(B+C)} \quad \text{Eq.4- 9}$$

where E, E_{pzt} are the Young's Modulus, H, h is the thickness, υ and υ_{pzt} are Poisson's Ratio of the specimen and PZT material, respectively. The equivalent displacement d_r is applied as an external force f(V) as shown in Eq.4- 3. The forward model is shown in Eq.4- 10. The details of the solution to it is discussed in CHAPTER 3.

$$\rho \frac{\partial^2 u_i}{\partial^2 t} = \frac{\partial \sigma_{ij}}{\partial x_j} + f(V) \quad \text{Eq.4- 10}$$

Receiver Mode

The PZT sensor can also convert the deformation back to voltage again. The output voltage V_o can be expressed as[93], [106],

$$V_o = \frac{E_{pzt} h d_{31}}{4K_3\epsilon_0\pi(1-\upsilon_{pzt})}\varepsilon_{rs} \quad \text{Eq.4- 11}$$

in which ε_{rs} is the in-plane strain of the PZT disc in the receiver mode. The in-plane displacement u_r on the edge of PZT is linear to strain ε_r [104],

$$u_r = \int_0^{r_{pzt}} \varepsilon_r dr \qquad \text{Eq.4- 12}$$

Therefore, the output voltage V_o is proportional to u_r, which can be written in a short form,

$$V_o = L(u_r) \qquad \text{Eq.4- 13}$$

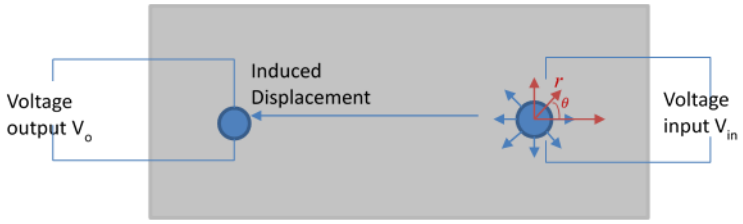

Figure 4. 1 Diagram of the coupled PZT model (actuator and receiver mode)

Coupled PZT Inverse Formulation

Objective Function

The adjoint -based inversion algorithm is discussed in CHAPTER 2. An improved integrated PZT inversion formulation is discussed here. The major improvement is integration of the piezoelectric effect into the inversion model. Since the major focus is on the strong discontinuity type defects such as cracks and delamination, the tuning parameter in the formulation is selected to be the material density. The objective function in term of material density ρ is written as,

$$minimize\{S(\rho)|\mathrm{S(P)} = \frac{1}{2}\int_0^{\mathrm{T}} \int_{\mathrm{V}} \sum_{\mathrm{n=1}}^{\mathrm{N}} \sum_{\mathrm{m=1}}^{\mathrm{M}} \left(\mathrm{u_{exp}}(\mathrm{x_m^n}, \mathrm{t}; \rho) - \mathrm{U_m^n}(\mathrm{x}, \mathrm{t})\right)^2 \mathrm{dVdt}\} \qquad \text{Eq.4- 14}$$

where the objective S is written as a function of experimental displacement $\mathrm{u_{exp}}$ and predicted displacement *U*. *T* is the duration of the measurement, and *M* is the total number of sensors of each actuator. N is the number of actuators and *V* is the domain of interest. The predicted displacement U_m is the solution of the wave propagation equations using the proposed k-space method. Given the material of PZT sensor in Table 4. 1, the

conversion between electric potential to displacement u_{exp} is obtained as shown in Eq.4-11 Eq.4- 13, which can be expressed as $u_{exp} = f(V)_{exp}$.

Adjoint problem

By introducing the adjoint variable $\boldsymbol{\lambda}$ into the objective function in Eq.4- 14,

$$S(\boldsymbol{P}) = \frac{1}{2}\int_0^T \sum_{n=1}^{N}\sum_{m=1}^{M}\int_V \left(f(V)_{exp}(\boldsymbol{x_m}, t; \boldsymbol{P}) - \boldsymbol{U_m^n}(\boldsymbol{x}, t)\delta(\boldsymbol{x} - \boldsymbol{x_m})\right)^2 dt\, dV dt$$
$$- \sum_{n=1}^{N}\int_0^T\int_V \boldsymbol{\lambda^n}(\boldsymbol{x}, t)\left(\rho\frac{\partial^2 \boldsymbol{u}(\boldsymbol{x}, t; \boldsymbol{P})}{\partial^2 t} - \nabla\cdot(\boldsymbol{C}:\nabla(\boldsymbol{u}(\boldsymbol{x}, t; \boldsymbol{P}))) - \boldsymbol{f^n}\right) dV dt \quad \text{Eq.4- 15}$$

By using the Gaussian theorem and integral by parts, the variation on $\boldsymbol{S}$ in the direction of density is

$$\Delta S(\rho) = \sum_{n=1}^{N} -\int_0^T\int_V \rho\boldsymbol{\lambda^n}\frac{\boldsymbol{d^2 u^n}}{\boldsymbol{d^2 t}} dV dt \quad \text{Eq.4- 16}$$

and the gradient δS is approximated by,

$$\delta S = \frac{\Delta S(\rho)}{\Delta\rho} = \sum_{k=1}^{K}\frac{\Delta S(P_k)}{\Delta P_k} = \sum_{\boldsymbol{n=1}}^{N}\left(-\int_0^T\int_V \boldsymbol{\lambda^n}\frac{\boldsymbol{d^2 u^n}}{\boldsymbol{d^2 t}} dV dt\right) \quad \text{Eq.4- 17}$$

Sensitivity Problem

A sensitivity problem is discussed since the solution is used for the computation of the step size in the CG method. In the following discussion, material density is used for the parameter P. Other material properties, such as Modulus and attenuation coefficient, can be used as the parameter P in a similar way. The displacement u becomes (u+Δu) by adding a perturbation Δu and the density ρ becomes (ρ +Δ ρ) along the direction of estimated variable $\boldsymbol{\rho}$. The displacement variation $\boldsymbol{\Delta u}$ is a function of space coordinate x,

time t, and $\Delta\rho$, i.e., $\Delta\boldsymbol{u} = \Delta\boldsymbol{u}(\boldsymbol{x}, \boldsymbol{t}; \Delta\rho)$. The sensitivity equation is by using Taylor expansion,

$$\rho\frac{\partial^2\Delta\boldsymbol{u}}{\partial^2 t} = \nabla\cdot\left(\boldsymbol{C}:\nabla(\Delta\boldsymbol{u})\right) - \Delta\rho\frac{\partial^2\boldsymbol{u}}{\partial^2 t} \qquad \text{Eq.4- 18}$$

The solution of sensitivity problem $\Delta\boldsymbol{u}$ is solved by the proposed forward solver since the similarity to the forward wave equation, and the external force becomes $-\Delta\rho\frac{\partial^2\boldsymbol{u}}{\partial^2 t}$.

Multiple-path Conjugate gradient optimization

A CG (Conjugate Gradient) method combining the adjoint method is used for parameter estimation. The parameter is optimized with all sensor path information included simultaneously. Eq.(3.3.27)and (3.3.29) show the formulation of CG, where i is the number of iterations, and P is unknown parameter. The value of P is updated along searching direction $\boldsymbol{d}$ iteratively [77]–[79],

$$\rho^{i+1} = \rho^i + \sum_{act=1}^{M}(\beta^i)_{act}\boldsymbol{d}^i{}_{act} \qquad \text{Eq.4- 19}$$

where β^i is searching step size and total of M actuators are activated. In classical CG, the step size β is a function of sensitivity matrix[72]. In the proposed framework, a line search technique is used to simplify the equation so that the step size is in term of $\Delta\boldsymbol{u}$ instead of the sensitivity term [80]. The expression is shown in Eq. (3.3.28),

$$\beta^i{}_{act} = \frac{\sum_{n=1}^{N}\sum_{m=1}^{M}\int_0^T(\boldsymbol{U_m^n}(\boldsymbol{x},t)^i - \boldsymbol{u_m^n}{}^i)\cdot(\Delta\boldsymbol{u^n}(\boldsymbol{x_m},t))^i dt}{\sum_{n=1}^{N}\sum_{m=1}^{M}\int_0^T(\Delta\boldsymbol{u^n}(\boldsymbol{x_m},t))^i\cdot(\Delta\boldsymbol{u^n}(\boldsymbol{x_m},t))^i dt} \qquad \text{Eq.4- 20}$$

where Δu^n is obtained from the solution of the sensitivity problem, Eq. 0.5. The searching direction $\boldsymbol{d}$ of an actuator is,

$$\boldsymbol{d}^i{}_{act} = -\nabla S_{act}(\rho^i) + \gamma^i{}_{act}\boldsymbol{d}^{i-1}{}_{act} \qquad \text{Eq.4- 21}$$

where initial value $\boldsymbol{d}^0=-\nabla S(\rho^0)$, γ is the conjugation coefficient and the expression is shown in Eq. (28) , which is in the form derived by *Polak* [11,19].

$$\gamma^i{}_{act} = \frac{\nabla S(\rho^i)^T(\nabla S(\rho^i) - \nabla S(\rho^{i-1}))}{\nabla S(\rho^{i-1})^T \nabla S(\rho^{i-1})} \qquad \text{Eq.4- 22}$$

where δS is obtained by Eq. (3.3.26) in terms of adjoint variable $\boldsymbol{\lambda}$.

The computation steps are summarized as the following,

1. Compute the direct problem given initial guess of unknown parameter ρ.
2. Compare the experimental equivalent displacement $f(V)_{exp}$ recorded by sensors with estimated displacement $\boldsymbol{U_m}$ by computing objective function.
3. Set a proper stopping criterion based on the objective, i.e. a threshold ε that if $S(\rho)<\varepsilon$, stop the iterations; If not, go to Step 4,
4. Compute $\Delta\boldsymbol{u}$ by solving the sensitivity problem,
5. Compute $\boldsymbol{\lambda}$ by solving the adjoint problem
6. Given $\boldsymbol{\lambda}$ and the estimated density ρ, compute gradient grad$S(\rho)$ using Eq. (25),
7. Compute conjugation coefficient γ^i and searching step size β^i
8. Update ρ^i to ρ^{i+1}
9. Let iteration number $i=i+1$ and start from Step 1 to Step 8 again.

Table 4. 1 Material Properties of PZT-5A

density(kg/m3)	charge constant d31(10-12m/V)	charge constant d33(10-12m/V)	Relative dielectric constant	Diameter(mm)
1780	-190	450	1580	7

4.4. EXPERIMENTAL VALIDATION of DAMAGE IMAGING

Experiments are conducted using surface mounted (Piezo-electric) PZT sensors on aluminum 2024-T3 and Carbon Fiber Reinforced Polymer (CFRP) T700G. Various shape cracks are made on the aluminum sample. The CFRP samples has pre-inserted Teflon between plies to model delamination. The wave signals are collected by an automatic data acquisition system.

4.4.1. Experimental Setup

The test set up is shown in Fig. 4-1. The automatic data acquisition system consists the AGILENT A1000 function generator, Tektronix DPO2000 oscilloscope, IA-3000 Relay control multiplexer, STEMINC PZT discs are mounted on the sample surface. The laptop controls the function generator and oscilloscope to actuate and save waveform signals using the LabVIEW program. The sample preparation and experiment procedures are summarized:

Sample Preparation

Clean the sample with acetone to be prepared for PZT sensor mounting. The sensor layout of the aluminum sample is shown Figure 4. 4. The locations of sensors are first marked with a pencil on the sample surface. The area is polished with a sand paper to have a stable interaction between PZT wafer and the sample and the area is cleaned with acetone again. Proper amount of Rapid fuse glue is applied on the bottom surface of the PZT wafer. Put the glued side of the sensor on the marked location on the sample and apply proper pressure on the top surface of the PZT for 20 seconds until the glue dried.

Experiment Procedures

The data collection process is shown in . First, an Agilent 1000 arbitrary function generator excites 20 Volts peak-peak Hanning-windowed 3 cycles tone-burst to the common I/O C_1 on the MUX trough a BNC cable. The C1 group contains 16 channels connected to PZT actuators. The receivers are also connected to the other group of channels of C_2. For example, an PZT sensor A_1 can be the actuator and other PZT S_2 to S_{32} are receivers. In next run, sensor A_i can be actuator (i=2, 3, ..., N) and the remaining sensors are receivers. A Tektronix DPO2024 oscilloscope acquires the waveform data and save the data automatically using a LabVIEW program. The flowchart of the experiment setup is shown in Figure 4. 3. The data acquisition system including the MUX, oscilloscope and function generator is shown in Figure 4. 2 and Figure 4. 3.

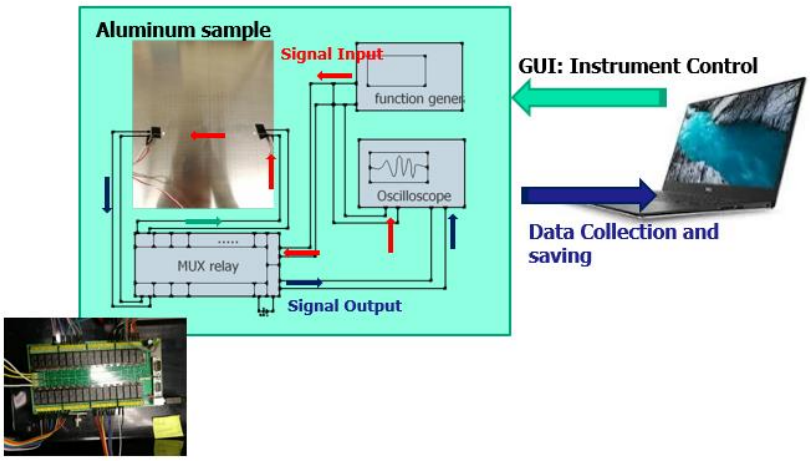

Figure 4. 2 Diagram of the experiment setup

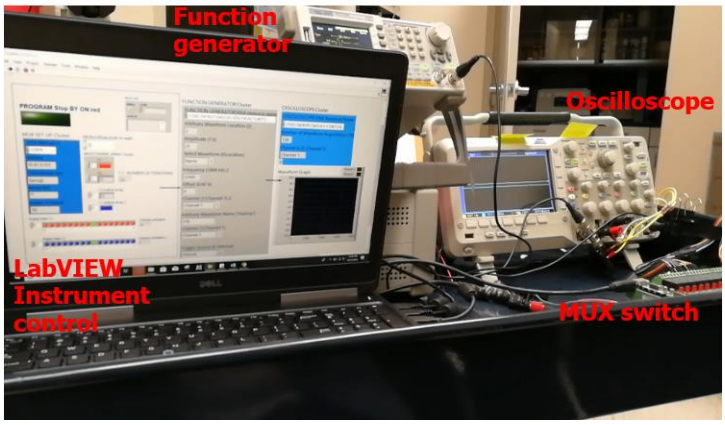

Figure 4. 3 Experiment set up- signal generation and data acquisition.

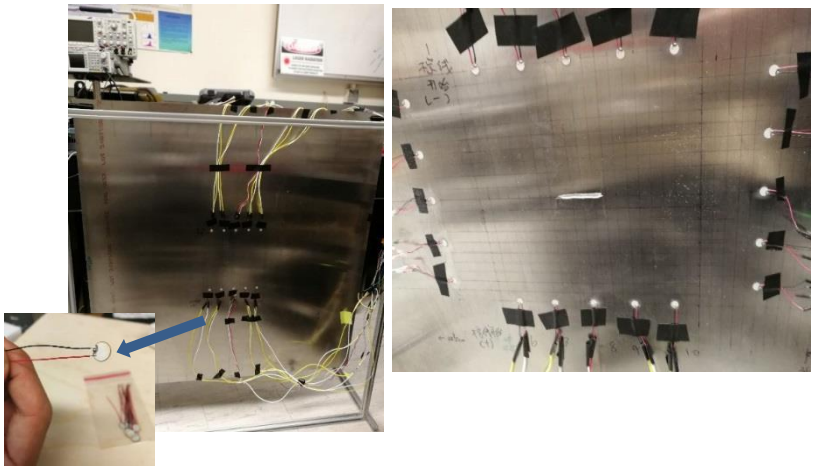

Figure 4. 4 Damage 1 Linear crack on aluminum 2024-t3 sample and PZT sensors layout

4.4.2. Isotropic Material

Experiments Setup

An 914mm by 914mm by 1.6mm aluminum T2024 plate with a line crack and a void defect is used for demonstration. The linear crack is 3.5mm in length and 2mm in height. The PZT discs are attached on the surface with a 7mm diameter and 0.2mm thickness. The sensor layout is shown in Figure 4. 4. The center frequency of the excitation signal is 150kz in the range of non-dispersion region in the frequency thickness product curve of aluminum [107]. Material properties are given in Table 4. 2.

Table 4. 2 Material properties of aluminum T2024.

	Yong's Modulus(Pa)	**Shear Modulus(Pa)**	**Poisson Ratio**	**Density(kgm^{-3})**
aluminum	70e9	1.31e10	0.33	2700

Damage Imaging Results

The interval of PZT sensor is 4cm.The distance of sensor arrays which are parallel to the crack is 0.2m. The sensor array normal to the crack length is 0.3m apart. Total of 20 PZT sensors are used which can either work in actuator or receiver mode. The reconstruction result of a 3.5 cm linear crack is shown in Figure 4. 5. The result of multiple defects including the linear crack and void with diameter of 0.8cm is shown in Figure 4. 6. The noise at the PZT sensor location is not eliminated totally by applying a constant threshold. This may need further discussion and will be discussed in the future work.

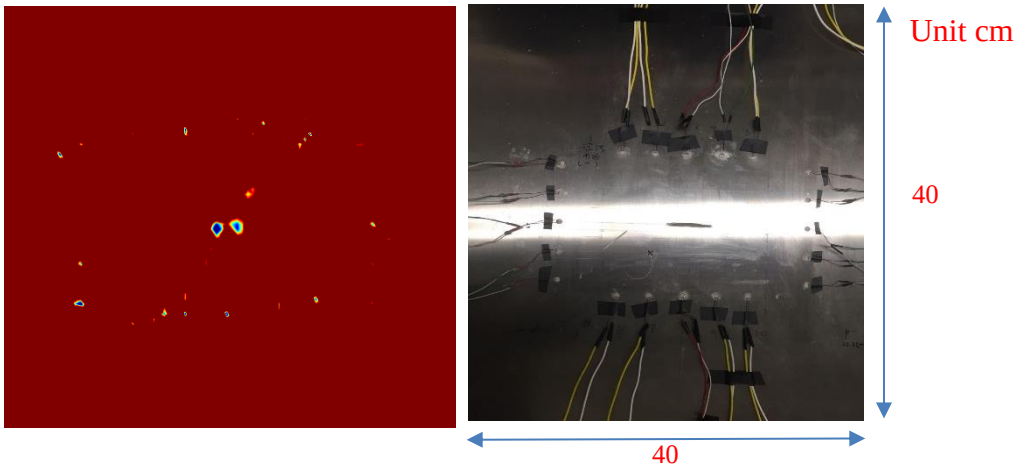

Figure 4. 5 Damage Imaging of linear crack

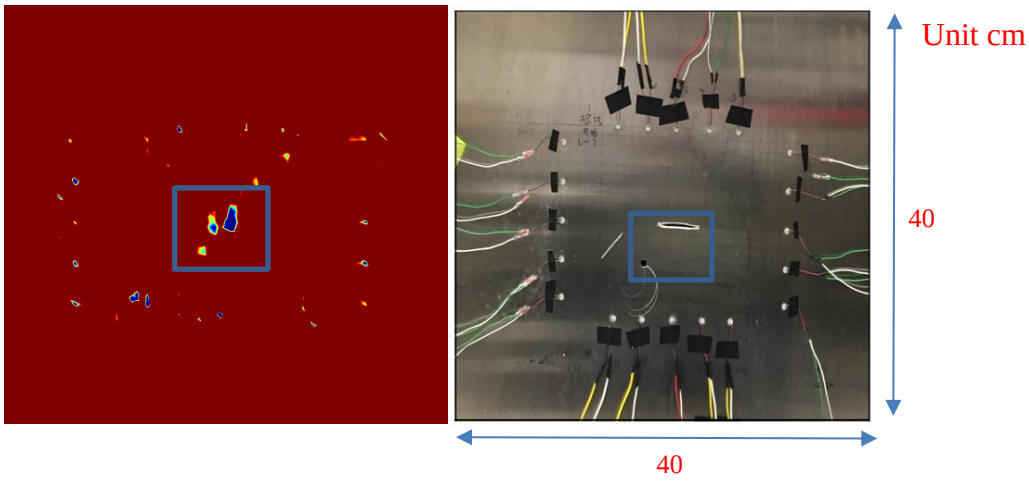

Figure 4. 6 Damage Imaging of multiple defects (void and linear crack)

4.4.3. Anisotropic Composites Laminate

Experimental Setup

Demonstration testing is performed on T700G laminated composites. The ply layup is $[0_2/90_4]_s$ with Teflon inserted at the middle layer which is an artificial delamination. The delamination is 2.54cm in diameter. The PZT sensors are Steminc PZT-5A which are mounted on the specimen surface. The sensor layout is show in Figure 4. 7. Each PZT

works as an actuator or receiver. The data acquisition system is same as the one in the aluminum test.

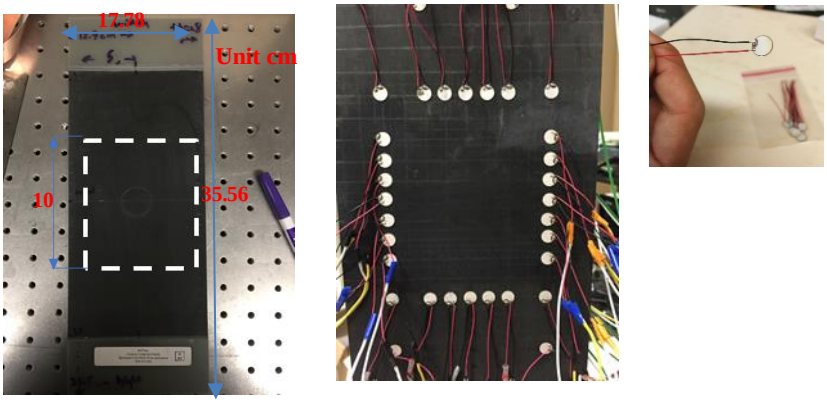

Figure 4. 7 Sensor Configuration of Laminated Composites CFRP T700G with center delamination

Damage Imaging Results

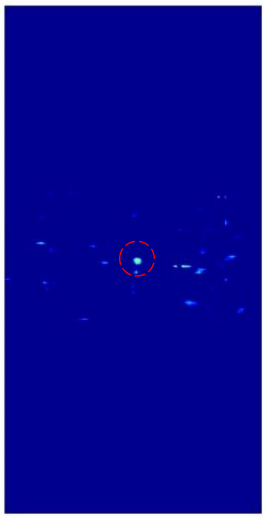

Figure 4. 8 Damage Imaging of laminated composites with center delamination

Discussion

The delamination area can be reconstructed using the proposed method. The variation caused by the signals can be seen on the right side of the delamination. The uncertainty caused by the experimental data should be addressed. The related sensitivity analysis will be done in the future work.

5. CONCLUSION AND FUTURE WORK

5.1. Chapter 2

A k-space method for wave propagation in damaged anisotropic solids is proposed in Chapter I. Numerical examples are used to demonstrate and verify the proposed methodology. Several major conclusions are,

- The proposed k-space formulation with two coupled first order differential equations and the wave number correction scheme are shown to be very accurate in the simulation of wave propagation in general anisotropic materials in the 2D and 3D domain;
- In the 2D simulation, the crack length has larger impact on the received wave amplitude and time of arrival compared to the crack density;

The combined effect of crack length and crack density is much more complex than a simple empirical model can predict, which indicates that it is necessary to use a model-assisted approach for damage detection in the future;

- The embedded subsurface crack has less impact on the received signal compared to the surface damages in the current investigation;

The CFL number needs to be reduced to compensate for the strong discontinuity and to ensure the stability in the numerical model. In the simulation examples, the CFL number of 0.1 for composites, anisotropic material and 0.3 for isotropic material are used respectively, which is shown to perform well for the investigated cases

- The current focus is on the forward simulation using the k-space method. Due to its superior computational efficiency, the inverse formulation using the k-space method should be investigated and will greatly facilitate the damage detection. Experimental validation with the proposed methodology is also required and is ongoing. Uncertainties associated with the material and measurements need to be included in the future for practical applications.
- A standard grid is used in the proposed study. The staggered grid is known to increase stability and accuracy but not required in spectral as mentioned in [41] [109]. Most work using the staggered grid focus on the wave propagation in soft material such as tissues and weakly heterogeneous material, and few of them focus on solids with strong discontinuities including cracks and delamination to the author's knowledge. It is mentioned that the staggered grid can yield inaccurate results or instability problems when the propagation of waves in media with high contrast of elastic parameters or strong fluctuations as mentioned in [42] [110] [111]. The discussion on standard staggered grid can be also found in the Introduction section. As mentioned in [42], the use of staggered-grid formulations mitigates problems like Nyquist errors and generation of non-usual artefacts when solving first-order wave equations. But the standard staggered-grid PSM cannot tackle anisotropy with symmetry lower than orthorhombic. A

previous study on this issues can be found in [42]. Detailed investigation using the proposed framework needs further study is listed as future work.

- The proposed study aims for the damage detection using transmitted waves. The first-time window waveform is the key feature in damage detection. The time of arrival and amplitude varies if damage exists. An accurate Linear-slip model incorporated Discontinues Galerkin method is proposed to study the transmission and reflections from fractures in [31]. The authors would like to include the discussion on reflected wave in the future work.
- The proposed framework uses a Forward Finite Difference in time discretization. A Central Difference scheme is compared with the Forward Difference scheme. It's found both methods converge around the same mesh size. The accuracy and convergence rate using different approximation orders need further investigation and details will be included in future work.

5.2. Chapter 3

A new damage imaging methodology combining k-space forward wave propagation solver and an adjoint method-based conjugate gradient optimization algorithms is proposed in Chapter II. Numerical simulations and parametric studies are used to verify the proposed methodology and applicability to various engineering structures/materials. Several conclusions can be drawn based on the proposed study.

- It is shown that 10~20 times enhancement for the computational efficiency using the proposed methodology for 2D and 3D structures;

- The increase of signal duration and sensor numbers will improve the imaging quality of the proposed method, but not linearly. The damage detection (location and size) can be achieved with a limited number of sensors and measurement durations;
- The noise level appears to have very little effect on the mean reconstruction of the proposed methodology;
- The proposed methodology can be applied for both homogeneous and heterogeneous materials.

Several future research directions are identified below.

- Experimental validation is required to fully justify the proposed methodology, especially for heterogeneous 3D structures.
- The current approach assumes the damage is related to the shear modulus change. This assumption is appropriate for cracking-induced damage as the stiffness will drop with minimal change of densities. For other type of damages, such as void, swelling, oxidization, and erosion, both density and stiffness may change simultaneously. Extension of the proposed methodology for simultaneous identification of multiple material property changes will be critical and challenging.
- Large uncertainties associated with the damage and measurements has not been systematically addressed. Probabilistic damage imaging will need further investigation for the confidence quantification of the damage detection results.

5.3. Chapter 4

An improved forward and inverse damage imaging is proposed based on CHPATER 3. The improved model includes the interaction between PZT sensor and the host structure. PZT sensor-based methods are widely adopted in damage detection in engineering structures such as aircrafts, pressure vessels, pipeline since the generated wave can travel long distance for large engineering structures with insulation and coating and are sensitive to multiple defects. Also, PZT sensors are lightweight and cost-effectiveness. However, due to the complex wave pattern in engineering structures, it's necessary to include the piezo-electric effect into the numerical model to improve the accuracy of the damage detection model. The key challenge of the coupled model is the computational efficiency especially in large-scale structures. The proposed method focuses on the above difficulty and the high efficiency is achieved by a fast k-space forward model and inverse adjoint model. Experimental validation is performed on various materials. It shows capability of reconstructing multiple damage (crack, void and delamination) simultaneously. The proposed method show potential for real-time damage detection in the engineering structures.

6. REFERENCES

[1] A. Raghavan and C. E. S. Cesnik, “Review of Guided-wave Structural Health Monitoring,” *Shock Vib. Dig.*, vol. 39, no. 2, pp. 91–114, 2007.

[2] J.-B. Ihn and F.-K. Chang, “Pitch-catch Active Sensing Methods in Structural Health Monitoring for Aircraft Structures.”

[3] L. Cheng, S. Member, B. Gao, G. Yun Tian, S. Member, W. Lok Woo, and G. Berthiau, “Impact Damage Detection and Identification Using Eddy Current Pulsed Thermography Through Integration of PCA and ICA,” *IEEE Sens. J.*, vol. 14, no. 5, 2014.

[4] J. Ou and H. Li, “Structural Health Monitoring in mainland China: Review and Future Trends.”

[5] K.-H. Ip and Y.-W. Mai, “Delamination detection in smart composite beams using Lamb waves,” *Smart Mater. Struct.*, vol. 13, no. 3, pp. 544–551, Jun. 2004.

[6] S. S. Kessler, S. M. Spearing, and C. Soutis, “Damage detection in composite materials using Lamb wave methods,” *Smart Mater. Struct.*, vol. 11, no. 2, pp. 269–278, Apr. 2002.

[7] H. Sohn, G. Park, J. R. Wait, N. P. Limback, and C. R. Farrar, “Wavelet-based active sensing for delamination detection in composite structures,” *Smart Mater. Struct.*, vol. 13, no. 1, pp. 153–160, Feb. 2004.

[8] J. He, X. Guan, T. Peng, Y. Liu, A. Saxena, J. Celaya, and K. Goebel, “A multi-feature integration method for fatigue crack detection and crack length estimation in riveted lap joints using Lamb waves,” *Smart Mater. Struct*, vol. 22, pp. 105007–12, 2013.

[9] S. Torkamani, S. Roy, M. E. Barkey, E. Sazonov, S. Burkett, and S. Kotru, “A novel damage index for damage identification using guided waves with application in laminated composites,” *Smart Mater. Struct.*, vol. 23, no. 9, p. 095015, Sep. 2014.

[10] X. Fang, H. Luo, and J. Tang, “Structural damage detection using neural network with learning rate improvement,” 2005.

[11] T. Peng, A. Saxena, K. Goebel, Y. Xiang, S. Sankararaman, and Y. Liu, “A novel Bayesian imaging method for probabilistic delamination detection of composite materials,” *Smart Mater. Struct.*, vol. 22, no. 12, p. 125019, Dec. 2013.

[12] C. Zhou, Z. Su, and L. Cheng, “Probability-based diagnostic imaging using hybrid features extracted from ultrasonic Lamb wave signals,” *Smart Mater. Struct.*, vol. 20, no. 12, p. 125005, Dec. 2011.

[13] J. He, X. Guan, T. Peng, Y. Liu, A. Saxena, J. Celaya, and K. Goebel, “A multi-

feature integration method for fatigue crack detection and crack length estimation in riveted lap joints using Lamb waves," *Smart Mater. Struct.*, vol. 22, no. 10, p. 105007, Oct. 2013.

[14] H. Sohn, C. Farrar, F. Hemez, and D. Shunk, "A review of structural health monitoring literature: 1996–2001," *Los Alamos Natl.*, 2003.

[15] H. Yan, K. Paynabar, and J. Shi, "Anomaly Detection in Images With Smooth Background via Smooth-Sparse Decomposition," *Technometrics*, vol. 59, no. 1, pp. 102–114, Jan. 2017.

[16] F. Mathieu, H. Leclerc, F. Hild, and S. Roux, "Estimation of Elastoplastic Parameters via Weighted FEMU and Integrated-DIC," *Exp. Mech.*, vol. 55, pp. 105–119, 2015.

[17] N. ZABARAS, "An inverse method for determining elastic material properties and a material interface," *Int. J. Numer. Methods Eng.*, 1992.

[18] S.-E. Fang, R. Perera, and G. De Roeck, "Damage identification of a reinforced concrete frame by finite element model updating using damage parameterization," *J. Sound Vib.*, vol. 313, no. 3, pp. 544–559, 2008.

[19] Q. Chang and Y. Liu, "A Novel Computational Method Modeling Wave propagation using K-space method and Damage Detection using Adjoint Method," in *58th AIAA/ASCE/AHS/ASC Structures, Structural Dynamics, and Materials Conference*, 2017.

[20] B. Treeby, B. Cox, and J. Jaros, "k-Wave A MATLAB toolbox for the time domain simulation of acoustic wave fields," vol. 1, p. 75, 2012.

[21] M. Tabei, T. Mast, and R. Waag, "A k-space method for coupled first-order acoustic propagation equations," *J. Acoust. Soc.*, 2002.

[22] D. C. Jiles, "Review of magnetic methods for nondestructive evaluation," *NDT Int.*, vol. 21, no. 5, pp. 311–319, 1988.

[23] S. S. Kessler, S. M. Spearing, and C. Soutis, "Damage detection in composite materials using Lamb wave methods," *Smart Mater. Struct.*, vol. 11, no. 2, pp. 269–278, Apr. 2002.

[24] W. J. Staszewski, B. C. Lee, L. Mallet, and F. Scarpa, "Structural health monitoring using scanning laser vibrometry: I. Lamb wave sensing," *Smart Mater. Struct.*, vol. 13, no. 2, pp. 251–260, Apr. 2004.

[25] L. V. Wang, *Photoacoustic imaging and spectroscopy*. CRC Press, 2009.

[26] Q. Zhan, Q. Ren, Q. Sun, H. Chen, and Q. H. Liu, "Isotropic Riemann Solver for a Nonconformal Discontinuous Galerkin Pseudospectral Time-Domain Algorithm," *IEEE Trans. Geosci. Remote Sens.*, vol. 55, no. 3, pp. 1254–1261, Mar. 2017.

[27] J. Virieux, "*P-SV* wave propagation in heterogeneous media: Velocity-stress finite-difference method," *GEOPHYSICS*, vol. 51, no. 4, pp. 889–901, Apr. 1986.

[28] Y. Cho and J. L. Rose, "An elastodynami`c hybrid boundary element study for elastic guided wave interactions with a surface breaking defect," *Int. J. Solids Struct.*, vol. 37, no. 30, pp. 4103–4124, 2000.

[29] W. M. Ostachowicz, "Damage detection of structures using spectral finite element method," *Comput. Struct.*, vol. 86, no. 3, pp. 454–462, 2008.

[30] T. Peng, a. Saxena, K. Goebel, Y. Xiang, and Y. Liu, "Integrated experimental and numerical investigation for fatigue damage diagnosis in composite plates," *Struct. Heal. Monit.*, vol. 13, no. 5, pp. 537–547, 2014.

[31] Q. Zhan, Q. Sun, Q. Ren, Y. Fang, H. Wang, and Q. H. Liu, "A discontinuous Galerkin method for simulating the effects of arbitrary discrete fractures on elastic wave propagation," *Geophys. J. Int. Geophys. J. Int*, vol. 210, pp. 1219–1230, 2017.

[32] K. Firouzi, A. Nikoozadeh, and B. T. Khuri-Yakub, "Modeling elastic waves in heterogeneous anisotropic media using a k-space method," in *2014 IEEE International Ultrasonics Symposium*, 2014, pp. 1356–1359.

[33] T. D. Mast, L. P. Souriau, D. L. Donald Liu, M. Tabei, A. I. Nachman, and R. C. Waag, "A k-space method for large-scale models of wave propagation in tissue," *IEEE Trans. Ultrason. Ferroelectr. Freq. Control*, vol. 48, no. 2, pp. 341–354, Mar. 2001.

[34] B. T. Cox, S. Kara, S. R. Arridge, and P. C. Beard, "k-space propagation models for acoustically heterogeneous media: Application to biomedical photoacoustics," *J. Acoust. Soc. Am.*, vol. 121, no. 6, p. 3453, 2007.

[35] F. Moser, L. J. Jacobs, and J. Qu, "Modeling elastic wave propagation in waveguides with the finite element method," *NDT E Int.*, vol. 32, no. 4, pp. 225–234, 1999.

[36] N. N. Bojarski, "The k-space formulation of the scattering problem in the time domain," *J. Acoust. Soc. Am.*, vol. 72, no. 2, pp. 570–584, 1982.

[37] Q.-H. Liu, "Generalization of the k-space formulation to elastodynamic scattering problems," *J. Acoust. Soc. Am.*, vol. 97, no. 3, p. 1373, 1995.

[38] M. Tabei, T. D. Mast, and R. C. Waag, "A k-space method for coupled first-order acoustic propagation equations," *J. Acoust. Soc. Am.*, vol. 111, no. 1, pp. 53–63, 2002.

[39] J. Cheng, T. Alkhalifah, Z. Wu, P. Zou, and C. Wang, "Simulating propagation of decoupled elastic waves using low-rank approximate mixed-domain integral operators for anisotropic media," *GEOPHYSICS*, vol. 81, no. 2, pp. T63–T77, Mar. 2016.

[40] K. Firouzi, A. Nikoozadeh, and B. T. Khuri-Yakub, “Modeling elastic waves in heterogeneous anisotropic media using a k-space method,” in *2014 IEEE International Ultrasonics Symposium*, 2014, pp. 1356–1359.

[41] M. Tabei, T. D. Mast, and R. R. C. Waag, “A k-space method for coupled first-order acoustic propagation equations,” *J. Acoust. Soc. Am.*, vol. 111, no. 1, pp. 53–63, Jan. 2002.

[42] P. Zou and J. Cheng, “Pseudo-spectral method using rotated staggered grid for elastic wave propagation in 3D arbitrary anisotropic media,” *Geophys. Prospect.*, Jun. 2017.

[43] B. E. Treeby and B. T. Cox, “k-Wave: MATLAB toolbox for the simulation and reconstruction of photoacoustic wave fields.,” *J. Biomed. Opt.*, vol. 15, no. 2, p. 021314, 2010.

[44] J. P. Berenger, “A perfectly matched layer for the absorption of electromagnetic waves,” *J. Comput. Phys.*, vol. 114, no. 2, pp. 185–200, 1994.

[45] W. C. Chew and Q. H. Liu, “Perfectly matched layers for elastodynamics: a new absorbing boundary condition,” *J. Comput. Acoust.*, vol. 04, no. 04, pp. 341–359, Dec. 1996.

[46] F. Collino and C. Tsogka, “Application of the PML absorbing layer model to the linear elastodynamic problem in anisotropic heteregeneous media,” *RR Inria*, vol. 66, no. 1, pp. 1–31, 1998.

[47] J. Dellinger and J. Etgen, “Wave-field separation in two-dimensional anisotropic media,” *GEOPHYSICS*, vol. 55, no. 7, pp. 914–919, Jul. 1990.

[48] J. L. Rose, *Ultrasonic waves in solid media*. Cambridge university press, 2004.

[49] A. H. Nayfeh, *Wave Propagation in Layered Anisotropic Media - with Applications to Composites*, vol. 39, no. 9. 1995.

[50] R. A. Bale, “Modelling 3D anisotropic elastic data using the pseudospectral approach,” *CREWES Res. Rep. Calgary*, vol. 14, no. June, pp. 2–5, 2002.

[51] R. E. Mickens, “Nonstandard Finite-Difference Schemes,” in *Nonstandard Finite Difference Models of Differential Equations*, WORLD SCIENTIFIC, 1993, pp. 68–92.

[52] Q. Zhang and G. a. McMechan, “2D and 3D elastic wavefield vector decomposition in the wavenumber domain for VTI media,” *Geophysics*, vol. 75, no. 3, pp. D13–D26, 2010.

[53] J. Dellinger, “Wavefield Separation in Anisotropic Media,” in *SEP-Report*, vol. 55, no. 7, 1988, pp. 55–72.

[54] E. Faccioli, F. Maggio, R. Paolucci, and A. Quarteroni, “2d and 3D elastic wave

propagation by a pseudo-spectral domain decomposition method," *J. Seismol.*, vol. 1, no. 3, pp. 237–251, 1997.

[55] L. N. Trefethen, *Finite Difference and Spectral Methods for Ordinary and Partial Differential Equations*. 1996.

[56] J. M. Carcione, "Chapter 1 - Anisotropic Elastic Media," in *Wave Fields in Real Media*, Oxford: Elsevier, 2015, pp. 1–62.

[57] R. C. Payton, *Elastic wave propagation in transversely isotropic media*, vol. 4. Springer Science & Business Media, 2012.

[58] D. Komatitsch, C. Barnes, and J. Tromp, "Simulation of anisotropic wave propagation based upon a spectral element method," *GEOPHYSICS*, vol. 65, no. 4, pp. 1251–1260, Jul. 2000.

[59] C. Tsingas, A. Vafidis, and E. R. Kanasewich, "Elastic wave propagation in transversely isotropic media using finite differences," *Geophys. Prosp.*, vol. 38, no. 08, pp. 933–950, 1990.

[60] J. M. Carcione, D. Kosloff, A. Behle, and G. Seriani, "A spectral scheme for wave propagation simulation in 3-D elastic-anisotropic media," *Geophysics*, vol. 57, no. 12, pp. 1593–1607, 1992.

[61] S. Courtin, C. Gardin, G. Bézine, and H. B. H. Hamouda, "Advantages of the J-integral approach for calculating stress intensity factors when using the commercial finite element software ABAQUS," *Eng. Fract. Mech.*, vol. 72, no. 14, pp. 2174–2185, 2005.

[62] M. Jolly, A. Prabhakar, B. Sturzu, K. Hollstein, R. Singh, S. Thomas, P. Foote, and A. Shaw, "Review of Non-destructive Testing (NDT) Techniques and their Applicability to Thick Walled Composites," in *Procedia CIRP*, 2015, vol. 38, pp. 129–136.

[63] S. Gholizadeh, "A review of non-destructive testing methods of composite materials," *Procedia Struct. Integr.*, vol. 1, pp. 50–57, 2016.

[64] K. Worden and G. Manson, "The application of machine learning to structural health monitoring," *Philos. Trans. R. Soc. A Math. Phys. Eng. Sci.*, vol. 365, no. 1851, pp. 515–537, Feb. 2007.

[65] D. A. Clayton and C. M. Smith, "Comparative testing of nondestructive examination techniques for concrete structures," in *Proc. SPIE*, 2014, vol. 9063, p. 90631G.

[66] L. E. Mujica, J. Vehí, M. Ruiz, M. Verleysen, W. Staszewski, and K. Worden, "Multivariate statistics process control for dimensionality reduction in structural assessment," *Mech. Syst. Signal Process.*, vol. 22, no. 1, pp. 155–171, Jan. 2008.

[67] T. Peng, J. He, Y. Xiang, Y. Liu, A. Saxena, J. Celaya, and K. Goebel,

"Probabilistic fatigue damage prognosis of lap joint using Bayesian updating," *J. Intell. Mater. Syst. Struct.*, vol. 26, no. 8, pp. 965–979, Jun. 2014.

[68] S. Avril, M. Bonnet, A. S. Bretelle, M. Grédiac, F. Hild, P. Ienny, F. Latourte, D. Lemosse, S. Pagano, E. Pagnacco, and F. Pierron, "Overview of identification methods of mechanical parameters based on full-field measurements," *Experimental Mechanics*, vol. 48, no. 4. Springer US, pp. 381–402, 25-Aug-2008.

[69] B. E. Treeby, E. Z. Zhang, and B. T. Cox, "Photoacoustic tomography in absorbing acoustic media using time reversal," *Inverse Probl.*, vol. 26, 2010.

[70] T. Peng and Y. Liu, "3D crack-like damage imaging using a novel inverse heat conduction framework," *Int. J. Heat Mass Transf.*, vol. 102, pp. 426–434, 2016.

[71] M. Doyley, "Model-based elastography: a survey of approaches to the inverse elasticity problem," *Phys. Med. Biol.*, 2012.

[72] M. Ozisik, "Inverse heat transfer: fundamentals and applications," 2000.

[73] F. Moser, L. J. Jacobs, and J. Qu, "Modeling elastic wave propagation in waveguides with the finite element method," *NDT E Int.*, vol. 32, no. 4, pp. 225–234, 1999.

[74] A. A. Oberai, N. H. Gokhale, and G. R. Feijóo, "Solution of inverse problems in elasticity imaging using the adjoint method," *Inverse Probl.*, vol. 19, no. 03, pp. 297–313, 2003.

[75] Y. Jarny, M. N. Ozisikt, and J. P. Bardon, "A general optimization method using adjoint equation for solving multidimensional inverse heat conduction," *ht. J. Heat Mass Transf.*, vol. 34, pp. 2911–2919, 1991.

[76] G. T. Mase, R. M. Smelser, and G. E. Mase, *Continuum mechanics for engineers*. CRC Press, 2010.

[77] J. R. Shewchuk, "An Introduction to the Conjugate Gradient Method Without the Agonizing Pain," 1994.

[78] Y. H. Dai and Y. Yuan, "A Nonlinear Conjugate Gradient Method with a Strong Global Convergence Property," *SIAM J. Optim.*, vol. 10, no. 1, pp. 177–182, Jan. 1999.

[79] J. C. Gilbert and J. Nocedal, "Global Convergence Properties of Conjugate Gradient Methods for Optimization," *SIAM J. Optim.*, vol. 2, no. 1, pp. 21–42, Feb. 1992.

[80] R. Fletcher, *Practical methods of optimization*. Wiley, 2013.

[81] L. Zhang, W. Zhou, and D.-H. Li, "A descent modified Polak – Ribì ere–Polyak conjugate gradient method and its global convergence," *IMA J. Numer. Anal.*, vol. 26, pp. 629–640, 2006.

[82] D. A. Clayton, “Improving synthetic aperture focusing technique for thick concrete specimens via frequency banding,” 2016, p. 98041D.

[83] A. McAndrew, *An Introduction to Digital Image Processing With Matlab*. Boston, MA, United States: Course Technology Press, 2004.

[84] Z. Su, L. Ye, and Y. Lu, “Guided Lamb waves for identification of damage in composite structures: A review,” *J. Sound Vib.*, vol. 295, no. 3–5, pp. 753–780, Aug. 2006.

[85] R. Zhu, G. L. Huang, and F. G. Yuan, “Fast damage imaging using the time-reversal technique in the frequency-wavenumber domain,” *Smart Mater. Struct.*, vol. 22, no. 7, 2013.

[86] L. Yu and V. Giurgiutiu, “In situ 2-D piezoelectric wafer active sensors arrays for guided wave damage detection,” *Ultrasonics*, vol. 48, no. 2, pp. 117–134, Apr. 2008.

[87] C. Maierhofer, M. Röllig, and J. Schlichting, “Active thermography for evaluation of reinforced concrete structures,” in *Non-Destructive Evaluation of Reinforced Concrete Structures: Non-Destructive Testing Methods*, Woodhead Publishing, 2010, pp. 370–402.

[88] A. Mohan and S. Poobal, “Crack detection using image processing: A critical review and analysis,” *Alexandria Eng. J.*, vol. 57, no. 2, pp. 787–798, Jun. 2018.

[89] X. Lin and F. G. Yuan, “Diagnostic Lamb waves in an integrated piezoelectric sensor/actuator plate: analytical and experimental studies,” *Smart Mater. Struct.*, vol. 10, no. 5, pp. 907–913, Oct. 2001.

[90] B. C. Lee and W. J. Staszewski, “Modelling of Lamb waves for damage detection in metallic structures: Part I. Wave propagation,” *Smart Mater. Struct.*, vol. 12, no. 5, pp. 804–814, 2003.

[91] Z. Liu, K. Sun, G. Song, C. He, and B. Wu, “Damage localization in aluminum plate with compact rectangular phased piezoelectric transducer array,” 2015.

[92] V. Giurgiutiu, “Tuned Lamb Wave Excitation and Detection with Piezoelectric Wafer Active Sensors for Structural Health Monitoring.”

[93] Z. Su, L. Ye, and Y. Lu, “Guided Lamb waves for identification of damage in composite structures: A review,” *J. Sound Vib.*, vol. 295, pp. 753–780, 2006.

[94] B. C. Lee and W. J. Staszewski, “Modelling of Lamb waves for damage detection in metallic structures: Part II. Wave interactions with damage,” *Smart Mater. Struct.*, vol. 12, no. 5, pp. 815–824, 2003.

[95] W. J. Staszewski, B. C. Lee, and W. J. Staszewski, “Modelling of Lamb waves for damage detection in metallic structures: Part I. Wave propagation Modelling of Lamb waves for damage detection in metallic structures: Part I. Wave propagation

Modelling of Lamb waves for damage detection in metallic structures: Part I. Wave propagation," 2003.

[96] Z. Su and L. Ye, "Lamb Wave Propagation-based Damage Identification for Quasi-isotropic CF/EP Composite Laminates Using Artificial Neural Algorithm: Part I-Methodology and Database Development."

[97] Y. Kim, S. Ha, and F.-K. Chang, "Time-Domain Spectral Element Method for Built-In Piezoelectric-Actuator-Induced Lamb Wave Propagation Analysis," 2007.

[98] Y. Shen and V. Giurgiutiu, "WaveFormRevealer: An analytical framework and predictive tool for the simulation of multi-modal guided wave propagation and interaction with damage," *Struct. Heal. Monit.*, vol. 13, no. 5, pp. 491–511, 2014.

[99] B. Poddar and V. Giurgiutiu, "Scattering of Lamb waves from a discontinuity: An improved analytical approach," *Wave Motion*, vol. 65, pp. 79–91, 2016.

[100] Y. Zheng, K. Liu, Z. Wu, D. Gao, R. Gorgin, S. Ma, and Z. Lei, "Lamb waves and electro-mechanical impedance based damage detection using a mobile PZT transducer set," *Ultrasonics*, vol. 92, pp. 13–20, Feb. 2019.

[101] M. Gresil, V. Giurgiutiu, Y. Shen, and B. Poddar, "Guidelines for Using the Finite Element Method for Modeling Guided Lamb Wave Propagation in SHM Processes," in *Proceedings of the 6th European Workshop on Structural Health Monitoring*, 2012, pp. 1–8.

[102] Y. Shen and V. Giurgiutiu, "Combined analytical FEM approach for efficient simulation of Lamb wave damage detection," 2016.

[103] V. Giurgiutiu and A. N. Zagrai, "Characterization of Piezoelectric Wafer Active Sensors," *J. Intell. Mater. Syst. Struct.*, vol. 11, no. 12, pp. 959–976, 2000.

[104] T. Wang, "Finite element modelling and simulation of guided wave propagation in steel structural members," 2014.

[105] Z. Su and L. Ye, *Identification of Damage Using Lamb Waves*, vol. 48. 2009.

[106] X. Lin and F. Yuan, "Diagnostic Lamb waves in an integrated piezoelectric sensor/actuator plate: analytical and experimental studies," *Smart Mater. Struct.*, 2001.

[107] Y. Zhao, F. Li, P. Cao, Y. Liu, J. Zhang, S. Fu, J. Zhang, and N. Hu, "Generation mechanism of nonlinear ultrasonic Lamb waves in thin plates with randomly distributed micro-cracks," *Ultrasonics*, vol. 79, pp. 60–67, Aug. 2017.

[108] TORAYCA, "T700G Preliminary Data Sheet Carbon."

[109] K. Firouzi, B. T. Cox, B. E. Treeby, and N. Saffari, "A first-order k-space model for elastic wave propagation in heterogeneous media," *J. Acoust. Soc. Am.*, vol. 132, no. 3, pp. 1271–1283, 2012.

[110] E. H. Saenger and S. A. Shapiro, “Effective velocities in fractured media: a numerical study using the rotated staggered finite-difference grid,” *Geophys. Prospect.*, vol. 50, no. 2, pp. 183–194, Mar. 2002.

[111] H. Igel, P. Mora, and B. Riollet, “Anisotropic wave propagation through finite-difference grids,” *Geophysics*, vol. 60, no. 4, pp. 1203–1216, 1995.